Aus dem Lehrstuhl für Experimentelle Ultrahochfeld Magnet Resonanz der
Medizinischen Fakultät Charité – Universitätsmedizin Berlin

DISSERTATION

Parametrische suszeptibilitätsgewichtete Bildgebung des Myokards mittels Magnetresonanzbildgebung bei hohen Magnetfeldern: Methodenentwicklung und Anwendung

zur Erlangung des akademischen Grades

Doctor rerum medicinalium (Dr. rer. medic.)

vorgelegt der Medizinischen Fakultät

Charité – Universitätsmedizin Berlin

von

Fabian Hezel

aus Essen

Datum der Promotion: 22.06.2014

Inhaltsverzeichnis

Zusammenfassung

Kurzfassung

Die Gewebedifferenzierung des Myokards mittels suszeptibilitäts- (T_2^*) gewichteter Kartierungstechniken findet in der (prä)-klinischen kardiovaskulären Magnetresonanzbildgebung steigenden Einsatz. Der Anstieg der Suszeptibilitätsempfindlichkeit bei steigenden Magnetfeldstärken macht die myokardiale T_2^* Kartierung bei hohen Magnetfeldstärken konzeptionell besonders attraktiv. Die Anwendungsmöglichkeiten der T_2^* gewichteten Herz MRT sind unter anderem die Erkennung myokardialer Ischämien, die Charakterisierung der Sauerstoffversorgung und die Darstellung der Mikrostruktur des Herzmuskels.

In dieser Arbeit werden geeignete Methoden entwickelt um die myokardialen T_2^* gewichtete Bildgebung bei hohen (3 T) und ultrahohen (7 T) Magnetfeldstärken durchzuführen. Zu diesem Zweck werden T_2^* gewichtete Pulssequenzen an die Anforderungen der Hochfeld MRT angepasst und Hochfrequenzspulen mit 4, 8, 16 und 32 Sende- und Empfangskanälen für die Herzbildgebung bei 7 T entwickelt und evaluiert. In Phantomexperimenten werden diese Pulssequenzen, welche eine dynamische, zeitlich aufgelöste (CINE) Kartierung erlauben mit etablierten Techniken validiert. In einer Studie mit gesunden Probanden werden zudem B_0 Shimming Techniken angewendet um makroskopische Feldinhomogenitäten zu reduzieren und dadurch die Suszeptibiltätsempfindlichkeit gegenüber mikroskopischen Effekten zu verstärken.

Diese Arbeit liefert erste in-vivo Normwerte für T_2^* Zeiten im gesunden humanen Herzmuskel bei 7 T und vergleicht diese Ergebnisse mit Daten welche bei 1.5 T und 3 T erhoben wurden. Die maximale B_0 Differenz konnte durch einen volumenselektiven Shim von etwa 400 Hz auf etwa 80 Hz für den Vierkammerblick und auf etwa 65 Hz für einen mitventrikulären Kurzachsenblick des Herzens reduziert werden. Die längsten T_2^* -Werte wurden für anteriore (T_2^* = 14,0 ms), anteroseptale (T_2^* = 17,2 ms) und inferoseptale (T_2^* = 16,5 ms) Myokardsegmenten gefunden. Die kürzesten T_2^* -Werte hingegen wurden für beobachtet inferiore (T_2^* = 10,6 ms) und inferolaterale (T_2^* = 11,4 ms) Segmente. Zwischen der end-diastolischen und end-systolischen Herzphase wurden signifikante Unterschiede ($p = 0,002$) in den T_2^*-Werten beobachtet mit Änderungen von T_2^* -Werten von bis zu ca. 27% über den Herzzyklus, welche besonders in der Herzscheidewand ausgeprägt waren.

Die T_2^* gewichtete Bildgebung bei 7 T bietet die Möglichkeit Änderungen der Sauerstoffsättigung im Herzmuskel zu visualisieren und zu quantifizieren. Bestehende Limitationen bezüglich räumlicher und zeitlicher Auflösung der konventionell eingesetzten Perfusions-Bolusmessungen mit Kontrastmittel könnten dadurch umgangen werden. Der endogene Kontrast des BOLD Effekts ermöglicht es, Änderungen im Gleichgewicht zwischen Sauerstoffversorgung und Sauerstoffnachfrage früh zu erkennen und zu visualisieren. Zusammenfassend unterstreichen diese Ergebnisse die Herausforderungen des myokardialen T_2^* Kartierung bei 7 T, zeigen jedoch, dass diese Probleme durch maßgeschneiderte B_0-Shimming Techniken und angepasste Akquisitionstechniken kompensiert werden können.

Abstract

Myocardial tissue characterization using T_2^* relaxation mapping techniques is an emerging application of (pre)clinical cardiovascular magnetic resonance imaging. The increase in microscopic susceptibility at higher magnetic field strengths renders myocardial T_2^* mapping at ultrahigh magnetic fields conceptually appealing. Applications of T_2^* weighted cardiac MR include the detection of myocardial ischemia, the characterization of oxygen supply and the microstructure of the cardiac muscle.

This work develops methods for myocardial T_2^* mapping at high (3 T) and ultrahigh (7 T) magnetic field strengths. For this reason T_2^* weighted pulse sequences are adapted to the requirements of highfield MRI and dedicated RF coils with 4, 8, 16 and 32 transmit and receive channels are developed for cardiac imaging at ultrahigh field strengths. In phantom experiments the pulse sequences, which provide dynamic, time resolved maps are benchmarked against conventional techniques. In a volunteer study B0 shimming techniques are applied to reduce macroscopic field inhomogeneities and therefore increase the susceptibility sensitivity for microscopic effects.

This work presents the first in-vivo norm values T_2^* values in the healthy human cardiac muscle at 7 T and compares it to results which were collected at 1.5 T and 3 T. for . The peak-to-peak B_0 difference following volume selective shimming was reduced from approximately 400 Hz to approximately 80 Hz for the four chamber view and mid-ventricular short axis view of the heart and to 65 Hz for the left ventricle. The longest T_2^* values were found for anterior (T_2^* = 14.0 ms), anteroseptal (T_2^* = 17.2 ms) and inferoseptal (T_2^* = 16.5 ms) myocardial segments. Shorter T_2^* values were observed for inferior (T_2^* = 10.6 ms) and inferolateral (T_2^* = 11.4 ms) segments. A significant difference ($p = 0.002$) in T_2^* values was observed between end-diastole and end-systole with T_2^* changes of up to approximately 27% over the cardiac cycle which were pronounced in the septum.

T_2^* weighted imaging at 7 T offers the potential to visualize and quantify changes in oxygen supply in the cardiac muscle. Existing limitations regarding spatial and temporal resolution of conventional first-pass perfusion imaging with contrast agents can avoided. The endogenous contrast provided by the BOLD effect allows the early detection of imbalances in oxygen supply and demand. To conclude, these results underscore the challenges of myocardial T_2^* mapping at 7.0 T but demonstrate that these issues can be offset by using tailored shimming techniques and dedicated acquisition schemes

Einleitung

Die kardiovaskuläre Magnetresonanztomographie (CMR) bietet eine Vielzahl von Möglichkeiten zur nicht-invasiven Diagnostik von Herzerkrankungen. Suszeptibilitätsgewichtete Bildgebungstechniken, auch als T_2^* gewichtete Techniken bezeichnet, sind sensitiv gegenüber mikroskopischen Feldinhomogenitäten und können diese sowohl qualitativ als auch quantitativ erfassen. Anwendungsmöglichkeiten der T_2^* gewichteten CMR sind unter anderem die Erkennung myokardialer Ischämien oder die Charakterisierung der Durchblutung des Herzmuskels. T_2^* sensitive Techniken stellen somit eine Alternative zu klinisch etablierten First-Pass Perfusionstechniken dar, welche auf exogener Kontrastmittelgabe beruhen. Im Gegensatz dazu nutzen die T_2^* gewichteten Techniken den endogenen Kontrastmechanismus des Blood Oxygen Level Dependent (BOLD) Effekts aus. Der BOLD Effekt beruht auf den unterschiedlichen magnetischen Eigenschaften von oxygeniertem (diamagnetisch) und desoxygeniertem (paramagnetisch) Hämoglobin. Das paramagnetische desoxygenierte Hämoglobin führt zu lokalen mikroskopischen Inhomogenitäten des Magnetfeldes, wodurch die effektive transversale Relaxationszeit T_2^* verkürzt wird. Die Messung von T_2^* ermöglicht somit den Nachweis einer veränderter Konzentration des desoxygenierten Hämoglobins aufgrund von Blutfluss oder Sauerstoffverbrauch. Die Anwendung dieser Technik am Herzen wurde in einer Vielzahl von Publikationen untersucht und gegenüber anderen Modalitäten wie quantitativer Koronarangiographie oder SPECT verglichen [1,2]. Es konnte gezeigt werden, dass es während pharmakologischen Stress (Adenosin- oder Dipyridamolgabe) zu signifikanten Unterschieden in der BOLD Signalintensität zwischen gesunden und ischämischen Regionen des Myokards kommt [3]. Somit kann eine myokardiale Ischämie aufgrund von Koronarstenosen mittels des BOLD Effekts nachgewiesen werden. Da diese Methode direkt die Sauerstoffsättigung im Herzmuskel misst, bietet sie Vorteile gegenüber der Koronarangiographie, welche anhand des Zustands der Koronargefäße indirekt auf die Durchblutung des Herzmuskels schließt.

BOLD CMR Daten bei 1.5 Tesla (T) sind jedoch bisher beschränkt auf kleine Patientenpopulationen oder experimentelle Tierstudien. Die Limitationen der bisherigen Arbeiten sind geringe Signalunterschiede zwischen gesunden und pathologischen Regionen im Myokard, das niedrige Signal-zu-Rausch Verhältnis (SNR), der auf Grund der Feldstärke von 1.5 T eher schwach ausgeprägte BOLD-Effekt, die niedrige Spezifität

der Methode, Blutfluss, bewegungsbedingte Artefakte und Verzerrungen aufgrund von Magnetfeldinhomogenitäten.

Der Übergang zu Hochfeld MRT Systemen (>3 T) bietet das Potenzial, die genannten Limitationen zu reduzieren. So bietet ein stärkeres statisches Magnetfeld (B_0 Feld) neben einem höheren SNR auch einen Anstieg der BOLD Empfindlichkeit. Durch Simulationen und Experimente konnte gezeigt werden, dass die BOLD Sensitivität durch den Anstieg von 1.5 T zu 3.0 T so erhöht wurde, dass selbst geringe, aber klinisch relevante Blutflussunterschiede im Herzmuskel detektiert werden können [4].

Die Herzbildgebung bei ultrahohen Magnetfeldstärken (≥7 T) wird durch den inhärenten SNR Vorteil motiviert. Dieser kann in eine höhere räumliche oder zeitliche Auflösung, oder aber in eine Verkürzung der Datenaufnahme investiert werden. Das volle Potenzial der Ultrahochfeld MRT ist jedoch bisher nicht ausgeschöpft, da insbesondere bei der Herzbildgebung die Vorteile auf Grund physikalischer Einschränkungen nicht direkt genutzt werden können. Zu diesen Einschränkungen zählen die erhöhte Magnetfeldinhomogenität, sogenannte Offresonanz-Artefakte und dielektrische Effekte. Aufgrund der Wellenlänge des verwendeten elektro-magnetischen Feldes von $\lambda \approx 12$ cm bei einer Feldstärke von 7 T entsteht ein komplexes Anregungsfeld, welches zu Signalauslöschungen und zu lokalen Überschreitungen des maximalen Wertes der spezifische Absorptionsrate (SAR) führen kann. Im Gegensatz zu klinischen Scannern, sind für 7 T Forschungs-MRT Systeme keine Volumenspulen zum Senden der Radiofrequenz vorgesehen, weshalb spezielle Sende- und Empfangsspulen benötigt werden. Für die Herzbildgebung waren zu Beginn dieser Arbeit keine kommerziell oder anderweitig verfügbaren Hochfrequenz (HF)-Spulen vorhanden, weshalb die Entwicklung und Validierung mehrkanaliger HF-Spulen ein Teil dieser Arbeit ist. Des Weiteren ist das Elektrokardiogramm (EKG), welches ein elektrisches Signal ist, innerhalb hoher Magnetfelder stark gestört und vielfach für den Gebrauch ungeeignet. Da das EKG Signal zur Synchronisation der Datenaufnahme mit dem Herzschlag benötigt wird, führen fehlerhafte Triggerpulse aufgrund des gestörten Signals zu Bewegungsartefakten in den Bilddaten.

Das Ziel dieser Arbeit bestand darin, Methoden für suszeptibilitätsgewichtete CMR Bildgebung bei hohen und ultrahohen Magnetfeldstärken zu entwickeln, diese in Phantomstudien zu evaluieren und eine Studie mit gesunden Probanden durchzuführen.

Die Methodenentwicklung umfasst dabei Erweiterungen und Modifikationen von Gradienten-Echo und schnellen Spin-Echo Sequenzen. Des Weiteren wird die Abhängigkeit der Feldstärke auf die BOLD Sensitivität untersucht, und analysiert inwieweit suszeptibilitätsbedingte Bildartefakte feldstärkeabhängig sind. Außerdem liefert diese Arbeit erste in-vivo Normwerte für T_2^* Zeiten im gesunden humanen Herzmuskel bei 7 T und vergleicht diese Ergebnisse mit Daten welche bei 1.5 T und 3 T erhoben wurden. Als notwendige Vorarbeit werden Hochfrequenz Sende- und Empfangsspulen mit 4, 8,16 und 32 Kanälen für die Herzbildgebung bei 7 T entwickelt und evaluiert. Diese Mehrkanal Sende- und Empfangsspulen sind eine Voraussetzung für ein homogenes Anregungsfeld (B_1^+) und für die parallele Bildgebung als Beschleunigungsmethode für die Datenakquise. Zudem wird eine Alternative zur herkömmlichen EKG basierten Synchronisation präsentiert, welche auf der Detektion der Herztöne im akustischen Phonokardiogramm basiert und daher auch bei hohen und ultrahohen Magnetfeldstärken verlässliche Triggersignale liefert.

Methodik

Hochaufgelöste T_2^* Kartierung am menschlichen Herzen bei 7 T

T_2^* Kartierung mit GRE Techniken

Gradienten-Echo (GRE) Sequenzen besitzen einen intrinsischen T_2^* Kontrast welcher durch die Anpassung der Echozeit TE variiert werden kann, wodurch verschiedene T_2^* Wichtungen erzeugt werden können. Auf Grund ihrer hohen Geschwindigkeit sind GRE Sequenzen für die Herzbildgebung gut geeignet. Innerhalb eines Anregungsintervalls wird in klassischen GRE Sequenzen ein einzelnes Echo akquiriert. Diese Abfolge wird für alle Phasenkodierungsschritte und jede einzelne Wichtung wiederholt und somit eine Serie von Bildern mit unterschiedlich starken T_2^* Wichtungen erstellt. Daraus kann mittels einer Ausgleichrechnung für jeden einzelnen Bildpunkt die charakteristische Zerfallszeit T_2^* bestimmt werden.

Die Wahl der optimalen Echozeitpunkte hängt von der Magnetfeldstärke und der Art der Anwendung ab. Da im Herzen sowohl Wasser als auch Fett zum Signal beitragen, ist der T_2^* Zerfall durch eine oszillierende exponentiell fallende Kurve charakterisiert (Abbildung 1). Die Oszillation resultiert aus dem Unterschied in der Resonanzfrequenz von Wasser gegenüber Fett, infolgedessen der vom Fett stammende Teil des Signals oszilliert. Die Amplitude der Signaloszillation ist abhängig von der unbekannten Fettkonzentration des abzubildenden Gewebes. Hohe Amplituden können dazu führen, dass die Berechnung der Zerfallskurve verfälscht wird. Um dies zu vermeiden werden Echozeitpunkte gewählt, zu denen das Fettsignal entweder voll (in-phase) oder nicht (out-phase) zum Wassersignal beiträgt, um so die Oszillation zu unterdrücken.

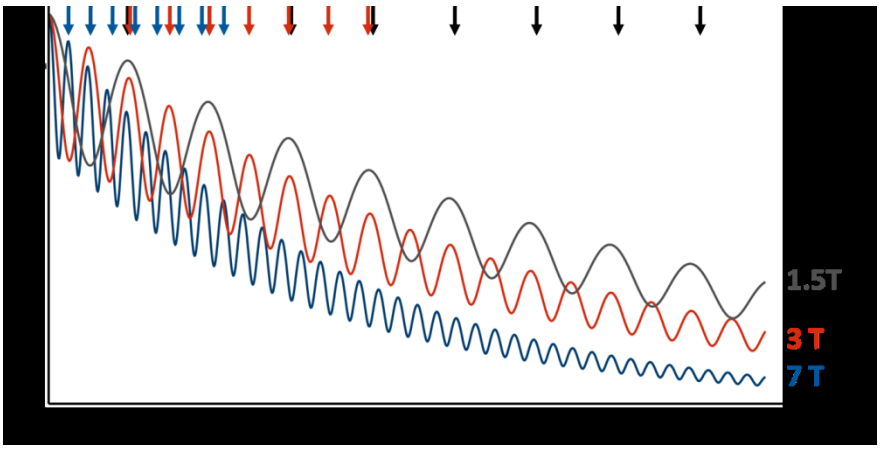

Abbildung 1: T_2^* Zerfallskurven von einem Fett und Wasser Signal bei 1.5 T*, 3T und* 7 T

Die Frequenz der Oszillation und damit auch die optimalen Echozeitpunkte sind von der chemischen Verschiebung zwischen Fett und Wasser von 3.35 ppm abhängig. Dies ergibt Frequenzunterschiede abhängig von der Magnetfeldstärke: 220 Hz bei 1.5 T, 440 Hz bei 3 T und 1027 Hz bei 7 T. Daraus ergeben sich Echozeitintervalle von 4.6 ms für 1.5 T, 2.3 ms für 3 T und 1.02 ms für 7 T.

Multi-Echo GRE (ME-GRE) Sequenzen akquirieren nach jeder Anregung mehrere Echos mit unterschiedlichen Echozeiten und erlauben auf diese Weise die für die T_2^* Kartierung notwendigen Echos innerhalb eines Anregungsintervalls (Repetitionszeit TR) aufzunehmen. Dadurch wird die Datenakquise erheblich beschleunigt. Der ME-GRE Ansatz wird bei 1.5 T standardmäßig eingesetzt. Die kurzen Interechozeiten von 1.02 ms bei 7 T führen jedoch dazu, dass nicht alle notwendigen Echos aufgenommen werden können, da die Vorbereitungs- und Auslesedauer eines einzelnen Echos länger als die optimale Interechozeit ist. ME-GRE Bildgebung ist aus diesem Grund bei 7 T nur mit Einschränkungen in der Wahl der Echozeiten durchführbar. Dennoch bietet die kurze Interechozeit bei 7 T einen Geschwindigkeitsvorteil gegenüber niederen Feldstärken dar, der konzeptionell auch zeitlich aufgelöste T_2^* Kartierungen über den Herzzyklus ermöglichen soll.

Aus diesem Grund wurde ein Hybridansatz aus klassischem GRE und ME-GRE implementiert, welcher einerseits die flexible Wahl der Echozeit der klassichen GRE Sequenz als auch die Effizienz der Echoaufnahme des ME-GRE Ansatzes bietet. Die ME-GRE Sequenz wurde um zusätzliche Anregungspulse zu einer Multi-Shot (MS) GRE erweitert. Dadurch werden nach jeder Anregung mehrere Echos akquiriert, wobei eng beieinanderliegende Echos in unterschiedlichen Intervallen aufgenommen werden. Dieser verschachtelte Ansatz umgeht die Limitationen der ME-GRE Sequenz, bietet aber weiterhin sowohl einen Geschwindigkeitsvorteil gegenüber dem klassischen Ansatz als auch die freie Wahl der Echozeiten.

Ein Vorteil des schnellen T_2^* Zerfalls bei 7 T ist die relativ kurze notwendige Echozeit von 10 ms um einen starken Kontrast für die T_2^* Kartierung zu erzeugen. Im Gegensatz dazu beträgt diese maximale Echozeit etwa 30 ms bei 1.5 T und 20 ms bei 3 T. Aufgrund dessen ist eine T_2^* Kartierung des Herzzyklus mit einer zeitlichen Auflösung von 25 Herzphasen bei 7T möglich. Dazu wurde eine über mehrere Atemanhaltephasen

verschachtelte Multi-Breathhold CINE (MB CINE) Sequenz erstellt. Die verwendeten GRE Sequenzen sind in Abbildung 2 zusammengefasst.

Die Genauigkeit der T_2^* Kartierung mittels der unterschiedlichen Multi-Echo GRE Sequenzen wurde an Phantomen mit kurzen und mittleren T_2^* Zeiten gegenüber der klassischen GRE Technik verglichen. In einer Studie mit acht gesunden Probanden wurden mittels MS-GRE T_2^* Karten des Myokards im Kurzachsenblick und Vierkammerblick sowohl während der Diastole als auch der Systole erstellt und analysiert. Zusätzlich wurde der gesamte Herzzyklus mittels MB CINE Sequenzen T_2^*-kartiert [5].

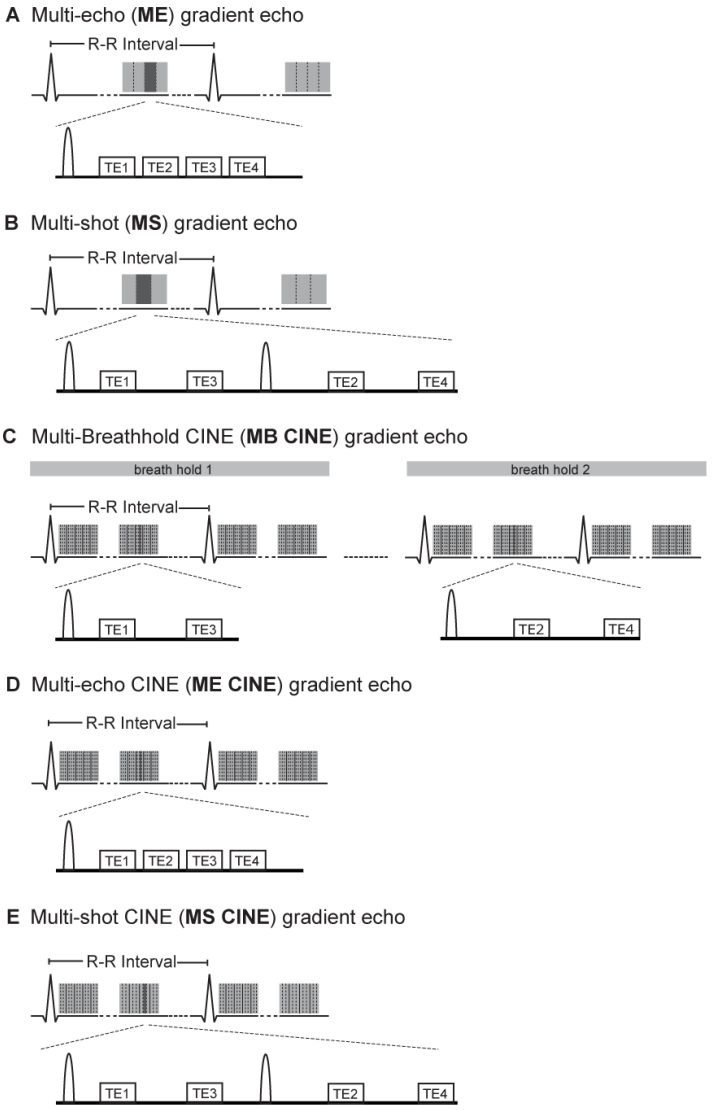

Abbildung 2:Übersicht der verwendeten Multi-Echo Gradienten Echo Techniken zur T_2^* Kartierung

Minimierung der makroskopischen Inhomogenitäten (B_0 Shimming)

Der T_2^* Kontrast von GRE Sequenzen wird durch physiologisch bedingte mikroskopische Inhomogenitäten beeinflusst. Diese basieren unter anderem auf dem BOLD Effekt. Zusätzlich bestimmen aber auch makroskopische Inhomogenitäten des statischen Magnetfeldes den T_2^* Kontrast. Um eine robuste BOLD sensitive Bildgebung zu gewährleisten, ist es deshalb unerlässlich, die makroskopischen Inhomogenitäten zu reduzieren, sodass die durch den BOLD Effekt erzeugten Inhomogenitäten nicht davon überlagert werden. Makroskopische Magnetfeldinhomogenitäten entstehen durch imperfekte statische Magnetfelder und durch den Einfluss der Beladung (Patientenkörper, Phantom) auf das statische Magnetfeld. Insbesondere Regionen mit sehr hohen Suszeptibilitätsübergängen, wie beispielsweise die Grenze zwischen Herz und Lunge, führen zu starken Magnetfeldvariationen. Mittels für 7 T angepasster Sequenzen wurden Karten der Magnetfeldverteilung (B_0 Karten) erstellt. Um eine homogene Verteilung des Feldes im Bereich des Herzens zu erreichen, wurde lediglich dieser Bereich mittels der berechneten B_0 Karten optimiert. Mit diesem Ansatz konnte auch bei 7 T eine Magnetfeldhomogenität erreicht werden, die mit üblichen Werten bei 3 T und 1.5 T vergleichbar ist.

Feldstärkenvergleich

T_2^* Zeiten des Herzmuskels und die myokardiale Verteilung von Artefakten weisen eine Feldstärkenabhänggkeit auf. Diese wurde in einer Studie an gesunden Probanden mittels Untersuchungen bei 1.5 T, 3 T und 7 T untersucht. Dazu wurden lokales R_2^* ($R_2^* = 1000 / T_2^*$) in 16 standardisierten Herzsegmenten, globales R_2^* und R_2^* im Septum bestimmt. Ein wurde ein Artefakt Faktor bestimmt, welcher die Abweichung von lokalem zu globalem R_2^* beschreibt (siehe [6]) und ein Vergleich dieses Faktors zwischen den drei Feldstärken durchgeführt.

Suszeptibilitätsgewichtete Spin-Echo Bildgebung

Eine weitere Möglichkeit T_2^* zu quantifizieren ist die Verwendung von Spin-Echo Techniken. Diese wenden nach dem Anregungspuls einen oder mehrere Refokussierungspulse an. Dadurch sind sie per se immun gegenüber Magnetfeldinhomogenitäten und somit T_2 statt T_2^* sensitiv. Spin Echo Techniken können jedoch durch das Einfügen einer zusätzlichen, frei skalierbaren Suszeptibilitätswichtungzeit (τ) vor dem ersten Refokusierungspuls verändert werden,

wodurch eine T_2^* Sensitivität erzeugt wird. Abbildung 3 zeigt das Sequenzdiagramm einer suszeptibilitätsgewichteten schnellen Spin Echo Sequenz. Um diese an die Anforderungen der Herzbildgebung anzupassen, werden zusätzlich zum modifizierten Bildgebungsmodul (displaced UFLARE) Vorbereitungsexperimente zur Atemkompensation und Blutunterdrückung angewendet.

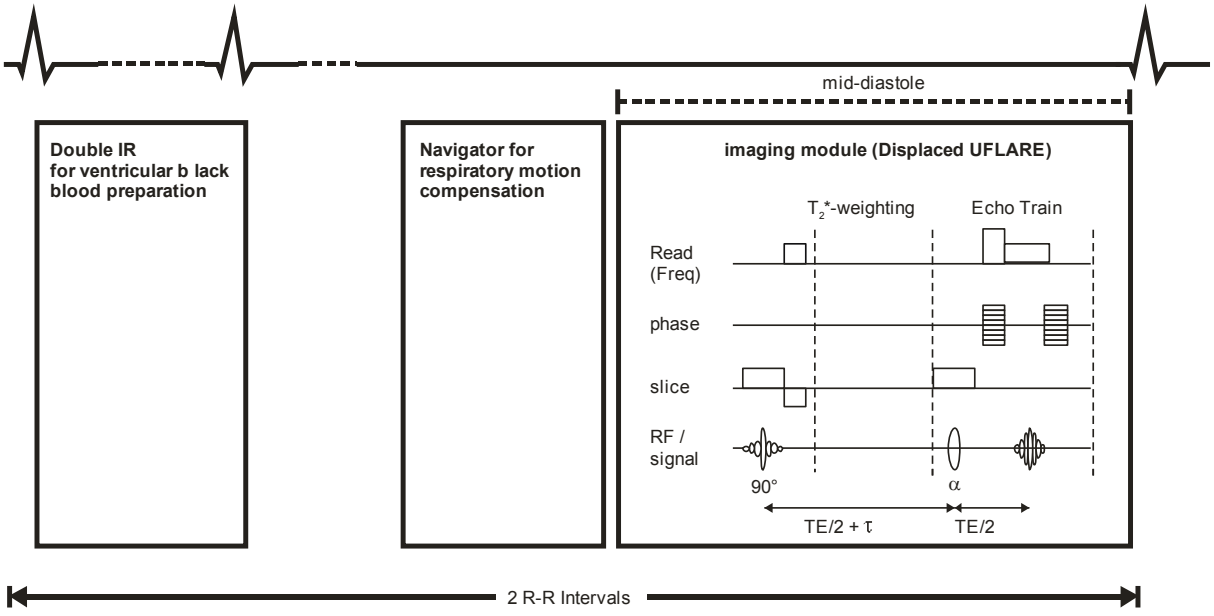

Abbildung 3: Sequenzdiagramm der suszeptibilitätsgewichteten Spin Echo Sequenz

Die Immunität gegenüber statischen Magnetfeldinhomogenitäten bleibt trotz der hinzugefügten T_2^* Wichtung erhalten, wodurch dieser Ansatz den Vorteil hat, lediglich sensitiv gegenüber physiologisch induzierten, also mikroskopischen Feldinhomogenitäten, zu sein.

Da Spin Echo Sequenzen ein homogenes Anregungsfeld benötigen, kann diese Technik zum jetzigen Stand bisher nicht mit der notwendigen diagnostischen Güte bei ultrahohen Feldern angewendet werden. Die beschriebene Sequenz wurde bei 1.5 T und 3 T in Phantomen und gesunden Probanden getestet und mit GRE Ergebnissen verglichen [7].

Vorarbeiten zur Herzbildgebung bei 7 T

Es wurde bereits erwähnt, dass für die Herzbildgebung bei 7 T besondere HF-Spulen zum Senden und Empfangen der Radiofrequenz notwendig sind. Die mit steigender Feldstärke sinkende Wellenlänge der Radiofrequenz verursacht ein inhomogenes Anregungsfeld. Deshalb wurden spezielle Oberflächenspulen zum Senden und Empfangen der Radiofrequenz entwickelt, die es erlauben das Anregungsfeld

anzupassen und zu homogenisieren. Dadurch wird die Energie effizienter verteilt, als es bei Volumenspulen der Fall ist, die bei niedrigen Feldstärken verwendet werden.

16-Kanal Sende- und Empfangsspule für die Herzbildgebung

Eine 16 Kanal Sende- und Empfangsspule wurde speziell für die Herzbildgebung entwickelt [8]. Sie besteht aus zwei Bauteilen. Das flache untere Bauteil lässt sich in den Tisch des MR Scanners integrieren und das leicht gebogene obere Bauteil ist einem durchschnittlichen Torso angepasst. Beide Bauteile bestehen jeweils aus 8 Loop-Elementen, welche es erlauben zwischen Signalpenetration (B_1^+) in den Körper und der Belastung durch das Anregungssignal (SAR) abzuwägen. Aus diesem Grund wurden B_1^+ Simulationen durchgeführt und mit Phantommessungen vergleichen. Anhand eines Voxelmodels für einen menschlichen Körper wurde die maximale Sendeleistung gemäß der IEC Vorgaben bestimmt. Die B_1^+ Verteilung wurde bei Probandenmessungen mittels Phasenmodulationen weiter angepasst, um ein möglichst homogenes Anregungsfeld über das gesamte Herz zu erzielen.

Diese 16-Kanal Spule wurde in einer Studie (N=10) mit zuvor entwickelten Oberflächenspulen mit 4 beziehungsweise 8 Sende- und Empfangskanälen verglichen. Dabei wurden Herzfunktionsbestimmung und SNR im Zusammenhang mit paralleler Bildgebung untersucht [9].

Akustische Triggerung

Für die Herzbildgebung ist eine Synchronisation der Datenaufnahme mit dem Herzschlag unerlässlich, da nicht der komplette Datensatz innerhalb eines Herzschlages aufgenommen wird und so eine Information über die aktuelle Position im Herzzyklus benötigt wird. Das in der klinischen Routine verwendete EKG ist jedoch bei 7 T aufgrund von Wechselwirkungen des elektrischen Signals mit dem Magnetfeld stark gestört. Aus diesem Grund wurde eine Alternative entwickelt, welche unabhängig von der Magnetfeldstärke eine robuste Synchronisation erlaubt. Diese Methode basiert auf der Detektion des ersten Herztones im akustischen Phonokardiogramm. Dieser wird mittels eines MR-kompatiblen Stethoskops registriert, mit Filtertechniken von Störgeräuschen des MR befreit [10] und erlaubt auf diese Weise eine akustische Triggerung (ACT) der Bildgebung.

Die Funktion und die Robustheit der akustischen Synchronisation wurde anhand von Studien an gesunden Probanden (N=14) bei 1.5 T und 3 T evaluiert. Zu diesem Zweck

wurde die Herzfunktion mittels EKG und ACT im MRT ermittelt und miteinander verglichen [11]. Bei 7 T wurde zusätzlich die Pulsoxymetrie zum Vergleich hinzugezogen [12].

Ergebnisse

Hochaufgelöste T_2^* Kartierung am menschlichen Herzen bei 7 T

Der Vergleich von MS-GRE gegenüber konventionell genutzten ME-GRE Techniken zeigte bei Phantommessungen keine signifikanten Unterschiede hinsichtlich der berechneten T_2^* Zerfallszeiten. Für alle Techniken konnte durch eine Verringerung der Schichtdicke und der damit verbundenen Verringerung der Dephasierungseffekte innerhalb der Voxel eine homogenere T_2^* Karte für beide Phantome erzielt werden.

Basierend auf den Phantomergebnissen wurde für die in-vivo Studie eine Schichtdicke von 4 mm und damit ein Kompromiss zwischen Rauschverstärkung und makroskopischen Magnetfeldveränderungen gewählt. Mittels des volumenselektiven Shims, wodurch das B_0 Feld lediglich im Bereich des Herzens homogenisiert wurde, konnte die maximale Feldverteilung über das gesamte Herz von etwa 400 Hz auf 80 Hz reduziert werden. Dies ist ausführlich in [5] beschrieben. Es wurde ein maximaler Feldgradient von etwa 20 Hz/mm beobachtet. Dieser trat im Bereich des Übergangs von Herz zu Lunge, sowie im inferioren und inferolateralen Segment des Kurzachsenblicks auf (Abbildung 4). Auf Grund dieses B_0 Gradienten war das Signal in den genannten Bereichen durch Phasenverluste um etwa 80% reduziert. Für die verbleibenden Herzsegmente betrug der durchschnittliche B_0 Gradient entlang der Schichtrichtung nur etwa 3 Hz/mm, wodurch Signalverminderungen auf Grund von Phasenverlusten minimal waren und der T_2^* Kontrast durch mikroskopische Feldinhomogenitäten dominiert wurde.

Die homogenisierte B_0 Verteilung ermöglichte die Aufnahme von T_2^* gewichteten MS-GRE und MB CINE Daten bei 7 T. Selbst für hohe Echozeiten von 10 ms traten keine deutlichen Suszeptibiltätsartefakte oder Signalauslöschungen im Septum und in den lateralen Herzsegmenten auf. Somit konnten sowohl mit MS als auch mit MB CINE Sequenzen T_2^* Karten des Herzens erzeugt werden. Die Differenz zwischen den von MS-GRE und MB CINE Techniken ermittelten T_2^* Werten im midventrikulären Myokardium betrug $T_{2\,diff}^* = (0.2 \pm 3.7)$ ms. Es wurden keine signifikanten Unterschiede zwischen den beiden Techniken beobachtet. Die durchschnittliche T_2^* Zeit im Myokardium betrug 14 ms, je nach Herzsegment wurden Werte zwischen 10.6 ms und 17.2 ms beobachtet (Abbildung 5).

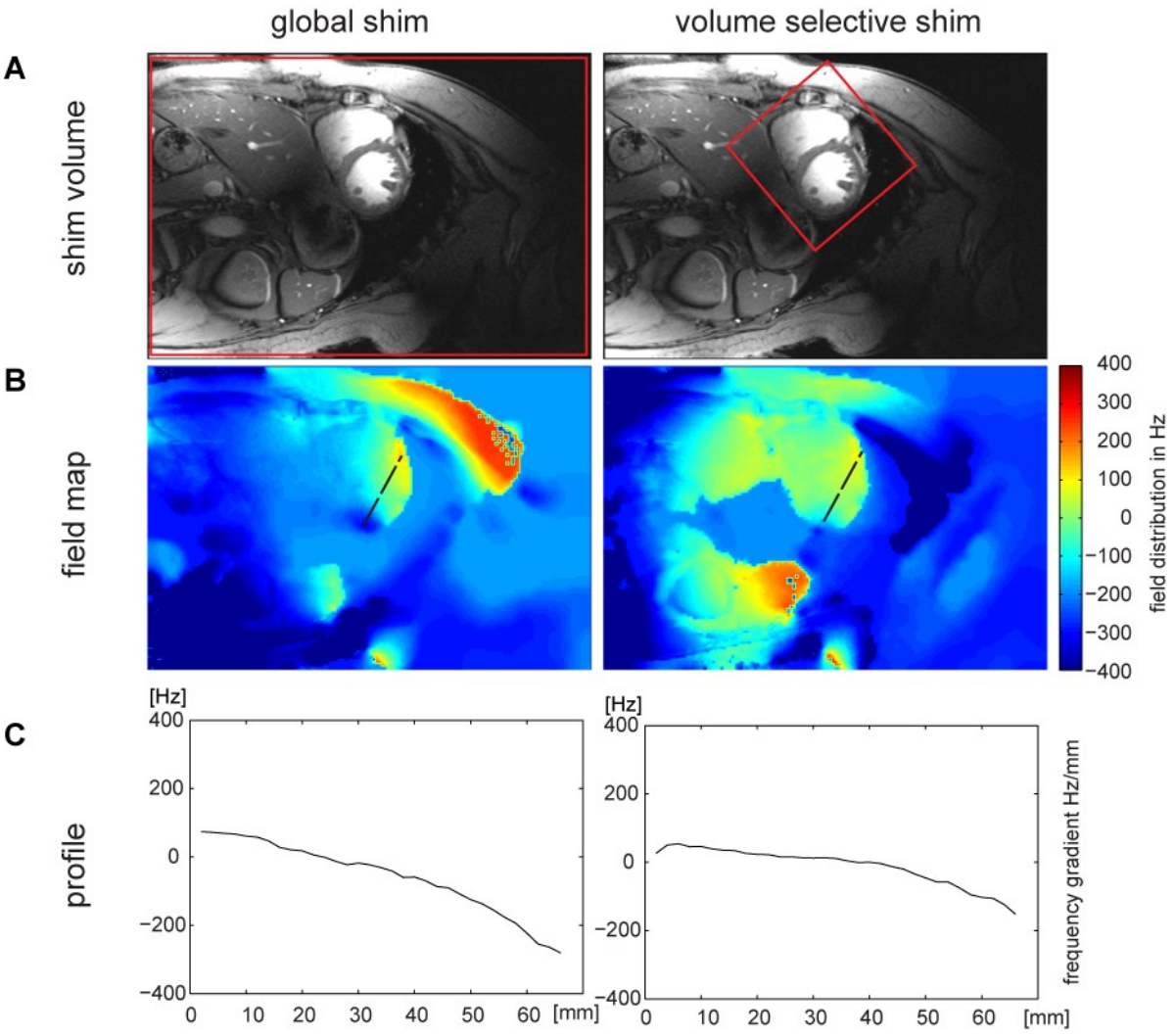

Abbildung 4: Vergleich der Magnetfeldverteilung vor und nach Volumen Selektiven Shim

Eine detaillierte Betrachtung der T_2^* Zeiten im Verlauf des Herzzyklus zeigte einen Anstieg von T_2^* während der diastolischen Phasen, welcher insbesondere im Septum deutlich erkennbar war. Über alle Probanden gemittelt zeigte sich eine um (27 ± 6)% erhöhte T_2^* Zeit während der Diastole im Vergleich zur Systole (Abbildung 6). Ein gepaarter T-Test welcher enddiastolische und endsystolische MS-GRE und MB CINE Karten vergleicht, zeigte die Signifikanz dieser Veränderung (P=0.002 für MS-GRE und p=0.001 für MB CINE).

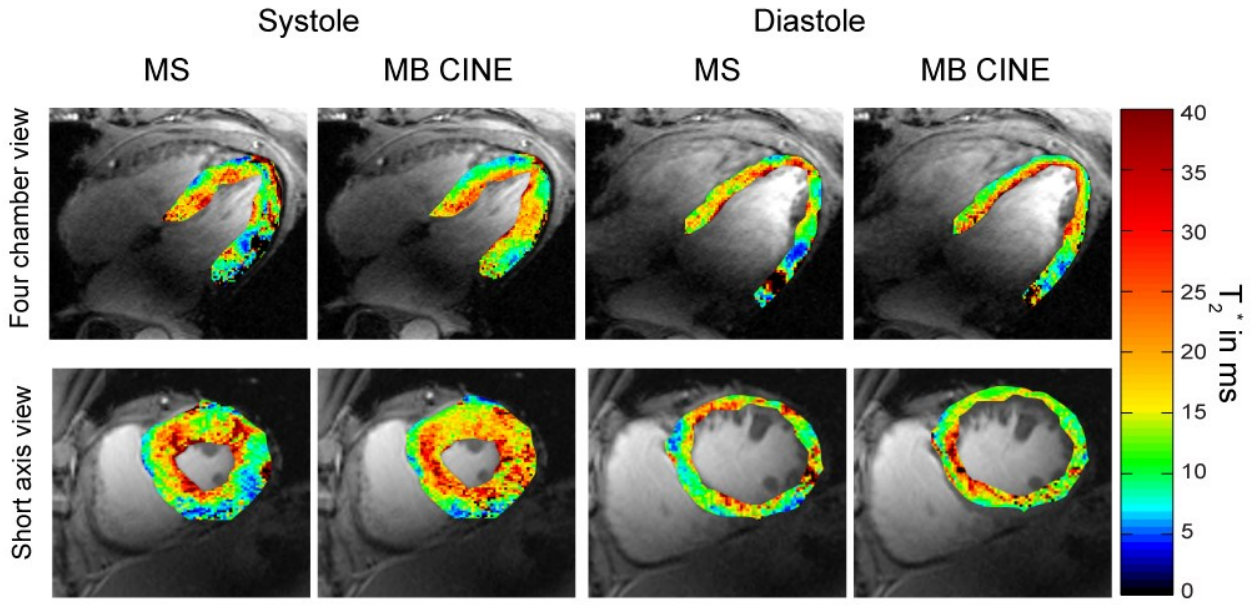

Abbildung 5: T_2^* Karten von MS und MB CINE während Systole und Diastole

Suszeptibilitätsgewichtete Spin-Echo Bildgebung

UFLARE basierte T_2^* Karten des Phantoms wiesen auch für starke T_2^* Wichtungen keine geometrischen Verzerrungen oder Signalauslöschungen aufgrund von B_0 Inhomogenitäten auf. Im Gegensatz dazu zeigten GRE-EPI basierte Karten Verzerrungen bis zu 1 cm entlang der Phasenkodierungsrichtung. Die mittels UFLARE und ME-GRE ermittelten T_2^* Werte des Phantoms stimmten überein (22.65 ± 0.89 ms versus 22.82 ± 0.79 ms). Abbildung 7 zeigt unterschiedlich stark T_2^* gewichtete Kurzachsenblicke des Herzens bei 1.5 T und 3 T mit den dazugehörigen T_2^* Karten. T_2^* Zeiten im Septum betrugen 29.9 ± 6.6 ms bei 1.5 T und 22.3 ± 4.8 ms bei 3 T.

Feldstärkenvergleich

Die Artefaktstärke der R_2^* Karten war bei 7 T signifikant erhöht gegenüber 1.5 T, nicht jedoch im Vergleich zu 3 T. Dabei waren die Artefakte in der inferolateralen Wand am stärksten ausgeprägt, wobei im Septum eine ähnlich geringe Artefaktstärke wie bei 1.5 T und 3 T beobachtet wurde. Die mittleren R_2^* Werte zeigten einen linearen Zusammenhang zur magnetischen Feldstärke; dabei war die Änderung der globalen R_2^* Zeiten stärker ausgeprägt als die der lokalen.

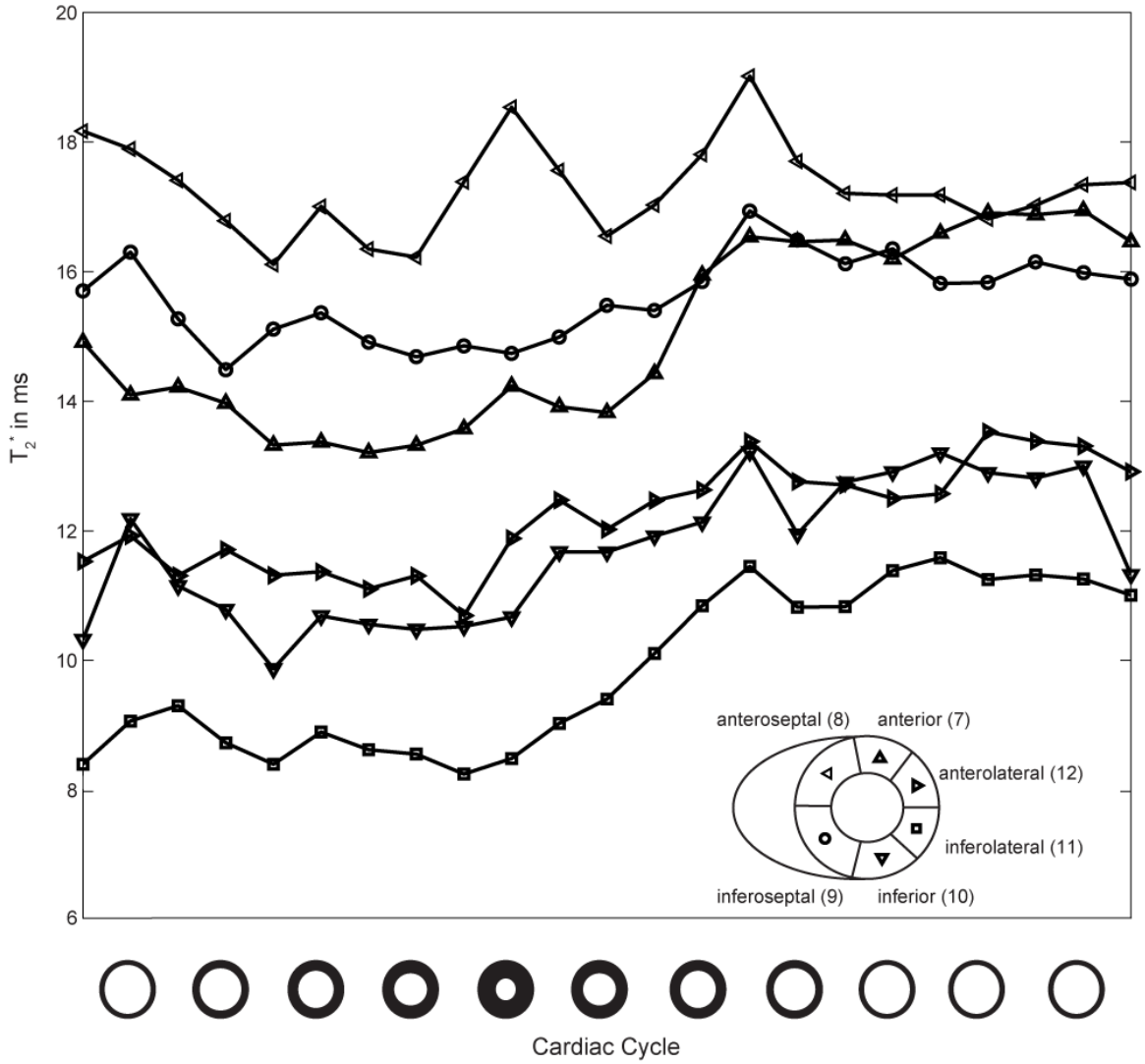

Abbildung 6: T_2^* Zeiten für verschiedene Herzsegmente über den Herzzyklus

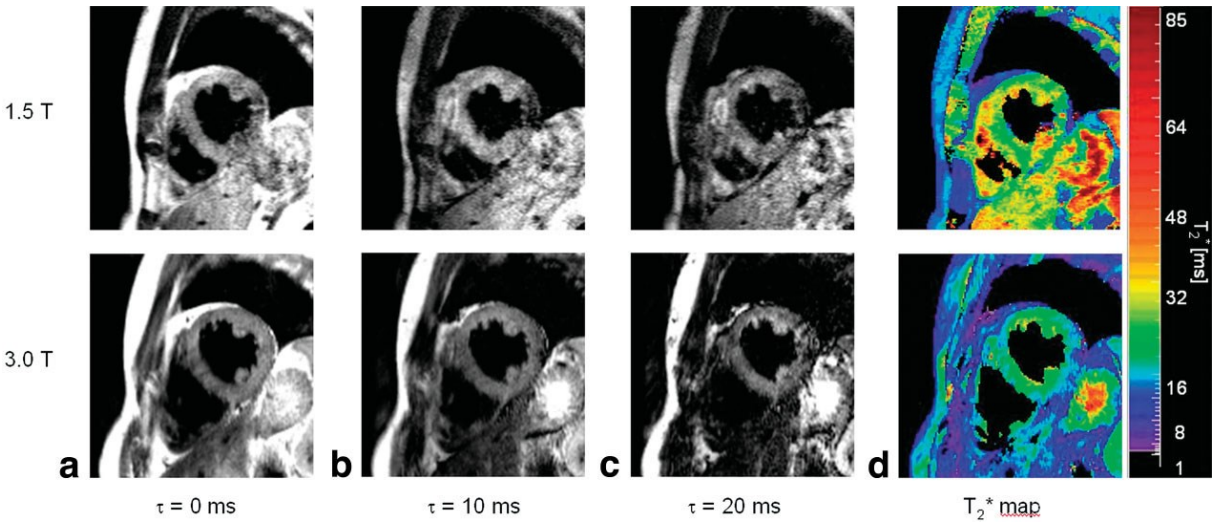

Abbildung 7 T_2^* gewichtete Kurzachsenblicke des Herzens bei 1.5 T und 3 T mit den dazugehörigen T_2^* Karten

Vorarbeiten zur Herzbildgebung bei 7 T

16-Kanal Sende- und Empfangsspule zur Herzbildgebung bei 7 T

Die für ein Phantom simulierte B_1^+ Verteilung wurde anhand von experimentellen Daten validiert. Für die Probandenstudie wurde anhand dessen eine Worst-Case B_1^+ Verteilung simuliert und die Leistungsgrenzen daran angepasst, sodass selbst bei konstruktiven Inferenzen bestehende SAR Grenzwerte nicht überschritten wurden. Die B_1^+ Effizienz und Verteilung wurde in in-vivo Experimenten weiter verbessert, indem destruktive Interferenzen mittels Phasenversätzen so verschoben wurden, dass sie die Bildgebung des Herzen nicht beeinträchtigen (Abbildung 8). Eine Analyse der Bildqualität für Beschleunigungsfaktoren von R=2 bis R=4 ergab klinisch akzeptable Ergebnisse bis R=4. Im Vergleich zur den 4 Kanal beziehungsweise 8 Kanal Spulen zeigte sich die 16 Kanal Spule überlegen hinsichtlich SNR, Geometrie Faktor und Bildqualität.

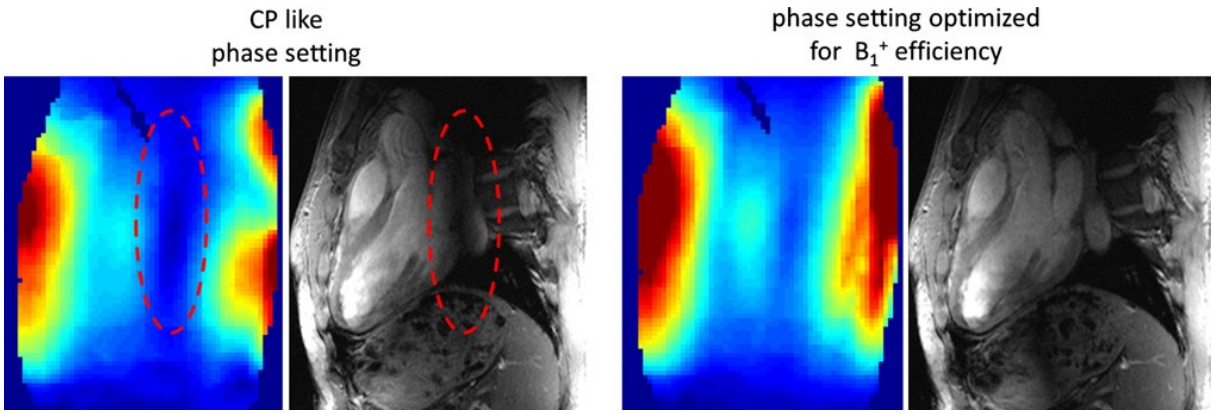

Abbildung 8: Vergleich B_1^+ Verteilung nach und vor Phasenoptimierung

Akustische Triggerung

Die Herzfunktionsparameter, die mittels EKG und akustisch synchronisierter Bilddaten bestimmt wurden, wiesen bei 1.5 T und 3 T keine Unterschiede auf. Akustisch synchronisierte zeigten jedoch Daten eine leicht verbesserte Kantenschärfe gegenüber EKG getriggerten Bilddaten. Die Analyse von bei 7 T aufgenommen EKG Daten ergab in etwa 30 % der Fälle falsche Triggerinformationen, da die R-Zacke nicht korrekt erkannt wurde. Abbildung 9 zeigt CINE Daten der drei Triggertechniken und die dazugehörigen Triggerpunkte. Die Genauigkeit in der Erkennung des Triggerpunktes wies bei der Pulsoxymetrie Schwankungen von etwa 72 ms auf, wohingegen die akustische Triggerung nur minimale Schwankungen von 5 ms zeigte.

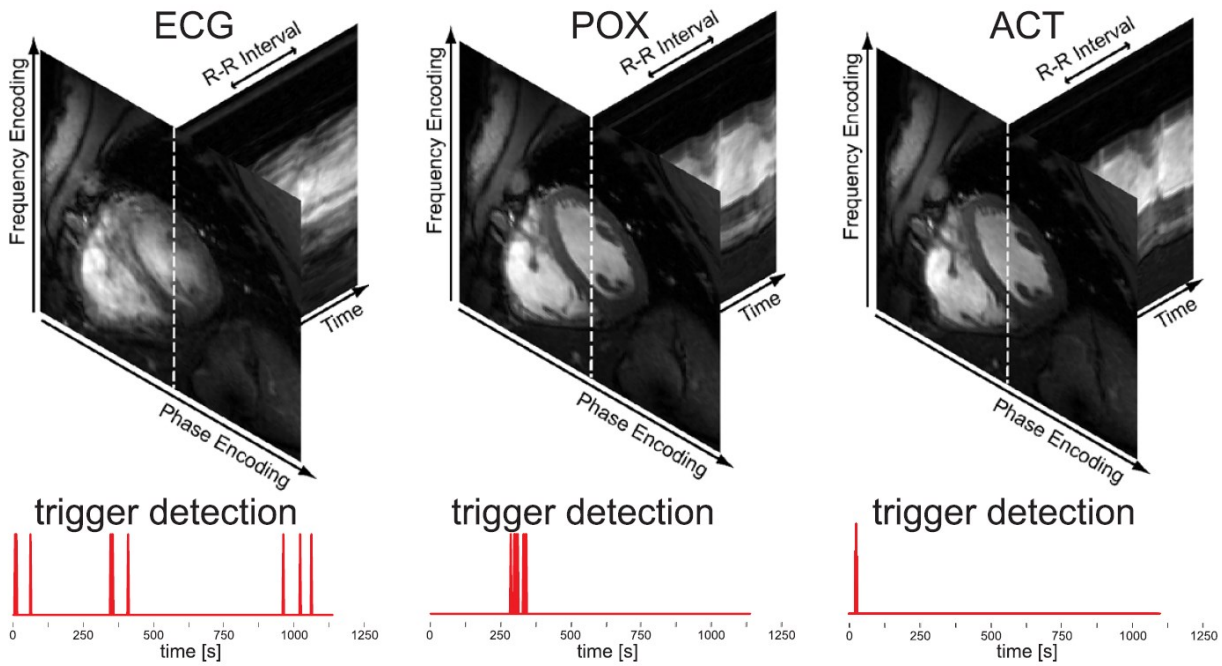

Abbildung 9: Vergleich von EKG, Pulsoxymetrie und akustisch getriggerter CINE Bildgebung bei 7 T.

Diskussion

In dieser Arbeit wird erstmals demonstriert, dass T_2^* gewichtete Bildgebung am Herzen bei 7T möglich ist. Für 7 T angepasste GRE Techniken wurden dazu an Phantomen und gesunden Probanden getestet und mit bei 1.5 T und 3 T etablierten Techniken verglichen. Der SNR Vorteil der Ultrahochfeld MRT wurde in eine Verbesserung der zeitlichen und räumlichen Auflösung der T_2^* Karten umgesetzt. Die erreichte hohe räumliche Auflösung von 1.1 x 1.1 x 2.5 mm^3 ist etwa um Faktor 6 gegenüber heute üblichen Werten verbessert und stellt dabei einen Kompromiss zwischen SNR Erwägungen, Voxeldephasierungseffekten und Gradientenbeschränkungen dar.

Diese Arbeit liefert erste Werte für T_2^* am menschlichen Herzen bei 7 T. Die gemessenen T_2^* Zeiten liegen zwischen 9 ms und 18 ms abhängig zum einen von der Position im Herzmuskel und zum anderen vom Zeitpunkt innerhalb des Herzzyklus. Eine bestehende Limitation ist, dass die durchgeführte Studie eine limitierte Anzahl von gesunden Probanden aus einem Zentrum umfasst. Dennoch stellt sie eine wichtige Vorarbeit für eine folgende größere Studie an gesunden Probanden und Patienten dar. Solch eine Studie könnte T_2^* Normwerte für gesundes und pathologisches Myokard etablieren, wie sie bereits für 1.5 T und 3 T existieren.

T_2^* gewichtete Bildgebung bei 7 T bietet die Möglichkeit Änderungen der Sauerstoffsättigung im Herzmuskel zu visualisieren und zu quantifizieren. Bestehende Limitationen bezüglich räumlicher und zeitlicher Auflösung der konventionell eingesetzten Perfusions-Bolusmessungen mit Kontrastmittel könnten dadurch umgangen werden. Der endogene Kontrast des BOLD Effekts ermöglicht es, Änderungen im Gleichgewicht zwischen Sauerstoffversorgung und Sauerstoffnachfrage früh zu erkennen.

Diese Arbeit zeigt auch erstmalig wie sich T_2^* im Verlauf des Herzzyklus ändert. Auf Grund der erhöhten Suszeptibilitätseffekte bei 7 T und die daraus folgenden kurzen notwendigen Echozeiten konnte eine sehr hohe zeitliche Auflösung realisiert werden. Es wurden dabei signifikante Änderungen der T_2^* Zeiten für verschiedene Phasen des Herzzyklus beobachtet. Eine mögliche Erklärung dieser Änderungen ist, dass durch die Kontraktion des Herzmuskels die Nachfrage nach sauerstoffreichem Blut erhöht wird, wodurch T_2^* sinkt. Die zeitlich aufgelöste Darstellung von T_2^* könnte eine Alternative zu pharmakologisch induzierten Stressmessungen darstellen. Mit durch körperliche Anstrengung während einer MR Untersuchung [13] kombinierte T_2^* Kartierung könnte

eine komplett nicht-invasive Charakterisierung der Sauerstoffversorgung des Herzmuskels ermöglicht werden. Dadurch könnten eventuelle minderdurchblutete Bereiche des Myokards frühzeitig erkannt werden.

Die räumliche Auflösung der T_2^* Kartierung bei 7 T ist deutlich höher als in vorherigen Studien bei 1.5 T und 3 T. So lassen sich innerhalb des Myokards Veränderungen der T_2^* Zeiten von den epikardialen zu den endokardialen Schichten erkennen. Im Vergleich zur ex-vivo MR Mikroskopie basierten T_2^* Kartierung am Rattenherzen [14] ist die Auflösung zwar noch um eine Größenordnung kleiner, jedoch kommt die effektive anatomische Auflösung – Voxelgröße per Anatomie- derjenigen in Tiermodellen sehr nahe. T_2^* gewichtete Bildgebung bei 7 T kann aus diesem Grund auch dazu beitragen um die Mikrostruktur des Herzens in-vivo darzustellen um damit die Muskelfaserstruktur und deren Orientierung zu visualisieren.

Diese Arbeit liefert zudem wichtige Vorarbeiten um mittels Multi-Echo Gradienten Techniken Fett-Wasser getrennte Bilder des Herzen bei 7 T zu erstellen [15] und auf diese Weise Fetteinschlüsse im Herzen zu detektieren. Auch bietet diese Arbeit die Grundlage für eine quantitative Suszeptibilitätskartierung (QSM), wie sie bereits in der neurologischen Bildgebung eingesetzt wird.

Für eine T_2^* gewichtete Bildgebung mittels schnellen Spin-Echo Sequenzen bei 7 T ist das derzeitig verfügbare Anregungsfeld nicht ausreichend stark und homogen genug. Entwicklungen im Bereich mehrkanaliger Sende- und Empfangssystemen, welche die Magnitude und Phase jedes einzelnen Sendekanals unabhängig modulieren, sind vielversprechend. Zusammen mit weiteren Verbesserungen und Weiterentwicklungen im Spulendesign [16] und im Pulsdesign werden zur Zeit bestehende Limitationen für die Spin-Echo basierte T_2^* Kartierung des Herzens reduziert. Damit stellen Spin-Echo basierte T_2^* sensitive Techniken eine vielsprechende Alternative zur Gradienten-Echo basierten Kartierung bei 7 T dar.

Referenzen

1. Friedrich M, Niendorf T, Schulz-Menger J, Gross C, Dietz R (2003) Blood oxygen level-dependent magnetic resonance imaging in patients with stress-induced angina. Circulation 108: 2219 - 2223.
2. Manka R, Paetsch I, Schnackenburg B, Gebker R, Fleck E, et al. (2010) BOLD cardiovascular magnetic resonance at 3.0 tesla in myocardial ischemia. Journal of Cardiovascular Magnetic Resonance 12: 54.
3. Friedrich MG, Niendorf T, Schulz-Menger J, Gross CM, Dietz R (2003) Blood oxygen level-dependent magnetic resonance imaging in patients with stress-induced angina. Circulation 108: 2219-2223.
4. Dharmakumar R, Arumana JM, Tang R, Harris K, Zhang Z, et al. (2008) Assessment of regional myocardial oxygenation changes in the presence of coronary artery stenosis with balanced SSFP imaging at 3.0 T: theory and experimental evaluation in canines. Journal of Magnetic Resonance Imaging: JMRI 27: 1037-1045.
5. Hezel F, Thalhammer C, Waiczies S, Schulz-Menger J, Niendorf T (2012) High spatial resolution and temporally resolved T2* mapping of normal human myocardium at 7.0 Tesla: an ultrahigh field magnetic resonance feasibility study. PLoS One 7: e52324.
6. Meloni A, Hezel F, Positano V, Keilberg P, Pepe A, et al. (2013) Detailing magnetic field strength dependence and segmental artifact distribution of myocardial effective transverse relaxation rate at 1.5, 3.0, and 7.0 T. Magn Reson Med. 2014 Jun;71(6):2224-30
7. Heinrichs U, Utting JF, Frauenrath T, Hezel F, Krombach GA, et al. (2009) Myocardial T2* mapping free of distortion using susceptibility-weighted fast spin-echo imaging: a feasibility study at 1.5 T and 3.0 T. Magn Reson Med 62: 822-828.
8. Thalhammer C, Renz W, Winter L, Hezel F, Rieger J, et al. (2012) A Two-dimensional Sixteen Channel Transmit/Receive Coil Array for Cardiac MRI at 7.0 Tesla: Design, Evaluation and Application. J Magn Reson Imaging. 2012 Oct;36(4):847-57
9. Winter L, Kellman P, Renz W, Grassl A, Hezel F, et al. (2012) Comparison of three multichannel transmit/receive radiofrequency coil configurations for anatomic and functional cardiac MRI at 7.0T: implications for clinical imaging. Eur Radiol.
10. Frauenrath T, Hezel F, Heinrichs U, Kozerke S, Utting JF, et al. (2009) Feasibility of cardiac gating free of interference with electro-magnetic fields at 1.5 Tesla, 3.0 Tesla and 7.0 Tesla using an MR-stethoscope. Investigative Radiology 44: 539-547.
11. Becker M, Frauenrath T, Hezel F, Krombach GA, Kremer U, et al. (2010) Comparison of left ventricular function assessment using phonocardiogram- and electrocardiogram-triggered 2D SSFP CINE MR imaging at 1.5 T and 3.0 T. Eur Radiol 20: 1344-1355.
12. Frauenrath T, Hezel F, Renz W, d'Orth Tde G, Dieringer M, et al. (2010) Acoustic cardiac triggering: a practical solution for synchronization and gating of cardiovascular magnetic resonance at 7 Tesla. J Cardiovasc Magn Reson 12: 67.
13. von Knobelsdorff-Brenkenhoff F, Dieringer MA, Fuchs K, Hezel F, Niendorf T, et al. (2013) Isometric handgrip exercise during cardiovascular magnetic resonance imaging: set-up and cardiovascular effects. J Magn Reson Imaging 37: 1342-1350.

14. Köhler S, Hiller KH, Waller C, Jakob PM, Bauer WR, et al. (2003) Visualization of myocardial microstructure using high-resolution T*2 imaging at high magnetic field. Magn Reson Med 49: 371-375.
15. Niendorf T, Graessl A, Thalhammer C, Dieringer MA, Kraus O, et al. (2013) Progress and promises of human cardiac magnetic resonance at ultrahigh fields: a physics perspective. J Magn Reson 229: 208-222.
16. Graessl A, Renz W, Hezel F, Dieringer MA, Winter L, et al. (2013) Modular 32-channel transceiver coil array for cardiac MRI at 7.0T. Magn Reson Med.in Press

Eidesstattliche Versicherung

„Ich, Fabian Hezel, versichere an Eides statt durch meine eigenhändige Unterschrift, dass ich die vorgelegte Dissertation mit dem Thema: „Parametrische suszeptibiltäts-gewichtete Bildgebung des Myokards mittels Magnetresonanzbildgebung bei hohen Magnetfeldern: Methodenentwicklung und Anwendung“ selbstständig und ohne nicht offengelegte Hilfe Dritter verfasst und keine anderen als die angegebenen Quellen und Hilfsmittel genutzt habe.

Alle Stellen, die wörtlich oder dem Sinne nach auf Publikationen oder Vorträgen anderer Autoren beruhen, sind als solche in korrekter Zitierung (siehe „Uniform Requirements for Manuscripts (URM)“ des ICMJE -*www.**icmje**.org*) kenntlich gemacht. Die Abschnitte zu Methodik (insbesondere praktische Arbeiten, Laborbestimmungen, statistische Aufarbeitung) und Resultaten (insbesondere Abbildungen, Graphiken und Tabellen) entsprechen den URM (s.o) und werden von mir verantwortet.

Mein Anteil an der ausgewählten Publikationen entspricht dem, der in der untenstehenden gemeinsamen Erklärung mit dem/der Betreuer/in, angegeben ist.

Die Bedeutung dieser eidesstattlichen Versicherung und die strafrechtlichen Folgen einer unwahren eidesstattlichen Versicherung (§156,161 des Strafgesetzbuches) sind mir bekannt und bewusst.

_____

Datum Unterschrift

Ausführliche Anteilserklärung an den erfolgten Publikationen

1. **High spatial resolution and temporally resolved T_2^* mapping of normal human myocardium at 7.0 Tesla: an ultrahigh field magnetic resonance feasibility study.**
   Hezel F, Thalhammer C, Waiczies S, Schulz-Menger J, Niendorf T
   PLoS One.2012;7(12):e52324

   Beitrag im Einzelnen:

   - Literaturrecherche und Problemanalyse
   - Auswahl geeigneter MR-Techniken, Sequenzdesign und Programmierung
   - Experimentelles Design, Protokollerstellung, Aufbau und Durchführung
   - Erstellung der Datenanalysewerkzeuge
   - Datennachverarbeitung und –auswertung
   - Datenanalyse und statistische Auswertung
   - Manuskript- und Abbildungserstellung

2. **Myocardial T_2^* Mapping Free of Distortion Using Susceptibility-Weighted Fast Spin-Echo Imaging: A Feasibility Study at 1.5 T and 3.0 T**
   Heinrichs U, Utting JF, Frauenrath T, **Hezel F**, Krombach GA, Hodenius MA, Kozerke S, Niendorf T
   Magn Reson Med. 2009 Sep;62(3):822-8

   Beitrag im Einzelnen:

   - Experimentdurchführung
   - MR Protokoll Anpassungen
   - Manuskript Überarbeitung

3. **Feasibility of Cardiac Gating Free of Interference With Electro-Magnetic Fields at 1.5 Tesla, 3.0 Tesla and 7.0 Tesla Using an MR-Stethoscope**
   Frauenrath T, **Hezel F**, Heinrichs U, Kozerke S, Utting JF, Kob M, Butenweg C, Boesiger P, Niendorf T
   Invest Radiol. 2009 Sep;44(9):539-47

Beitrag im Einzelnen:

- Konzeptionelle Erarbeitung und Erstellung vom Datenanalysewerkzeugen für die Bestimmung der endokardialen Kantenschärfe
- MR Protokoll Anpassungen
- Datenaufnahme
- Manuskript Überarbeitung
- Abbildungserstellung

4. **Comparison of left ventricular function assessment using phonocardiogram- and electrocardiogram-triggered 2D SSFP CINE MR imaging at 1.5 T and 3.0 T**

   Becker M, Frauenrath T, **Hezel F**, Krombach GA, Kremer U, Koppers B, Butenweg C, Goemmel A, Utting JF, Schulz-Menger J, Niendorf T.

   Eur Radiol. 2010 Jun;20(6):1344-55

   Beitrag im Einzelnen:

   - Erstellung vom Datenanalysewerkzeugen zur Bestimmung der endokardialen Kantenschärfe Datenauswertung
   - Manuskript Überarbeitung
   - Abbildungserstellung

5. **Cardiac chamber quantification using magnetic resonance imaging at 7 Tesla - A pilot study**

   von Knobelsdorff-Brenkenhoff F, Frauenrath T, Prothmann M, Dieringer MA, **Hezel F**, Renz W, Kretschel K, Niendorf T, Schulz-Menger J.

   Eur Radiol. 2010 Dec;20(12):2844-52.

   Beitrag im Einzelnen:

   - MR Protokoll Anpassungen
   - Datenaufnahme
   - Datenauswertung
   - Manuskript Überarbeitung

6. **Acoustic cardiac triggering: a practical solution for synchronization and gating of cardiovascular magnetic resonance at 7 Tesla**

   Frauenrath T, **Hezel F**, Renz W, d'Orth Tde G, Dieringer M, von Knobelsdorff-Brenkenhoff F, Prothmann M, Schulz Menger J, Niendorf T.

   J Cardiovasc Magn Reson. 2010 Nov 16;12:67

Beitrag im Einzelnen:

- Endokardiale Kantenschärfe Bestimmung
- Statistische Auswertung
- Manuskript Überarbeitung
- Abbildungserstellung

7. **Comparison of three multichannel transmit/receive radiofrequency coil configurations for anatomic and functional cardiac MRI at 7.0T: Implications for clinical imaging**
   Winter L, Kellman P, Renz W, Gräßl A, **Hezel F**, Thalhammer C, von Knobelsdorff-Brenkenhoff F, Tkachenko V, Schulz-Menger J, Niendorf T.
   Eur Radiol. 2012 Oct;22(10):2211-20

   Beitrag im Einzelnen:

   - SNR und g-Maps Auswertung
   - MR Protokoll Anpassungen
   - Manuskript Überarbeitung

8. **Two-Dimensional Sixteen Channel Transmit/Receive Coil Array for Cardiac MRI at 7.0 T: Design, Evaluation, and Application**
   Thalhammer C, Renz W, Winter L, **Hezel F**, Rieger J, Pfeiffer H, Graessl A, Seifert F, Hoffmann W, von Knobelsdorff-Brenkenhoff F, Tkachenko V, Schulz-Menger J, Kellman P, Niendorf T.
   J Magn Reson Imaging. 2012 Oct;36(4):847-57

   Beitrag im Einzelnen:

   - Experimentdurchführung und Datenaufnahme
   - Anpassung und Feinabstimmung der HF-Spulenhardware (Phaseneinstellungen)
   - T_2^* Mapping und Fett-Wasser Trennung Datenerstellung
   - Datenauswertung
   - SNR und g-Maps Auswertung
   - Manuskript Überarbeitung

9. **Progress and promises of human cardiac magnetic resonance at ultrahigh fields: A physics perspective**

   Niendorf T, Graessl A, Thalhammer C, Dieringer MA, Kraus O, Santoro D, Fuchs K, Hezel F, Waiczies S, Ittermann B, Winter L

   J Magn Reson. 2012 Nov 29

   Beitrag im Einzelnen:

   - Manuskript Überarbeitung
   - Abbildungserstellung

10. **Isometric Handgrip Exercise During Cardiovascular Magnetic Resonance Imaging: Set-up and Cardiovascular Effects**

    von Knobelsdorff-Brenkenhoff F, Dieringer MA, Fuchs K, **Hezel F**, Niendorf T, Schulz-Menger J

    J Magn Reson Imaging. 2013 Jan 24

    Beitrag im Einzelnen:

    - Experimentaufbau
    - Manuskript Überarbeitung

11. **Assessment of the right ventricle with cardiovascular magnetic resonance at 7 Tesla**

    von Knobelsdorff-Brenkenhoff, F ,Tkachenko V , Winter L, Rieger J, Thalhammer C, **Hezel F**, Graessl A, Dieringer MA, Niendorf T, Schulz-Menger J.

    J Cardiovasc Magn Reson. 2013 Mar 14;15:23.

    Beitrag im Einzelnen:

    - Datenauswertung
    - MR Protokoll Anpassungen
    - Manuskript Überarbeitung

12. **Detailing Magnetic Field Strength Dependence and Segmental Artifact Distribution of Myocardial Effective Transverse Relaxation Rate at 1.5, 3.0, and 7.0 T**

    Meloni A, **Hezel F**, Positano V, Keilberg P, Pepe A, Lombardi M, Niendorf T

    Magn Reson Med. 2014 Jun;71(6):2224-30

Beitrag im Einzelnen:

- Experimentdurchführung
- Datenaufnahme
- Datenanalyse
- MR Protokoll Anpassungen
- Manuskript Überarbeitung

13. Modular 32-channel transceiver coil array for cardiac MRI at 7.0 T

Graessl A, Renz W, Hezel F, Dieringer MA, Winter L, Oezerdem C, Rieger J, Kellman P, Santoro D, Lindel TD, Frauenrath T, Pfeiffer H, Niendorf T.

Magn Reson Med. 2013 Jul 31. [online verfügbar, noch nicht gedruckt]

Beitrag im Einzelnen:

- Experimentdurchführung
- SNR und g-Maps Auswertung
- T_2^* Mapping und Fett-Wasser Trennung Datenerstellung
- Abbildungserstellung
- MR Protokoll Anpassungen
- Manuskript Überarbeitung

Unterschrift, Datum und Stempel des betreuenden Hochschullehrers/der betreuenden Hochschullehrerin

_____

Prof. Dr. Thoralf Niendorf

Unterschrift des Doktoranden/der Doktorandin

_____

Fabian Hezel

OPEN ACCESS Freely available online

PLOS ONE

High Spatial Resolution and Temporally Resolved T_2^* Mapping of Normal Human Myocardium at 7.0 Tesla: An Ultrahigh Field Magnetic Resonance Feasibility Study

Fabian Hezel[1], Christof Thalhammer[1], Sonia Waiczies[1,2], Jeanette Schulz-Menger[1,2,3], Thoralf Niendorf[1,2]*

1 Berlin Ultrahigh Field Facility (B.U.F.F.), Max Delbrueck Center for Molecular Medicine, Berlin, Germany, **2** Experimental and Clinical Research Center, a Joint Cooperation between the Charité Medical Faculty and the Max Delbrueck Center for Molecular Medicine, Campus Berlin Buch, Berlin, Germany, **3** Department of Cardiology and Nephrology, HELIOS Klinikum Berlin Buch, Berlin, Germany

Abstract

Myocardial tissue characterization using T_2^* relaxation mapping techniques is an emerging application of (pre)clinical cardiovascular magnetic resonance imaging. The increase in microscopic susceptibility at higher magnetic field strengths renders myocardial T_2^* mapping at ultrahigh magnetic fields conceptually appealing. This work demonstrates the feasibility of myocardial T_2^* imaging at 7.0 T and examines the applicability of temporally-resolved and high spatial resolution myocardial T_2^* mapping. In phantom experiments single cardiac phase and dynamic (CINE) gradient echo imaging techniques provided similar T_2^* maps. *In vivo* studies showed that the peak-to-peak B_0 difference following volume selective shimming was reduced to approximately 80 Hz for the four chamber view and mid-ventricular short axis view of the heart and to 65 Hz for the left ventricle. No severe susceptibility artifacts were detected in the septum and in the lateral wall for T_2^* weighting ranging from TE = 2.04 ms to TE = 10.2 ms. For TE >7 ms, a susceptibility weighting induced signal void was observed within the anterior and inferior myocardial segments. The longest T_2^* values were found for anterior (T_2^* = 14.0 ms), anteroseptal (T_2^* = 17.2 ms) and inferoseptal (T_2^* = 16.5 ms) myocardial segments. Shorter T_2^* values were observed for inferior (T_2^* = 10.6 ms) and inferolateral (T_2^* = 11.4 ms) segments. A significant difference ($p = 0.002$) in T_2^* values was observed between end-diastole and end-systole with T_2^* changes of up to approximately 27% over the cardiac cycle which were pronounced in the septum. To conclude, these results underscore the challenges of myocardial T_2^* mapping at 7.0 T but demonstrate that these issues can be offset by using tailored shimming techniques and dedicated acquisition schemes.

Citation: Hezel F, Thalhammer C, Waiczies S, Schulz-Menger J, Niendorf T (2012) High Spatial Resolution and Temporally Resolved T_2^* Mapping of Normal Human Myocardium at 7.0 Tesla: An Ultrahigh Field Magnetic Resonance Feasibility Study. PLoS ONE 7(12): e52324. doi:10.1371/journal.pone.0052324

Editor: Wolfgang Rudolf Bauer, University Hospital of Würzburg, Germany

Received July 23, 2012; **Accepted** November 16, 2012; **Published** December 14, 2012

Funding: This study was founded through institutional funding provided by the Max Delbrück Centrum for Molecular Medicine. The funders had no role in study design, data collection and analysis, decision to publish, or preparation of the manuscript.

Competing Interests: TN is founder of MRI.Tools GmbH. This does not alter the authors' adherence to all the PLOS ONE policies on sharing data and materials. The authors would also like to point out that there are no patents, products in development or marketed products to declare.

* E-mail: Thoralf.Niendorf@mdc-berlin.de

Introduction

Emerging cardiovascular magnetic resonance (CMR) imaging applications include T_2^* relaxation sensitized techniques, which are increasingly used in basic research and (pre)clinical imaging. Methodological developments in T_2^* sensitized imaging [1–4] and simulations of myocardial vasculature [5,6] have been indispensable. Applications include investigation of the microstructure of the isolated rat heart [7], detection of myocardial ischemia [8–14], probing of vasodilator or dipyridamole-induced changes in myocardial perfusion [15–18], visualization of scarred myocardium [19], imaging of capillary recruitment [20] and assessment of tissue oxygenation related to endothelium-dependent blood flow changes [21]. T_2^* mapping has also been shown to be of substantial clinical value for the ascertainment of myocardial iron levels [22–29].

The most widely used methods for T_2^* mapping are echo planar imaging (EPI) and gradient echo based techniques. Unlike conventional CINE gradient echo imaging, the relatively strong T_2^*-weighting required to make gradient echo sequences sensitive to changes in magnetic susceptibility asks for a long evolution time (TE) between RF excitation and data acquisition. Consequently, gradient echo based myocardial T_2^* mapping is commonly restricted to a single slice and single cardiac phase that can be accommodated in a single breath-hold at 1.5 T and 3.0 T [30–32].

The linear relationship between magnetic field strength and microscopic susceptibility [33–35] renders it conceptually appealing to pursue myocardial T_2^* mapping at ultrahigh magnetic field strengths. Realizing the opportunities and challenges of T_2^* mapping, this pilot study demonstrates the feasibility of ultrahigh field susceptibility-weighted myocardial imaging and examines its applicability for temporally-resolved and high spatial resolution myocardial T_2^* mapping at 7.0 T. To meet this goal, the applicability of 2D spoiled gradient-echo multi-echo based techniques for T_2^* mapping at 7.0 T is closely investigated in phantom experiments. The feasibility of gradient-echo multi-echo based techniques for fast CINE T_2^* mapping of the human heart is

demonstrated at 7.0 T. We also present the suitability of this technique for high spatial resolution myocardial T_2^* mapping by using thin slices (slice thickness = 2.5 mm) and in-plane spatial resolution of (1.1×1.1) mm^2. Our initial volunteer studies serve as a mandatory precursor to a broader clinical study. The merits and limitations of T_2^* mapping using 2D spoiled gradient-echo multi-echo imaging at 7.0 T are discussed and implications for cardiac MR at 7.0 T are considered.

Methods

MR-Hardware

Imaging was conducted using a 7.0 T whole body MR scanner (Magnetom, Siemens Healthcare, Erlangen, Germany) equipped with a gradient system (Avanto, Siemens Healthcare, Erlangen, Germany) capable of supporting a slew rate of 200 mT/m/ms and a maximum gradient strength of 40 mT/m. A 16 channel transmit/receive coil array was used for excitation and signal reception. The coil was designed for cardiac imaging and comprises an anterior and posterior former, each laid out on a two-dimensional 2 by 4 grid of loop elements. For further details about the coil please see [36,37]. An MR stethoscope (EasyACT, MRI.TOOLS GmbH, Berlin, Germany) was used for cardiac triggering [38,39].

T_2^* Mapping Techniques

Myocardial T_2^* mapping is commonly conducted with cardiac triggered, segmented multi-echo spoiled gradient echo (**ME**) techniques that use breath-held acquisitions for respiratory motion compensation [8,9,15,18,40]. In this work, various ME configurations have been used for (i) time resolved CINE and for (ii) single cardiac phase acquisitions (Figure 1).

For single cardiac phase imaging, the acquisition period is commonly placed into end-diastole, which limits the viable window of data acquisition to 100 ms to 200 ms. Data acquisition is segmented over a series of cardiac cycles with each segment acquiring a set of echoes during the quiescent interval (Figure 1a). The number of segments and echoes per segment are dictated by the longest TE used for T_2^* weighting as outlined in Figure 1a. To avoid T_2^* errors due to signal modulations induced by fat-water phase shift, it is essential to choose echo times where fat and water are in-phase [4]. At 1.5 T and 3.0 T TE increments equivalent to the fat-water shift are 4.4 ms and 2.2 ms, respectively. At 7.0 T this inter echo time is 1.02 ms, which is beneficial for rapid multi-echo acquisitions. However, if a larger data matrix size is needed for high spatial resolution T_2^* mapping, the readout/acquisition window can easily exceed 1.02 ms even when short dwell times are used. Consequently, it is elusive to accomplish inter-echo time increments of 1.02 ms for high spatial resolution T_2^* mapping at 7.0 T using sequential multi echo gradient echo imaging.

CINE T_2^* mapping might be feasible at 7.0 T assuming a T_2^* reduction at 7.0 T versus 1.5 T and 3.0 T and considering the relationship between proper T_2^* weighting and range of echo times to be covered. To this end, a maximum TE = 10 ms would be compatible with the needs of CINE imaging but would also provide sufficient coverage of the T_2^* decay at 7.0 T.

For all these reasons, two imaging strategies were employed at 7.0 T:

i. Interleaved multi-shot multi-echo (**MS**) gradient echo technique for single cardiac phase myocardial T_2^* mapping (Figure 1b). This approach addresses the competing constraints of inter echo time and spatial resolution of the **ME** approach by adding more excitations and by interleaving the echoes.
ii. Multi-breath-hold multi-echo (**MB CINE**) gradient echo technique for CINE myocardial T_2^* mapping (Figure 1c). This approach runs the trait that all k-space lines required to form the final image for a given echo time are acquired in a single breathhold.

Phantom Studies

For the evaluation of **MS** and **MB CINE** T_2^* mapping strategies, phantom experiments were conducted using a long T_2^* and medium T_2^* phantom. For long T_2^*, a cylindrical water phantom (diameter = 15 cm) containing an agarose copper sulfate solution (4 g $CuSO_4$ +2 g NaCl +2 g agarose dissolved in 1.0 l H_2O) was used. A glass capillary (inner diameter = 0.5 mm) filled with air and a tube (inner diameter = 5 mm) filled with water were placed inside the phantom to create strong susceptibility gradients of limited spatial extension within the uniform phantom. For the medium T_2^* phantom, a cylindrical water phantom (diameter = 8 cm) containing agarose (5 mg agarose dissolved in 250 ml H_2O) was used. T_2^* was reduced by ultrasmall superparamagnetic iron oxide particles (500 µl Molday ION (10 mg Fe/ml), BioPal, Worchester, USA), which afforded a T_2^* of approximately 20 ms.

In the phantom experiments, **MS** (Figure 1b) and **MB CINE** (Figure 1c) T_2^* mapping strategies were benchmarked against other T_2^* mapping techniques, which are already established at 1.5 T and 3.0 T but are unsuitable for myocardial T_2^* mapping at 7.0 T due to echo time and acquisition time constraints. These reference methods include:

i. conventional multi-echo (**ME**) gradient echo for single cardiac phase T_2^* mapping (Figure 1a).
ii. multi-echo CINE (**ME CINE**) gradient echo (Figure 1d).
iii. multi-shot multi-echo CINE (**MS CINE**) gradient echo (Figure 1e).

For phantom T_2^* mapping, an image matrix of 320×240, a field of view of (360×270) mm^2, an in-plane resolution of (1.1×1.1) mm^2, and a slice thickness ranging from 2.5 mm to 8 mm were used. A unipolar readout using gradient flyback was applied together with echo times ranging from 2.04 ms to 10.20 ms. This approach results in nine equidistant echoes with an inter echo time of 1.02 ms with the exception of **ME** and **ME CINE** due to gradient switching induced peripheral nerve stimulation constraints. For **ME** and **ME CINE** 6 echoes with an inter echo time of 3.06 ms and a TE_{min} = 2.04 ms were used. For the **MS**, **MS CINE** and **MB CINE** techniques three excitations together with 3 echoes were used to ensure an inter-echo time of 1.02 ms. With the first excitation echo 1, 4 and 7 were acquired. The second excitation covered echo 2, 5 and 8 while echo 3, 6, and 9 were recorded after the third excitation. A simulated heart rate of 60 bpm was used for prospective triggering of the phantom experiments.

Ethics Statement

For the *in vivo* feasibility study, 8 healthy subjects (mean age: 27±3 years, 5 females, mean BMI: 24 kg/m^2, mean heart rate: 78 bpm) without any known history of cardiac disease were included after due approval by the local ethical committee (registration number DE/CA73/5550/09, Landesamt für Arbeitsschutz, Gesundheitsschutz und technische Sicherheit, Berlin,

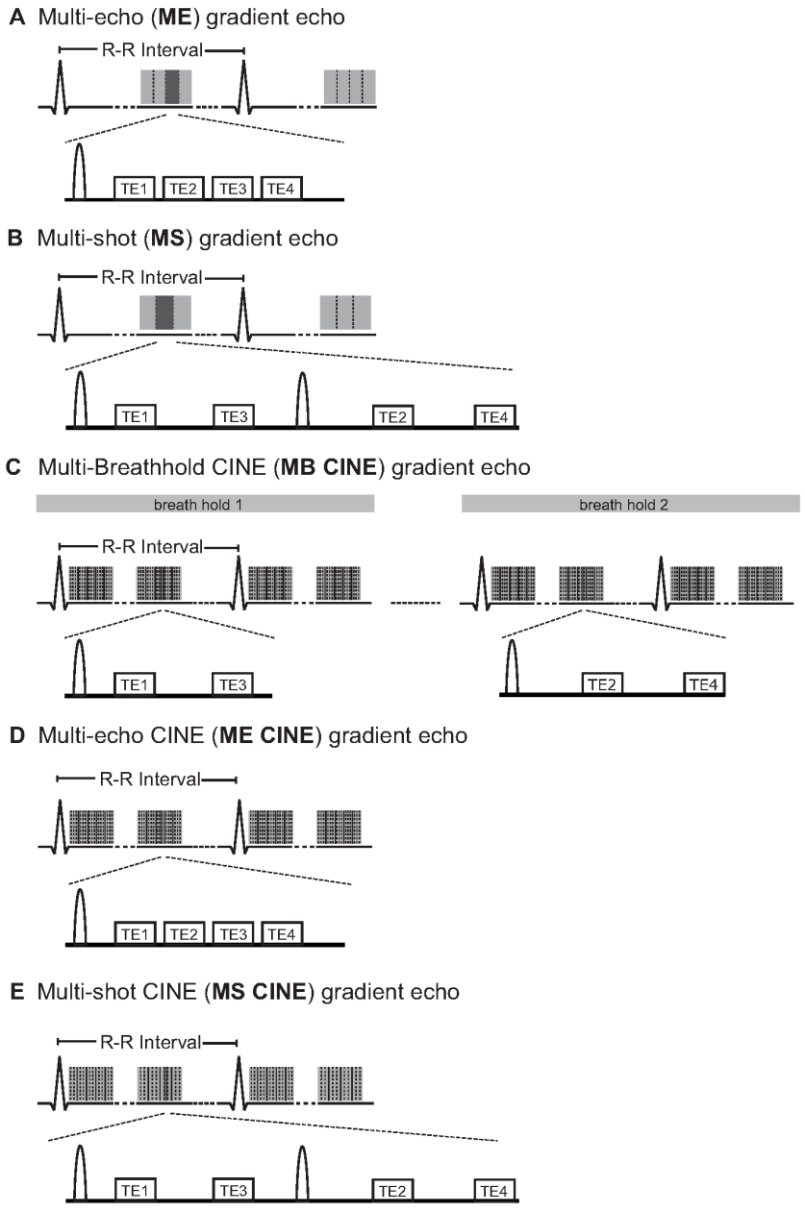

Figure 1. Synopsis of multi-echo gradient echo strategies used for T_2^* mapping at 7.0 T. A). Conventional multi-echo (**ME**) gradient echo for single cardiac phase myocardial T_2^* mapping. Multiple echoes are acquired after excitation to obtain a set of T_2^* weighted images. The competing constraints of inter echo time and spatial resolution inherent to the **ME** approach are addressed by the **B**) interleaved multi-shot multi-echo (**MS**) gradient echo technique. In **MS** a set of excitations is employed together with echo interleaving echoes to acquire a set of T_2^* weighted images. **C**) The multi-breath-hold multi-echo (**MB CINE**) gradient echo technique allows myocardial CINE T_2^* mapping by interleaving the echoes over several breath-holds. For benchmarking **D**) multi-echo CINE (**ME CINE**) gradient echo and **E**) multi-shot multi-echo CINE (**MS CINE**) were applied for T_2^* mapping in phantom studies. To guide the eye vertical dashed lines refer to k-space lines. Vertical solid lines refer to cardiac phases. A unipolar readout using gradient flyback was applied for all strategies.
doi:10.1371/journal.pone.0052324.g001

Germany). Informed written consent was obtained from each volunteer prior to the study.

Volunteer Studies

For each volunteer, slice positioning was carried out following international consensus by the same technician to omit inter-operator variability. Myocardial T_2^* mapping was conducted using the **MS** and the **MB CINE** imaging strategies for all

Table 1. Synopsis of scan time duration and temporal resolution used for the single cardiac phase and CINE T_2^* mapping protocols.

	ME	MS	MB CINE	ME CINE	MS CINE
scan duration phantom study	25s	49s	3×81s	121s	241s
scan duration *in vivo* study	-	24s	3×22s	-	-
acquisition window length	205ms	192ms	36ms	38ms	36ms

The scan duration of **MS** protocols is doubled versus **ME** protocols. For *in vivo* T_2^* mapping **MS** and **MB CINE** were applied. CINE protocols provided an acquisition window length of about 36 ms, which renders the impact of cardiac motion effects rather low. The acquisition window length is given by the number of k-spaces lines acquired per cardiac cycle times the repetition time.
doi:10.1371/journal.pone.0052324.t001

subjects. For this purpose, a mid-ventricular short axis view and a four chamber view were used. Imaging parameters were set to: acquisition data matrix = 256×224, FOV = (288×252) mm^2, in-plane resolution = (1.1×1.1) mm^2, slice thickness = 4 mm if not otherwise stated. A nominal flip angle of $\alpha = 20^\circ$ has been applied; and electro magnetic field (EMF) simulations using the human voxel model "Duke" were conducted for transmission field shaping to enhance B_1^+ uniformity across the heart [36,37,41]. Echo times ranging from 2.04 ms to 10.20 ms were applied. Three excitations together with 3 echoes per excitation were used to ensure an inter-echo time of 1.02 ms. With the first excitation, echo 1, 4 and 7, were acquired. The second excitation covered echo 2, 5 and 8. Echo 3, 6, and 9 were recorded after the third excitation. Moderate acceleration (R = 2 for **MS** and R = 3 for **MB CINE**) in conjunction with GRAPPA reconstruction [42] was applied to reduce the breath-hold time. For single cardiac phase acquisitions, the **MS** protocol was prospectively triggered to place data acquisition at end-diastole or end-systole. For prospectively triggered CINE T_2^* mapping, 25 cardiac phases were acquired for a heart rate of 60 bpm. Phase images of the first two echoes (TE_1 = 2.04 ms, TE_2 = 3.06 ms) of **MS** were used to determine B_0 field maps offline.

Prior to T_2^* mapping, volume selective B_0 shimming was conducted to reduce static magnetic field inhomogeneities [43,44]. In doing so, the susceptibility weighting will be dictated by microscopic B_0 susceptibility gradients, rather than by macroscopic B_0 field inhomogeneities. For this purpose, a 2D multi-slice, cardiac gated, breath-hold double echo (**DE**) gradient echo sequence (TE_1 = 3.06 ms, TE_2 = 5.10 ms) was used for B_0 field mapping. Cardiac gating and breath-holding were applied to reduce and possibly eliminate phase contributions induced by cardiac and respiratory motion. The shim volume was adjusted to cover the left and right ventricle in the four chamber view and in the short axis view of the heart. Data acquisition for B_0 shimming was adjusted to diastole. This choice is based on previous reports which demonstrated that field maps showed a negligible temporal variation across the cardiac cycle [43]. For the shim volumes, linear and second order room temperature shims were calculated to reduce the frequency shift across the phantom or across the

Table 2. Survey of T_2^* derived from phantom studies for single cardiac phase and for CINE T_2^* mapping techniques.

	Mapping technique				
Slice thickness	**ME mean±std**	**MS mean±std**	**MB CINE mean±std**	**ME CINE mean±std**	**MS CINE mean±std**
			(temporal std)	**(temporal std)**	**(temporal std)**
[mm]	**[ms]**	**[ms]**	**[ms]**	**[ms]**	**[ms]**
8	26.1±3.7	26.7±3.0	28.3±2.8	26.9±3.2	27.2±2.6
			(0.4)	(0.4)	(0.3)
	18.3±0.8	18.6±0.8	19.5±0.9	18.6±0.7	19.3±0.7
			(0.3)	(0.1)	(0.3)
6	27.5±2.5	27.2±1.8	28.5±1.9	27.9±2.3	27.6±1.7
			(0.4)	(0.5)	(0.4)
	19.0±0.6	19.2±0.7	19.7±0.7	19.2±0.6	19.5±0.9
			(0.4)	(0.2)	(0.4)
4	28.6±1.6	27.7±1.3	30.2±1.5	29.0±1.5	28.7±1.2
			(0.5)	(0.5)	(0.5)
	19.4±0.7	19.3±0.6	19.8±1.0	19.5±0.8	19.7±1.3
			(0.7)	(0.4)	(0.7)
2.5	30.0±1.3	28.7±1.1	30.7±1.3	30.2±1.3	29.8±1.3
			(0.7)	(0.6)	(0.8)
	19.6±0.9	19.5±2.2	20.1±1.7	19.9±1.3	20.1±2.1
			(1.2)	(0.6)	(1.2)

Mean T_2^* and standard deviation of T_2^* derived from **ME, MS, ME CINE, MS CINE** and **MB CINE** acquisitions using a slice thickness ranging from 8 mm to 2.5 mm. For all slice thicknesses the top rows show T_2^* for the long T_2^* phantom while the bottom rows show T_2^* for the medium T_2^* phantom. For the long T_2^* phantom T_2^* was observed for a ROI (diameter 2 cm) placed in the iso-center of an axial slice of the phantom. For the mediumT_2^* phantom T_2^* was observed for a ROI (diameter 6 cm). Please note, for CINE protocols temporal T_2^* variation is given in parentheses as standard deviation of mean T_2^* over the CINE cycle.
doi:10.1371/journal.pone.0052324.t002

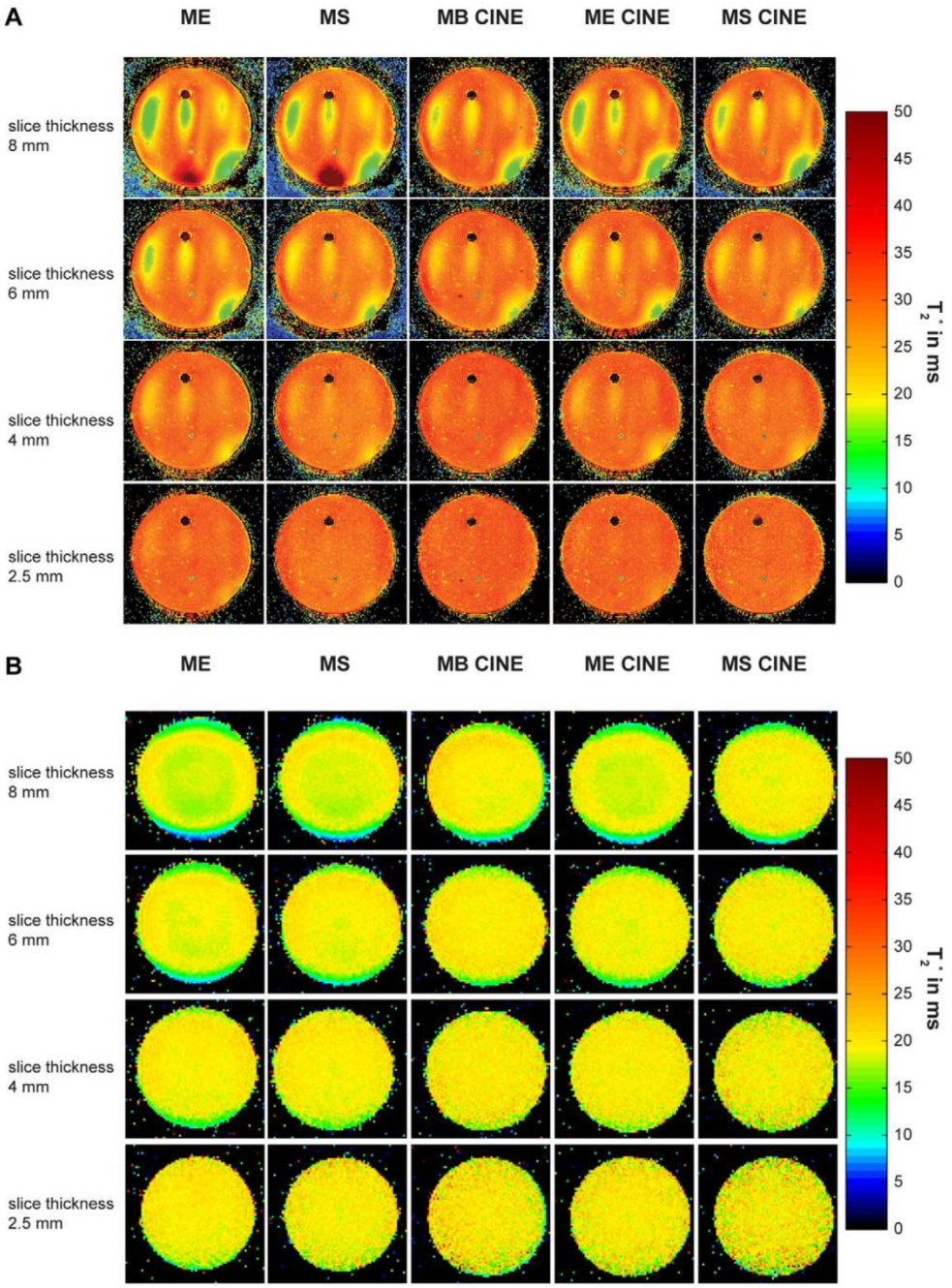

Figure 2. Survey of T_2^* maps derived from phantom studies. T_2^* maps obtained for all imaging strategies using a long T_2^* (**A**) and a medium T_2^* phantom (**B**). Slice thicknesses ranging from 8 mm to 2.5 mm (top to bottom) were applied. T_2^* analysis revealed similar results for all T_2^* mapping strategies. For a slice thickness of 8 mm T_2^* varied substantially across both phantoms. The uniformity in T_2^* was improved for a slice thickness of 6 mm and even further enhanced for a slice thickness of 4 mm or 2.5 mm.
doi:10.1371/journal.pone.0052324.g002

heart with the goal to render B_0 uniform. The overall protocol time, including localizer, slice angulation, volume selective B_0 mapping routine, 2D FLASH CINE imaging (4 chamber view and short axis view) and T_2^* mapping using MS and MB CINE was approximately 30 minutes. Table 1 outlines the breath hold times used for MS and MB CINE T_2^* mapping in healthy volunteers.

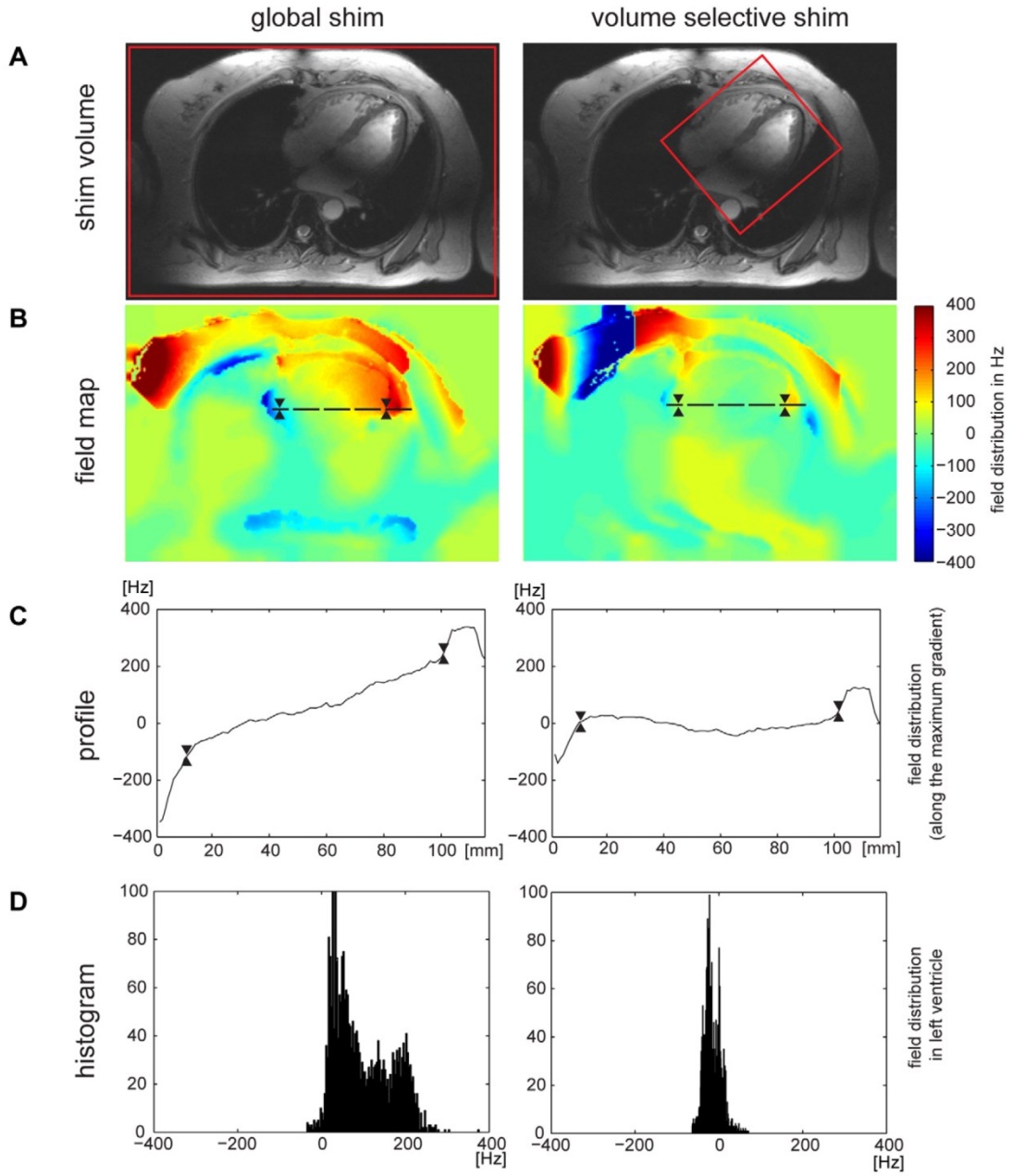

Figure 3. B_0 distribution for global and volume selective B_0 shimming of a four chamber view of the heart. A) Four chamber view of the heart illustrating the positioning of the volume (marked in red) used for global (left) and volume selective (right) shimming. **B**) B_0 field variation derived from global and volume selective shimming. For this subject the global shim provided a peak-to-peak field variation of about 400 Hz across the entire heart. After volume selective shimming peak-to-peak B_0 variation across the heart was reduced to approximately 80 Hz. The direction of the maximal B_0 gradient is illustrated by the dashed black line in **B**) and the corresponding profile of B_0 field distribution is plotted in **C**). To guide the eye the epicardial borders are marked in **B**) and **C**) by two triangles. The histogram of the field distribution over the left ventricle is shown in **D**). The full width at half maximum is approximately 200 Hz for the globally shimmed B_0 field map and was reduced to about 80 Hz after volume selective shimming.
doi:10.1371/journal.pone.0052324.g003

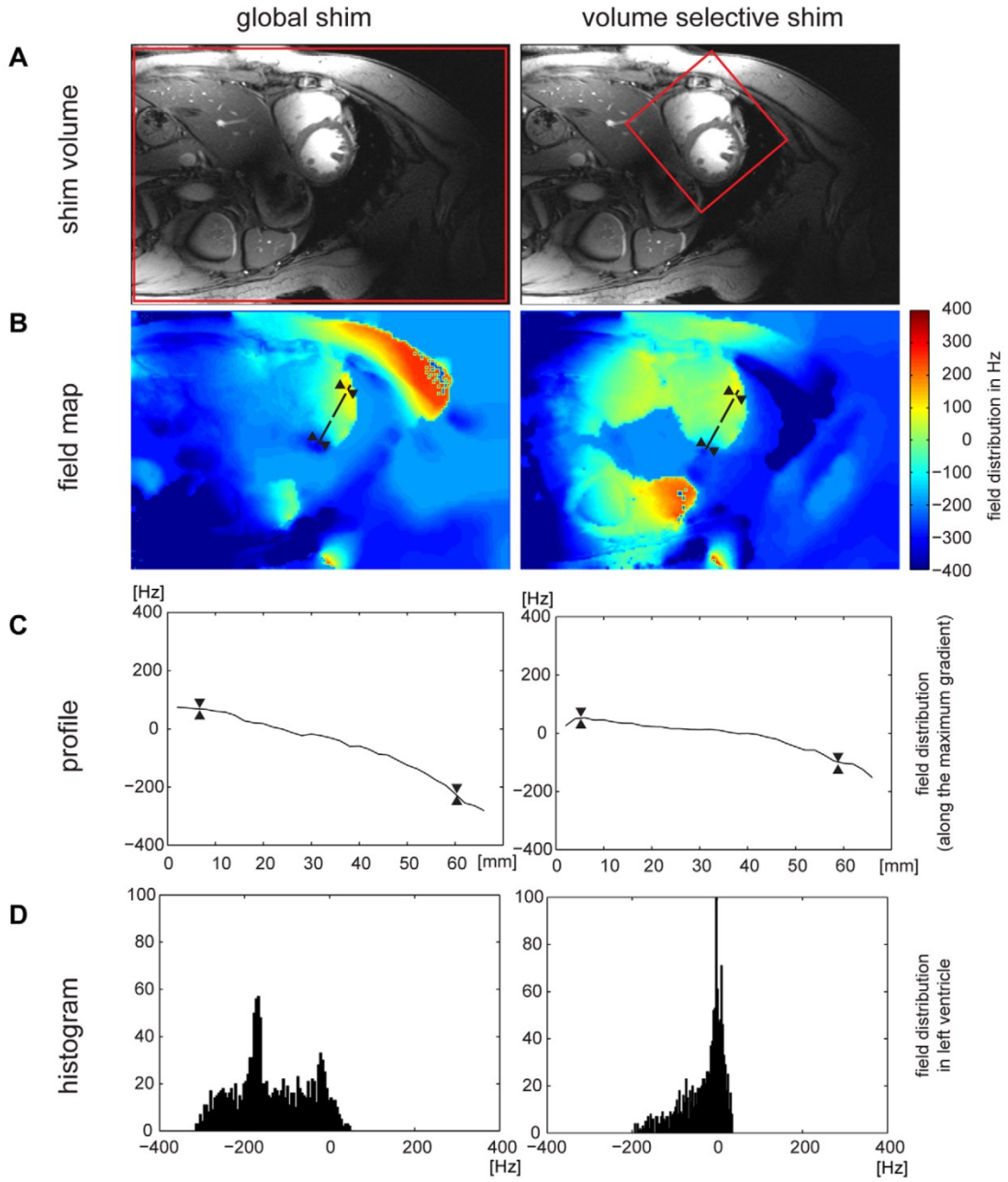

Figure 4. B_0 distribution for global and volume selective shimming of a mid-ventricular short axis view of the heart. A) Mid-ventricular short axis view of the heart illustrating the positioning of the volume (marked in red) used for volume selective shimming. **B**) B_0 field maps. **C**) B_0 profile along the direction of the strongest B_0 gradient which is highlighted by the dashed black line in **B**). To guide the eye the epicardial borders are marked in **B**) and **C**) by two triangles. **D**) Frequency histogram across the left ventricle. After volume selective shimming a strong susceptibility gradient at the inferior region of the heart could be reduced. The full width at half maximum is approximately 300 Hz for the globally shimmed field map and was reduced to about 80 Hz after volume selective shimming.
doi:10.1371/journal.pone.0052324.g004

Post-Processing and Image Analysis

Image datasets were transferred to a MATLAB (The Mathworks, Natick, USA) workstation and processed offline. For all datasets, T_2^* was estimated based on a linear equation set obtained from the logarithm of Equation 1, where $S_{(0)}$ was estimated through $S_{(TEmin)}$. The T_2^* and S_0 estimation was used as initialization values to fit the data points to a mono exponential

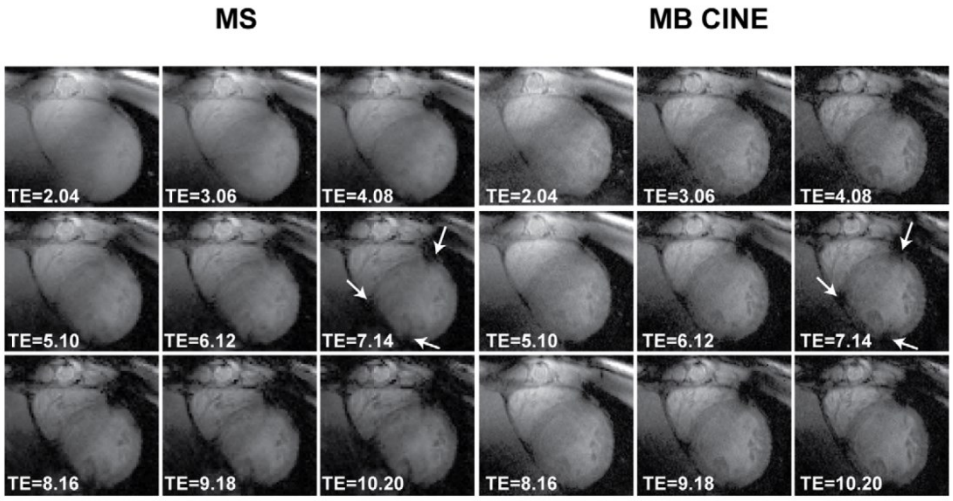

Figure 5. Short axis views derived from single cardiac phase and dynamic CINE T_2^* weighted imaging of the heart. Echo times ranging from 2.04 ms to 10.20 ms were used for **MS** and **MB CINE** acquisitions. A low nominal flip angle of 20° was used to preserve myocardial signal. Image quality observed for **MS** and **MB CINE** acquisitions is comparable**.** No severe susceptibility artifacts were detected in the septum and in the lateral wall for TEs ranging between 2.04 ms to 10.20 ms. For anterior and inferior myocardial areas encompassing major cardiac veins susceptibility weighting related signal void was observed for TE >7 ms as highlighted by white arrows.
doi:10.1371/journal.pone.0052324.g005

decay (Equation 1) based on the MATLAB region trust algorithm.

$$S_{(TE)} = S_0 * e^{\frac{-TE}{T_2^*}} \quad (1)$$

For T_2^* assessment of the phantom data, a ROI covering the entire central axial view of the phantom was used. Average and standard deviation of T_2^* were determined.

For examination of the *in vivo* data, an affine registration of the **MB CINE** datasets was incorporated into the post-processing procedure to compensate for misalignments due to the use of multiple breath-hold periods. The affine registration is landmark based. It shifts and shears the datasets derived from multiple breath-held acquisitions. Landmarks were set manually. Mid-ventricular short axis T_2^* maps were segmented according to the standardized myocardial segmentation and nomenclature for tomographic imaging of the heart [45]. For each segment of the

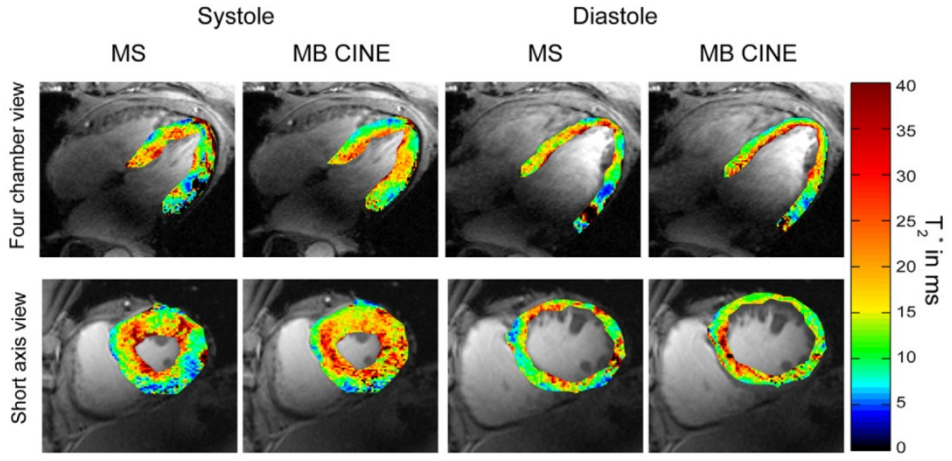

Figure 6. T_2^* maps derived from single cardiac phase and dynamic CINE mapping of a four chamber and short axis view of the heart at end-diastole and end-systole. Four chamber (top) and short axis view T_2^* colour maps obtained from **MS** and **MB CINE** superimposed to anatomical 2D CINE FLASH gray scale images. For **MB CINE** a systolic and diastolic phase was chosen to match the cardiac phase with the end-systolic and end-diastolic phase derived from **MS**. T_2^* maps deduced from **MS** and **MB CINE** showed no significant differences between both methods in the segmental analysis of T_2^* values. When comparing systolic and diastolic T_2^* maps significant differences were found with $p = 0.002$ for MS and $p = 0.01$ for **MB CINE**.
doi:10.1371/journal.pone.0052324.g006

Table 3. Summary of mean and standard deviation of T_2^* (in ms) at end-diastole and at end-systole.

	cardiac segment					
	7	**8**	**9**	**10**	**11**	**12**
MB CINE end-systole	13.7±2.9	17.4±2.5	14.8±1.8	10.5±4.2	8.3±2.4	10.9±1.7
MB CINE end-diastole	16.8±2.2	17.3±1.4	16.3±2.2	12.0±3.6	11.4±2.8	12.5±1.9
MS end-systole	12.4±2.1	17.2±2.7	15.7±2.9	7.6±2.1	10.2±2.0	13.6±1.9
MS end-diastole	14.0±1.8	17.2±2.6	16.5±2.0	10.6±4.4	11.4±2.5	15.7±2.0

Mean T_2^* (in ms) averaged over all subjects for each cardiac segment of a mid-ventricular short axis derived from single cardiac phase **MS** and from **MB CINE** acquisitions at end-diastole and at end-systole. T_2^* values obtained for both approaches show a fair agreement. The statistical analysis showed no significant difference between T_2^* derived from **MS** and T_2^* deduced from **MB CINE** acquisitions.
doi:10.1371/journal.pone.0052324.t003

mid-ventricular slice (segment 7–12 according to [45]), T_2^* values were calculated during end-diastole and end-systole for the single cardiac phase approach. For assessment of temporal changes in T_2^* throughout the cardiac cycle ROIs encompassing segment 7 to 12 were defined and analysed for all cardiac phases derived from MB CINE. For this purpose, the position and shape of the ROI was carefully adjusted throughout the cardiac cycle to account for myocardial contraction and relaxation. Also, this approach was used to include only compact myocardium into the analysis so that blood or trabecular tissue contributions can be eliminated. For careful delineation of the myocardial borders 2D CINE FLASH (flip angle = 32°, acquisition data matrix = 256×224, FOV = (288×252) mm^2, in-plane resolution = (1.1×1.1) mm^2, slice thickness = 4 mm, TE = 2.8 ms, TR = 4.2 ms) was used. Mean values and standard deviation of T_2^* were calculated for all ROIs. Statistical analysis was performed to test for data distribution and group differences using R project for statistical computing (OpenSource: www.r-project.org). A p-value below 0.05 was considered as statistically significant.

Results

Phantom Studies

T_2^* maps derived with all imaging strategies for the phantom experiments are surveyed in Figure 2 and Table 2 and show that all imaging strategies provide similar T_2^* maps. For the long T_2^* phantom, T_2^* varied from 13.6 ms to 37.4 ms across the entire central axial slice when using a slice thickness of 8 mm. The non-uniformity in T_2^* was reduced for 6 mm slices with T_2^* ranging

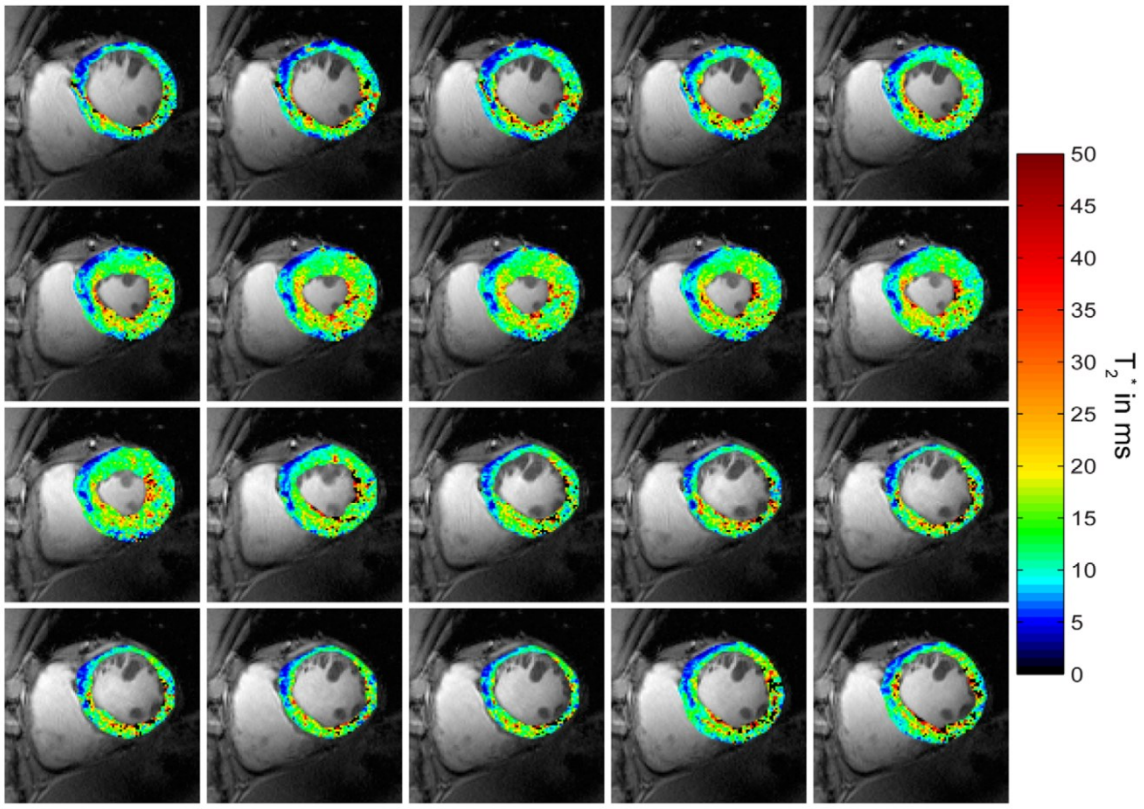

Figure 7. CINE T_2^* maps over the cardiac cycle. Short axis view T_2^* colour maps derived from **MB CINE** acquisitions across the cardiac cycle overlaid to conventional 2D CINE FLASH images. T_2^* values are increasing from diastole to systole, especially for endocardial layers. Macroscopic susceptibility induced T_2^* reduction effects were present at the epicardium at inferior regions.
doi:10.1371/journal.pone.0052324.g007

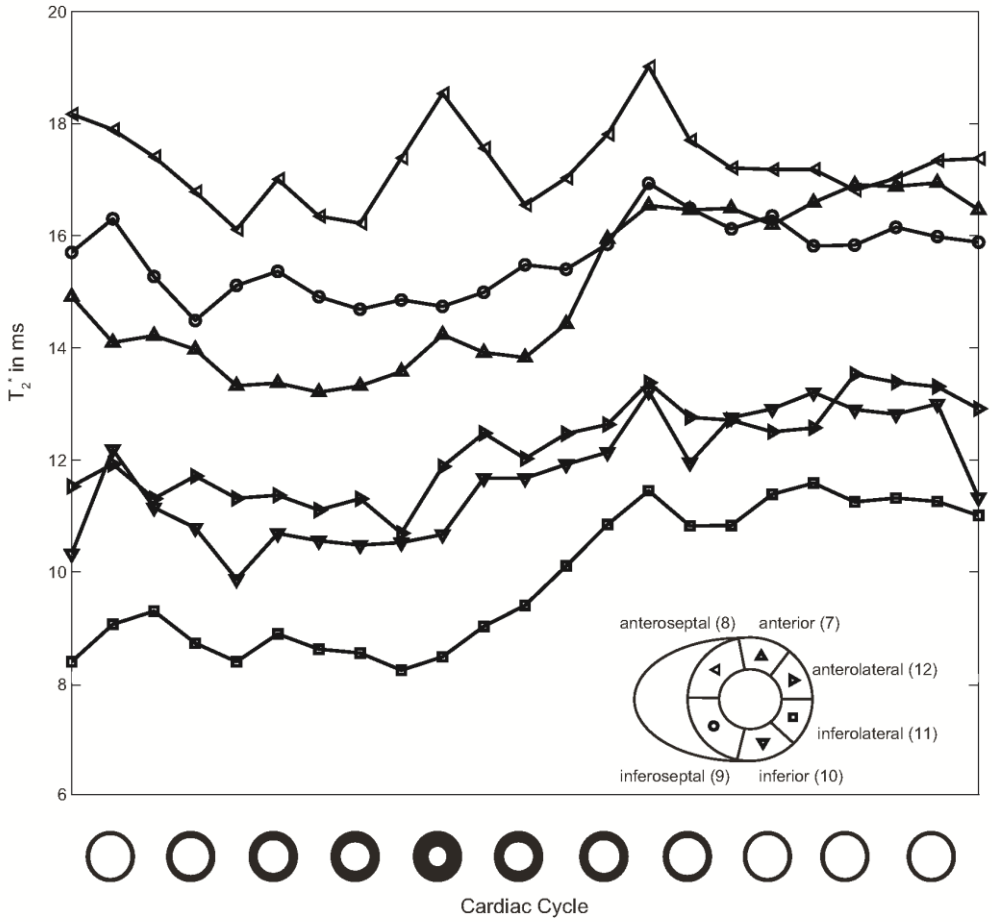

Figure 8. Analysis of T_2^* across the cardiac cycle. Synopsis of the evolution of mean T_2^* averaged over all subjects for standard mid-ventricular segments of the heart. T_2^* derived from each cardiac segment are plotted versus the cardiac cycle. T_2^* changes over the cardiac cycle. Averaging T_2^* over all mid-ventricular myocardial segments revealed that T_2^* increases approximately 27% between systole and diastole. Myocardial T_2^* was derived from **MB CINE** acquisitions. Prospective triggering was used which resulted in a gap at end-diastole of approximately 100 ms depending on the heart rate. For this reason the cardiac cycle is normalized for all subjects without including this gap.
doi:10.1371/journal.pone.0052324.g008

from 19.7 ms to 33.9 ms across the entire central axial slice. T_2^* non-uniformity across the central axial slice was further reduced upon further reducing the slice thickness to 4 mm and 2.5 mm, which showed T_2^* of (29.1±1.5) ms and (29.9±1.7) ms, respectively. T_2^* values derived from a ROI (d = 2 cm) placed in the iso-center of the central axial slice of the phantom varied between 26.1 ms (**ME**) and 28.3 ms (**MB CINE**) for a slice thickness of 8 mm. In comparison, T_2^* values ranging from 28.7 ms (**MS**) to 30.7 (**MB CINE**) were observed for the same small ROI when using a slice thickness of 2.5 mm. T_2^* values derived from CINE imaging remained constant (std <1 ms) throughout the cycle given by the gating paradigm.

For the medium T_2^* phantom, mean T_2^* varied between 18.3 ms and 19.3 ms for a ROI covering the entire central axial slice (slice thickness = 8 mm). For a slice thickness of 6 mm, mean T_2^* values were ranging from 19.0 ms to 19.9 ms. T_2^* mapping using a slice thickness of 4 mm yielded mean T_2^* values ranging from 19.3 ms to 19.8 ms. For a 2.5 mm slice thickness the range of mean T_2^* values encompassed 19.5 ms to 20.1 ms. For this slice thickness the standard deviation of T_2^* across the central slice of the phantom was approximately 2 ms for **MS, MB and MS CINE** due to SNR constraints. T_2^* values derived from CINE imaging remained constant (std <1 ms) throughout the cycle given by the cardiac gating paradigm.

In all phantom experiments, the acquisition time of the **MS** approach was doubled versus the **ME** approach, as summarized in Table 1. In **MS,** only 5 views per segment were recorded while **ME** used 10 views per segment. This approach has been deliberately chosen already at this stage to ensure that the acquisition windows do not exceed the cardiac rest period in the *in vivo* studies. For **ME CINE,** only two views per segment were used to accomplish an acquisition window of 38 ms which increased the total scan duration to 121 s in the phantom studies. This scan duration was doubled for **MS CINE** since only one view per segment could be used for this approach.

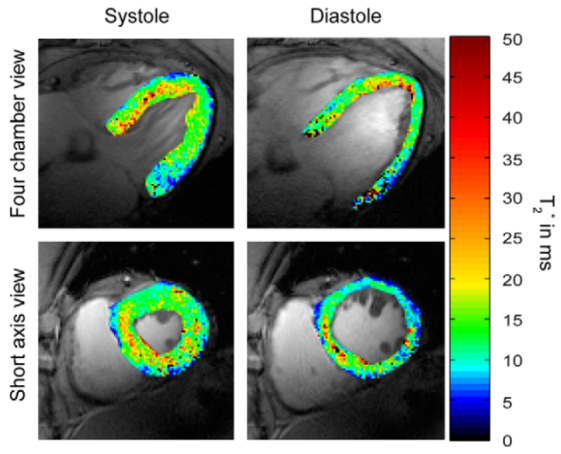

Figure 9. High spatial resolution four chamber and short axis view T_2^* maps derived from T2* weighted CINE imaging. For **MB CINE** slice thickness was reduced to 2.5 mm while maintaining the in-plane spatial resolution of (1.1×1.1) mm^2. Compared to the results obtained with **MB CINE** using a slice thickness of 4 mm, changes in T_2^* from epicardial to endocardial septal myocardial layers are more pronounced, in particular during systole.
doi:10.1371/journal.pone.0052324.g009

Volunteer Studies

For the *in vivo* studies, **MS** and **MB CINE** were applied using a slice thickness of 4 mm to balance the competing constraints between SNR and B_0 background gradients. A reduction in slice thickness helps to reduce intra-voxel dephasing due to B_0 gradients along the slice direction. This slice thickness is afforded by the SNR advantage inherent to 7.0 T and is smaller than that commonly used for T_2^* mapping at 1.5 T and 3.0 T. Localized shimming was performed to reduce static magnetic field inhomogeneities to make sure that the susceptibility weighting is not dominated by macroscopic B_0 field inhomogeneities but rather by microscopic B_0 susceptibility gradients. Figure 3 and Figure 4 depict B_0 maps together with B_0 profiles across the heart and frequency histograms of the heart obtained prior to and after volume selective shimming for a four chamber (Figure 3) and short axis view (Figure 4). The B_0 field maps following global shimming showed a mean peak-to-peak field difference of approximately 400 Hz across the heart for a four chamber view (Figure 3B) and approximately 300 Hz for a mid-ventricular short axis view (Figure 4B). After volume selective shimming, a mean peak-to-peak B_0 difference of approximately 80 Hz was found across the entire heart for a four chamber view (Figure 3B) and a mid-ventricular short axis view (Figure 4B) of the heart. For the left ventricle a B_0 peak-to-peak difference of approximately 65 Hz was observed after volume selective shimming. For both short axis view and 4 chamber view, a maximum in-plane field gradient of approximately 20 Hz/mm (through-plane approximately 80 Hz/voxel for a 4 mm slice thickness) was observed at the epicardial fat/lung interface of the inferior and inferolateral segment as indicated by the B_0 maps and frequency profiles shown in Figure 3B,C and Figure 4B,C. This local B_0 gradient translates into a phase loss of approximately 80% at the maximum echo time of TE = 10 ms. However, the through-plane field gradient at the epicardium/lung interface is much more pronounced versus the through-plane field gradient obtained for the left and right ventricle, as demonstrated in Figure 3B/C. For myocardial anterior, anterolateral and inferoseptal segments a mean in-plane B_0 gradient of approximately 3 Hz/mm was obtained which translates into an through-plane B_0 dispersion of approximately 12 Hz/voxel for a 4 mm slice thickness. This B_0 gradient implies that macroscopic intravoxel dephasing effects are of minor effect for the TE range used. Inspite of B_1^+ shaping using EMF simulations the signal intensity change across the myocardium of a mid-ventricular short axis slice was found to be approximately 40%.

We next employed **MS** and **MB CINE** to determine the limits of susceptibility artifacts. Figure 5 shows end-diastolic short axis views derived from **MS** and **MB CINE** acquisitions using echo times ranging from 2.04 ms to 10.20 ms. With the flip angle of 20°, RF power deposition was well in the SAR limits given by the IEC guidelines [46], which were confirmed by rigorous electromagnetic field simulations [36,37]. The low flip angle was deliberately chosen to preserve myocardial signal by reducing T_1-saturation effects. Although this approach results in a low contrast between the blood pool and the surrounding myocardium (Figure 5), it is beneficial for myocardial T_2^* quantification. Unlike previous reports at 1.5 T and 3.0 T double inversion recovery prepared blood suppression was not used since this approach does not meet the requirements of CINE T_2^*mapping. It should be noted that no differences in mean T_2^* values were found for black blood versus white blood acquisitions at 1.5 T [47]. No severe susceptibility artifacts were detected in the septum (segment 8–9) and in the lateral wall (segment 11–12) for TEs ranging between 2.04 ms to 10.20 ms. For anterior (segment 7) and inferior (segment 10) myocardial areas, which encompass major cardiac veins, a signal void related to the susceptibility weighting was observed for TE >7 ms (Figure 5).

We next explored myocardial T_2^* using single cardiac phase (**MS**) and dynamic CINE (**MB CINE**) acquisitions. Figure 6 shows end-systolic and end-diastolic short axis and four chamber view T_2* maps. Regions of T_2^* reduction were observed in areas adjacent to the large cardiac vein and the posterior vein. A paired t-test showed no significant differences in T_2* values observed for **MS** and **MB CINE** strategies. ($p = 0.8$ for diastole, $p = 0.7$ for systole). The differences between the **MS** the **MB CINE** imaging strategy including all mid-ventricular segments were found to be $T_2^*_{diff} = (0.2 \pm 3.7)$ ms at end-diastole and $T_2^*_{diff} = (-0.2 \pm 3.4)$ ms at end-systole. **MS** and **MB CINE** showed a mean T_2^* of approximately 14 ms for mid-ventricular myocardium. Regional T_2^* variation was observed for mid-ventricular myocardium. The longest T_2^* values were found for segment 8 (**MS:** $T_2^* = 17.2$ ms, **MB CINE:** $T_2^* = 17.3$ ms), segment 9 (**MS:** $T_2^* = 16.5$, **MB CINE:** $T_2^* = 16.3$) and segment 7 (**MS:** $T_2^* = 14.0$ ms, **MB CINE:** $T_2^* = 16.8$ ms). For segment 10 and segment 11 lower T_2^* values were observed (segment 10: **MS:** $T_2^* = 10.6$ ms, **MB CINE:** $T_2^* = 12.0$ ms, segment 11: **MS:** $T_2^* = 11.4$ ms, **MB CINE:** $T_2^* = 11.4$ ms). A synopsis of T_2^* values averaged over all subjects for **MS** and **MB CINE** acquisitions at end-diastole is given in Table 3.

A closer examination revealed a significant difference between myocardial T_2^* obtained at end-diastole and those derived from end-systolic acquisitions. Indeed, an increase in T_2^* can be clearly observed, particularly at the septum, during systolic phases (Figure 6, Figure 7). Figure 7 shows exemplary CINE T_2^* maps for all phases of the cardiac cycle and illustrates the changes of T_2^* over the cardiac cycle. A paired t-test comparing end-diastolic and end-systolic phase T_2^* values for all segments revealed $p = 0.002$ for single cardiac phase **MS** acquisitions and $p = 0.01$ for **MB CINE** acquisitions. When averaging the T_2^* time course from all subjects an increase in T_2^* of 27%±6% in all cardiac segments

could be observed over the cardiac cycle (Figure 8). The shortest T_2^* values were noted for a cardiac phase placed in systole. For all cardiac segments, the longest T_2^* values were found after the onset of diastole. The largest T_2^* increase over the cardiac cycle was found for segment 7 (ΔT_2^* =+3.7 ms) and segment 10 (ΔT_2^* =+3.4 ms).

To demonstrate the baseline SNR advantage of 7.0 T and to further reduce intravoxel dephasing along the slice direction, the slice thickness was reduced to 2.5 mm while maintaining the in-plane spatial resolution of (1.1×1.1) mm^2 in the **MB** CINE protocol. Figure 9 shows short axis and four chamber view T_2^* maps, which demonstrate the high spatial resolution. This approach further manifests the observed changes in T_2^* during systole and diastole and also indicates the high sensitivity of susceptibility mapping by visualizing differences in T_2^* between endocardial and epicardial layers of the myocardium.

Discussion

This work shows the feasibility of high spatially and temporally resolved myocardial T_2^* mapping at 7.0 T. For this purpose T_2^* weighted, gradient echo based imaging techniques using single cardiac phase (**MS**) and CINE (**MB CINE**) acquisition regimes were benchmarked against T_2^* mapping techniques commonly used in current clinical practice at 1.5 T and 3.0 T. These two imaging techniques were first examined in detail in phantom experiments.

It might be considered as a remaining limitation that our results might be affected by residual macroscopic B_0 gradients. However, our B_0 mapping results suggest that a reasonable B_0 uniformity across the heart and the left ventricle can be achieved at 7.0 T which is embodied by a mean through-plane gradient of 3 Hz/mm across the left ventricle. In this regard it should be also noted that our measurements of the B_0 field distribution after volume selective shimming of our uniform phantom provided a through slice peak-to-peak B_0 variation of 80 Hz along a distance of 4 cm which translates into 2 Hz/mm. This B_0 field gradient is similar to what has been observed for the left and right ventricle which showed a mean of 3 Hz/mm.

The frequency shift across the heart reported here compares well with previous 3.0 T studies which reported a peak-to-peak off-resonance variation of (262±58) Hz over the left ventricle and the right ventricle (basal short axis view) for a global shim [48]. This B_0 inhomogeneity was improved to (176±30) Hz and (121±31) Hz with the use of localized linear and second-order shimming [48]. The use of an enhanced locally optimized shim algorithm, which is tailored to the geometry of the heart, afforded a reduction of the peak-to-peak frequency variation over the heart from 235 Hz to 86 Hz at 3.0 T [49]. Another pioneering study showed a peak-to-peak off-resonance of (71±14) Hz for short axis views acquired at 1.5 T [40] using global shimming.

Previous reports on brain imaging/spectroscopy suggest that third-order and even higher order shims help to further enhance B_0 uniformity across the target anatomy [50,51]. For this purpose extra shim drum inserts are retrofitted to the scanner. Notwithstanding its utility the current implementation limits the available space inside of the MR scanner bore which would be prohibitive for cardiac or body MRI at 7.0 T. Other attempts to integrate third order shim coils into high performance 7.0 T whole body gradient coil designs were found to show pronounced gradient non-linearity for spherical volumes with a diameter larger than (20–25) cm; a behavior which does not meet the requirements of cardiac or body MR. Obviously, another approach to further reduce the residual impact of through-plane gradients and intra-voxel dephasing B_0 gradients is the use of even thinner slices and the reduction in voxel size. To meet this goal we pushed the envelope by using a slice thickness as thin as 2.5 mm together with an in-plane resolution of (1.1×1.1) mm^2. This slice thickness and in-plane resolution is afforded by the SNR advantage inherent to 7.0 T. The corresponding voxel size is by a factor of five smaller than commonly used for T_2^* mapping at 1.5 T and 3.0 T. However, it should be noted that the move to even thinner slices and smaller voxel sizes – ideally one might opt to use an infinitesimal small voxel – would disturb the balance dictated by the competing constraints of SNR and background gradients effects.

This study sheds further light to the current literature since it demonstrates the applicability of **MS** and **MB CINE** for T_2^* mapping of normal myocardium at 7.0 T. While we recognize a limitation due to the limited number of healthy subjects studied, we believe this feasibility study to be an essential precursor to a larger 7.0 T study involving healthy and patient cohorts. Such a study would aid to establish the lower limits for normal myocardial T_2^* values versus the clinically established normal values for T_2^* of healthy myocardium at 1.5 T and 3.0 T. To this end, T_2^* mapping at 7.0 T may be useful to extend the capabilities and the dynamic range of the sensitivity of the established approach used for quantification of myocardial iron content. With this in mind, we anticipate to extend our efforts towards clinical studies at 7.0 T including thalassemia major patients, whose T_2^* relaxation times will be benchmarked against the normal values of healthy subjects.

Our results show that T_2^* obtained for human myocardial muscle tissue at 7.0 T ranges from 9 ms to 18 ms. This is in line with T_2^* =(15.8±0.2) ms recently observed for hind limb skeletal muscle in rats at 7 Tesla [52]. Admittedly, the absolute spatial resolution demonstrated for T_2^* mapping of the human heart at 7.0 T is still by an order of magnitude below that previously reported for *ex vivo* MR microscopy based T_2^*mapping of the isolated rat heart [7], which demonstrated that T_2^*mapping provides an insight into the complex architecture of the heart musculature. However, the effective anatomical spatial resolution – voxel size per anatomy – is getting close to what has been demonstrated for animal models. This improvement might be beneficial to gain a better insight into the myocardial microstructure *in vivo* with the ultimate goal to visualize myocardial fibers or to examine helical angulation of myocardial fibers using T_2^* mapping, since the susceptibility effects depend on the tilt angle between blood filled capillaries and the external magnetic field [53]. Myocardial fibre tracking using T_2^* mapping holds the promise to be less sensitive to bulk motion than diffusion-weighted MR of the myocardium [54,55]. Our results also suggest that the increased susceptibility contrast available at 7.0 T could be exploited to quantitatively study iron accumulations in organs other than the heart with high sensitivity and temporal and spatial resolution superior to what can be achieved at 1.5 T and 3.0 T.

For normal myocardium a T_2^* value of approximately 37 ms was found at 1.5 T [23]. At 3.0 T a T_2^* of approximately 27 ms was observed for normal myocardium [56]. These measurements are usually limited to the septum, which shows the lowest spatial variation in T_2^* [57]. It is elusive to study temporal changes in T_2^* at 1.5 and 3.0 T due to scan time constraints which are prohibitive for CINE T_2^* mapping. Of course, single cardiac phase T2* mapping can be applied to diastole and systole as reported previously [58]. This 1.5 T study with thalassemia patients demonstrated mean T_2^* values of (26.4±14.2) ms for early systole and (25.2±13.1) ms for late diastole, which were found to be not significantly different (P=0.27). However, the limited T_2^*

sensitivity together with the temporal resolution used in the study presents a challenge for tracking temporal changes in T_2^*. Please also note, that these data exhibit a rather large standard deviation of approximately ±13.0 ms, which presents another challenge for assessment of temporal T_2^* changes.

A careful literature research revealed that no 1.5 T and 3.0 T T_2^* mapping study has been reported yet which uses a high spatial resolution accomplished here. We would also like to point out that our study is the first study which affords CINE T_2^* mapping due to inter echo time shortening at 7.0 T. To this end it is interesting to note that the myocardial BOLD effect has been investigated using SSFP imaging, which is sensitive to changes in the relaxation times T_2 and T_1. In this regard it has been shown recently that the signal intensity derived from SSFP imaging of the myocardium varies across the cardiac cycle [59]. This study showed a systole-to-diastole T_2 ratio of approximately 1.1 for normal myocardium.

The ability to probe for changes in tissue oxygenation using T_2^* sensitized imaging/mapping offers the potential to address some of the spatial and temporal resolution constraints of conventional first pass perfusion imaging and holds the promise to obviate the need for exogenous contrast agents. Since microscopic susceptibility increases with field strength, thus making the BOLD effect due to (patho)physiology of interest more pronounced, T_2^* mapping at 7.0 T might be beneficial to address some of the BOLD sensitivity constraints reported for the assessment of regional myocardial oxygenation changes in the presence of coronary artery stenosis [60] or for the characterization of vasodilator-induced changes of myocardial oxygenation at 1.5 T and at 3.0 T [17].

Conclusion

Our results underscore the challenges of myocardial T_2^* mapping at 7.0 T due to the propensity to macroscopic susceptibility artefacts and T_2^* shortening, but demonstrate that these issues can be offset by using tailored shimming techniques together with dedicated acquisition schemes.

Acknowledgments

We wish to acknowledge Peter Kellman (Laboratory of Cardiac Energetics, NHLBI, Bethesda, MD, USA) for his valuable support and Antje Els and Julia Skodowski for technical assistance.

Author Contributions

Conceived and designed the experiments: FH CT JSM TN. Performed the experiments: FH CT TN. Analyzed the data: FH JSM. Contributed reagents/materials/analysis tools: FH SW. Wrote the paper: FH CT SW JSM TN.

References

1. Positano V, Pepe A, Santarelli MF, Scattini B, De Marchi D, et al. (2007) Standardized T2* map of normal human heart in vivo to correct T2* segmental artefacts. NMR Biomed 20: 578–590.
2. He T, Gatehouse PD, Kirk P, Mohiaddin RH, Pennell DJ, et al. (2008) Myocardial T(*)2 measurement in iron-overloaded thalassemia: An ex vivo study to investigate optimal methods of quantification. Magn Reson Med 60: 350–356.
3. Heinrichs U, Utting JF, Frauenrath T, Hezel F, Krombach GA, et al. (2009) Myocardial T2* mapping free of distortion using susceptibility-weighted fast spin-echo imaging: a feasibility study at 1.5 T and 3.0 T. Magn Reson Med 62: 822–828.
4. Hernando D, Vigen KK, Shimakawa A, Reeder SB (2011) R 2* mapping in the presence of macroscopic B(0) field variations. Magn Reson Med.
5. Bauer WR, Nadler W, Bock M, Schad LR, Wacker C, et al. (1999) The relationship between the BOLD-induced T(2) and T(2)(*): a theoretical approach for the vasculature of myocardium. Magn Reson Med 42: 1004–1010.
6. Bauer WR, Nadler W, Bock M, Schad LR, Wacker C, et al. (1999) Theory of the BOLD effect in the capillary region: an analytical approach for the determination of T2 in the capillary network of myocardium. Magn Reson Med 41: 51–62.
7. Köhler S, Hiller KH, Waller C, Jakob PM, Bauer WR, et al. (2003) Visualization of myocardial microstructure using high-resolution T*2 imaging at high magnetic field. Magn Reson Med 49: 371–375.
8. Friedrich MG, Niendorf T, Schulz-Menger J, Gross CM, Dietz R (2003) Blood oxygen level-dependent magnetic resonance imaging in patients with stress-induced angina. Circulation 108: 2219–2223.
9. Manka R, Paetsch I, Schnackenburg B, Gebker R, Fleck E, et al. (2010) BOLD cardiovascular magnetic resonance at 3.0 tesla in myocardial ischemia. J Cardiovasc Magn Reson 12: 54.
10. Jahnke C, Gebker R, Manka R, Schnackenburg B, Fleck E, et al. (2010) Navigator-gated 3D blood oxygen level-dependent CMR at 3.0-T for detection of stress-induced myocardial ischemic reactions. JACC Cardiovasc Imaging 3: 375–384.
11. Karamitsos TD, Leccisotti L, Arnold JR, Recio-Mayoral A, Bhamra-Ariza P, et al. (2010) Relationship between regional myocardial oxygenation and perfusion in patients with coronary artery disease: insights from cardiovascular magnetic resonance and positron emission tomography. Circ Cardiovasc Imaging 3: 32–40.
12. Friedrich MG (2010) Testing for myocardial ischemia: the end of surrogates? JACC Cardiovasc Imaging 3: 385–387.
13. Pennell DJ (2010) To BOLDly go where positron emission tomography has been before. Circ Cardiovasc Imaging 3: 2–4.
14. Tsaftaris SA, Tang R, Zhou X, Li D, Dharmakumar R (2012) Ischemic extent as a biomarker for characterizing severity of coronary artery stenosis with blood oxygen-sensitive MRI. J Magn Reson Imaging 35: 1338–1348.
15. Wacker CM, Bock M, Hartlep AW, Beck G, van Kaick G, et al. (1999) Changes in myocardial oxygenation and perfusion under pharmacological stress with dipyridamole: assessment using T*2 and T1 measurements. Magn Reson Med 41: 686–695.
16. Wacker CM, Hartlep AW, Pfleger S, Schad LR, Ertl G, et al. (2003) Susceptibility-sensitive magnetic resonance imaging detects human myocardium supplied by a stenotic coronary artery without a contrast agent. J Am Coll Cardiol 41: 834–840.
17. Vohringer M, Flewitt JA, Green JD, Dharmakumar R, Wang J Jr., et al. (2010) Oxygenation-sensitive CMR for assessing vasodilator-induced changes of myocardial oxygenation. J Cardiovasc Magn Reson 12: 20.
18. Li D, Dhawale P, Rubin PJ, Haacke EM, Gropler RJ (1996) Myocardial signal response to dipyridamole and dobutamine: demonstration of the BOLD effect using a double-echo gradient-echo sequence. Magn Reson Med 36: 16–20.
19. Egred M, Waiter GD, Al-Mohammad A, Semple SI, Redpath TW, et al. (2006) Blood oxygen level dependent (BOLD) MRI: A novel technique for the detection of myocardial ischemia. Eur J Intern Med 17: 551–555.
20. Wacker CM, Bock M, Hartlep AW, Bauer WR, van Kaick G, et al. (1999) BOLD-MRI in ten patients with coronary artery disease: evidence for imaging of capillary recruitment in myocardium supplied by the stenotic artery. MAGMA 8: 48–54.
21. Utz W, Jordan J, Niendorf T, Stoffels M, Luft FC, et al. (2005) Blood oxygen level-dependent MRI of tissue oxygenation: relation to endothelium-dependent and endothelium-independent blood flow changes. Arterioscler Thromb Vasc Biol 25: 1408–1413.
22. Tanner MA, He T, Westwood MA, Firmin DN, Pennell DJ (2006) Multi-center validation of the transferability of the magnetic resonance T2* technique for the quantification of tissue iron. Haematologica 91: 1388–1391.
23. Pepe A, Positano V, Santarelli MF, Sorrentino F, Cracolici E, et al. (2006) Multislice multiecho T2* cardiovascular magnetic resonance for detection of the heterogeneous distribution of myocardial iron overload. J Magn Reson Imaging 23: 662–668.
24. Modell B, Khan M, Darlison M, Westwood MA, Ingram D, et al. (2008) Improved survival of thalassaemia major in the UK and relation to T2* cardiovascular magnetic resonance. J Cardiovasc Magn Reson 10: 42.
25. Ramazzotti A, Pepe A, Positano V, Scattini B, Santarelli MF, et al. (2008) Standardized T2* map of a normal human heart to correct T2* segmental artefacts; myocardial iron overload and fibrosis in thalassemia intermedia versus thalassemia major patients and electrocardiogram changes in thalassemia major patients. Hemoglobin 32: 97–107.
26. Mavrogeni S, Pepe A, Lombardi M (2011) Evaluation of myocardial iron overload using cardiovascular magnetic resonance imaging. Hellenic J Cardiol 52: 385–390.
27. Pennell DJ, Porter JB, Cappellini MD, Chan LL, El-Beshlawy A, et al. (2011) Continued improvement in myocardial T2* over two years of deferasirox therapy in beta-thalassemia major patients with cardiac iron overload. Haematologica 96: 48–54.
28. Carpenter JP, He T, Kirk P, Roughton M, Anderson LJ, et al. (2011) On T2* magnetic resonance and cardiac iron. Circulation 123: 1519–1528.
29. Modell B, Khan M, Darlison M, Westwood MA, Ingram D, et al. (2008) Improved survival of thalassaemia major in the UK and relation to T2* cardiovascular magnetic resonance. J Cardiovasc Magn Reson 10: 42.

30. Kirk P, He T, Anderson LJ, Roughton M, Tanner MA, et al. (2010) International reproducibility of single breathhold T2* MR for cardiac and liver iron assessment among five thalassemia centers. J Magn Reson Imaging 32: 315–319.
31. Meloni A, Positano V, Keilberg P, De Marchi D, Pepe P, et al. (2012) Feasibility, reproducibility, and reliability for the T*(2) iron evaluation at 3 T in comparison with 1.5 T. Magn Reson Med 68: 543–551.
32. Restaino G, Meloni A, Positano V, Missere M, Rossi G, et al. (2011) Regional and global pancreatic T*2 MRI for iron overload assessment in a large cohort of healthy subjects: normal values and correlation with age and gender. Magn Reson Med 65: 764–769.
33. Turner R, Jezzard P, Wen H, Kwong KK, Le Bihan D, et al. (1993) Functional mapping of the human visual cortex at 4 and 1.5 tesla using deoxygenation contrast EPI. Magn Reson Med 29: 277–279.
34. van der Zwaag W, Francis S, Head K, Peters A, Gowland P, et al. (2009) fMRI at 1.5, 3 and 7 T: characterising BOLD signal changes. Neuroimage 47: 1425–1434.
35. Donahue MJ, Hoogduin H, van Zijl PC, Jezzard P, Luijten PR, et al. (2011) Blood oxygenation level-dependent (BOLD) total and extravascular signal changes and DeltaR2* in human visual cortex at 1.5, 3.0 and 7.0 T. NMR Biomed 24: 25–34.
36. Thalhammer C, Renz W, Winter L, Hezel F, Rieger J, et al. (2012) Two-Dimensional sixteen channel transmit/receive coil array for cardiac MRI at 7.0 T: Design, evaluation, and application. J Magn Reson Imaging 36: 847–857.
37. Winter L, Kellman P, Renz W, Grassi A, Hezel F, et al. (2012) Comparison of three multichannel transmit/receive radiofrequency coil configurations for anatomic and functional cardiac MRI at 7.0T: implications for clinical imaging. Eur Radiol 22: 2211–2220.
38. Frauenrath T, Hezel F, Heinrichs U, Kozerke S, Utting JF, et al. (2009) Feasibility of cardiac gating free of interference with electro-magnetic fields at 1.5 Tesla, 3.0 Tesla and 7.0 Tesla using an MR-stethoscope. Investigative Radiology 44: 539–547.
39. Frauenrath T, Hezel F, Renz W, d'Orth Tde G, Dieringer M, et al. (2010) Acoustic cardiac triggering: a practical solution for synchronization and gating of cardiovascular magnetic resonance at 7 Tesla. J Cardiovasc Magn Reson 12: 67.
40. Reeder SB, Faranesh AZ, Boxerman JL, McVeigh ER (1998) In vivo measurement of T_2^* and field inhomogeneity maps in the human heart at 1.5 T. Magn Reson Med 39: 988–998.
41. Christ A, Kainz W, Hahn EG, Honegger K, Zefferer M, et al. (2010) The Virtual Family—development of surface-based anatomical models of two adults and two children for dosimetric simulations. Physics in medicine and biology 55: N23.
42. Griswold MA, Jakob PM, Heidemann RM, Nittka M, Jellus V, et al. (2002) Generalized autocalibrating partially parallel acquisitions (GRAPPA). Magn Reson Med 47: 1202–1210.
43. Shah S, Kellman P, Greiser A, Weale P, Zuehlsdorff S, et al. (2009) Rapid Fieldmap Estimation for Cardiac Shimming. Proc Intl Soc Mag Reson Med 17: 566.
44. Schär M, Kozerke S, Boesiger P (2004) Navigator gating and volume tracking for double-triggered cardiac proton spectroscopy at 3 Tesla. Magn Reson Med 51: 1091–1095.
45. Cerqueira M, Weissman N, Dilsizian V, Jacobs A, Kaul S, et al. (2002) Standardized myocardial segmentation and nomenclature for tomographic imaging of the heart: a statement for healthcare professionals from the Cardiac Imaging Committee of the Council on Clinical Cardiology of the American Heart Association. Circulation 105: 539–542.
46. (2010) International Electrical Commission: Particular requirements for the basic safety and essential performance of magnetic resonance equipment for medical diagnosis. IEC-60601-2-33 Medical electrical equipment Part 2–33.
47. Smith GC, Carpenter JP, He T, Alam MH, Firmin DN, et al. (2011) Value of black blood T2* cardiovascular magnetic resonance. J Cardiovasc Magn Reson 13: 21.
48. Schar M, Kozerke S, Fischer SE, Boesiger P (2004) Cardiac SSFP imaging at 3 Tesla. Magn Reson Med 51: 799–806.
49. Schar M, Vonken EJ, Stuber M (2010) Simultaneous B(0)- and B(1)+-map acquisition for fast localized shim, frequency, and RF power determination in the heart at 3 T. Magn Reson Med 63: 419–426.
50. Pan JW, Lo KM, Hetherington HP (2012) Role of very high order and degree B(0) shimming for spectroscopic imaging of the human brain at 7 tesla. Magn Reson Med 68: 1007–1017.
51. Hetherington HP, Avdievich NI, Kuznetsov AM, Pan JW (2010) RF shimming for spectroscopic localization in the human brain at 7 T. Magn Reson Med 63: 9–19.
52. Ziener CH, Kampf T, Melkus G, Jakob PM, Schlemmer HP, et al. (2012) Signal evolution in the local magnetic field of a capillary – analogy to the damped driven harmonic oscillator. Magn Reson Imaging 30: 540–553.
53. Reichenbach JR, Haacke EM (2001) High-resolution BOLD venographic imaging: a window into brain function. NMR Biomed 14: 453–467.
54. Reese TG, Weisskoff RM, Smith RN, Rosen BR, Dinsmore RE, et al. (1995) Imaging myocardial fiber architecture in vivo with magnetic resonance. Magn Reson Med 34: 786–791.
55. Wu MT, Tseng WY, Su MY, Liu CP, Chiou KR, et al. (2006) Diffusion tensor magnetic resonance imaging mapping the fiber architecture remodeling in human myocardium after infarction: correlation with viability and wall motion. Circulation 114: 1036–1045.
56. O'Regan D, Callaghan M, Fitzpatrick J, Naoumova R, Hajnal J, et al. (2008) Cardiac T2* and lipid measurement at 3.0 T-initial experience. Eur Radiol 18: 800–805.
57. Meloni A, Luciani A, Positano V, De Marchi D, Valeri G, et al. (2011) Single region of interest versus multislice T2* MRI approach for the quantification of hepatic iron overload. J Magn Reson Imaging 33: 348–355.
58. He T, Gatehouse PD, Kirk P, Tanner MA, Smith GC, et al. (2007) Black-blood T2* technique for myocardial iron measurement in thalassemia. J Magn Reson Imaging 25: 1205–1209.
59. Tsaftaris SA, Rundell V, Zhou X, Liu Y, Tang R, et al. Detecting Myocardial Ischemia at Rest with Cardiac Phase-Resolved BOLD MRI: Early Findings. Proc Intl Soc Mag Reson Med; 2011; Montreal, Quebec, Canada. #217.
60. Dharmakumar R, Arumana JM, Tang R, Harris K, Zhang Z, et al. (2008) Assessment of regional myocardial oxygenation changes in the presence of coronary artery stenosis with balanced SSFP imaging at 3.0 T: theory and experimental evaluation in canines. J Magn Reson Imaging 27: 1037–1045.

Myocardial T2* mapping free of distortion using susceptibility-weighted fast spin-echo imaging: a feasibility study at 1.5 T and 3.0 T

Heinrichs U, Utting JF, Frauenrath T, Hezel F, Krombach GA, Hodenius MA, Kozerke S, Niendorf T.

Magn Reson Med. 2009 Sep;62(3):822-8

http://dx.doi.org/10.1002/mrm.22054

Feasibility of cardiac gating free of interference with electro-magnetic fields at 1.5 Tesla, 3.0 Tesla and 7.0 Tesla using an MR-stethoscope

Frauenrath T, Hezel F, Heinrichs U, Kozerke S, Utting JF, Kob M, Butenweg C, Boesiger P, Niendorf T.

Invest Radiol. 2009 Sep;44(9):539-47

http://dx.doi.org/10.1097/RLI.0b013e3181b4c15e

Comparison of left ventricular function assessment using phonocardiogram- and electrocardiogram-triggered 2D SSFP CINE MR imaging at 1.5 T and 3.0 T

Becker M, Frauenrath T, Hezel F, Krombach GA, Kremer U, Koppers B, Butenweg C, Goemmel A, Utting JF, Schulz-Menger J, Niendorf T.

Eur Radiol. 2010 Jun;20(6):1344-55

http://dx.doi.org/10.1007/s00330-009-1676-z

Cardiac chamber quantification using magnetic resonance imaging at 7 Tesla--a pilot study

von Knobelsdorff-Brenkenhoff F, Frauenrath T, Prothmann M, Dieringer MA, Hezel F, Renz W, Kretschel K, Niendorf T, Schulz-Menger J.

Eur Radiol. 2010 Dec;20(12):2844-52

http://dx.doi.org/10.1007/s00330-010-1888-2

Frauenrath et al. Journal of Cardiovascular Magnetic Resonance 2010, 12:67
http://www.jcmr-online.com/content/12/1/67

Journal of Cardiovascular Magnetic Resonance

RESEARCH Open Access

Acoustic cardiac triggering: a practical solution for synchronization and gating of cardiovascular magnetic resonance at 7 Tesla

Tobias Frauenrath[1*], Fabian Hezel[1], Wolfgang Renz[1,2], Thibaut de Geyer d'Orth[1], Matthias Dieringer[1,3,4], Florian von Knobelsdorff-Brenkenhoff[3,4], Marcel Prothmann[3], Jeanette Schulz-Menger[1,3,4], Thoralf Niendorf[1,4]

Abstract

Background: To demonstrate the applicability of acoustic cardiac triggering (ACT) for imaging of the heart at ultrahigh magnetic fields (7.0 T) by comparing phonocardiogram, conventional vector electrocardiogram (ECG) and traditional pulse oximetry (POX) triggered 2D CINE acquisitions together with (i) a qualitative image quality analysis, (ii) an assessment of the left ventricular function parameter and (iii) an examination of trigger reliability and trigger detection variance derived from the signal waveforms.

Results: ECG was susceptible to severe distortions at 7.0 T. POX and ACT provided waveforms free of interferences from electromagnetic fields or from magneto-hydrodynamic effects. Frequent R-wave mis-registration occurred in ECG-triggered acquisitions with a failure rate of up to 30% resulting in cardiac motion induced artifacts. ACT and POX triggering produced images free of cardiac motion artefacts. ECG showed a severe jitter in the R-wave detection. POX also showed a trigger jitter of approximately $\Delta t = 72$ ms which is equivalent to two cardiac phases. ACT showed a jitter of approximately $\Delta t = 5$ ms only. ECG waveforms revealed a standard deviation for the cardiac trigger offset larger than that observed for ACT or POX waveforms.
Image quality assessment showed that ACT substantially improved image quality as compared to ECG (image quality score at end-diastole: ECG = 1.7 ± 0.5, ACT = 2.4 ± 0.5, p = 0.04) while the comparison between ECG vs. POX gated acquisitions showed no significant differences in image quality (image quality score: ECG = 1.7 ± 0.5, POX = 2.0 ± 0.5, p = 0.34).

Conclusions: The applicability of acoustic triggering for cardiac CINE imaging at 7.0 T was demonstrated. ACT's trigger reliability and fidelity are superior to that of ECG and POX. ACT promises to be beneficial for cardiovascular magnetic resonance at ultra-high field strengths including 7.0 T.

Background

The challenge of synchronization of data acquisition with the cardiac cycle constitutes a practical impediment of cardiovascular magnetic resonance (CMR). Cardiac motion has been addressed by synchronization strategies exploiting (i) finger plethysmography [1], (ii) cardiac activity related esophageal wall motion [2], (iii) invasive left ventricular blood pressure gating [3], (iv) Doppler ultrasound [4], (v) motion induced changes in the impedance match of RF-coils [5], (vi) self gating techniques [6-10] and optic acoustic methods [11] including human and animal studies. In current clinical CMR, cardiac motion is commonly dealt with using electrocardiographic (ECG) or finger pulse oximetry (POX) triggering/gating techniques [12-14] to synchronize data acquisition with the cardiac cycle. At higher magnetic field strengths the artifact sensitivity of ECG recordings and even of advanced vector ECG increases [13,15]. ECG, being an inherently electrical measurement with electrically active components [12], does carry a risk of surface heating of patients' skin and even of skin burns resulting from induction of high voltages in ECG hardware [16-19]. As ultrahigh field CMR becomes more widespread, the propensity of ECG recordings to

* Correspondence: Tobias.Frauenrath@mdc-berlin.de
[1]Berlin Ultrahigh Field Facility (B.U.F.F.), Max-Delbrueck Center for Molecular Medicine, Berlin, Germany
Full list of author information is available at the end of the article

interference from electromagnetic fields and to magneto-hydrodynamic effects is further pronounced [20-22].

Realizing the constraints of conventional ECG, a MR-stethoscope which uses the phonocardiogram has been proposed. Its feasibility for the pursuit of/prospectively triggered and retrospectively gated cardiac imaging has been demonstrated for field strengths up to 3.0 T [20,21,23] The applicability and clinical efficacy of acoustic cardiac triggering (ACT) has not been demonstrated for imaging of the heart at ultrahigh magnetic fields yet due to the lack of appropriate RF coils and other practical obstacles of CMR at 7.0 T. Recently, R-wave mis-registration has been consistently reported for ECG triggered CMR at 7.0 T [24-26]. Consequently, in one study approximately 20% of the healthy subjects needed to be excluded from left ventricular function assessment [24,25]. In another study 80% of the acquisitions were gated using pulse oximetry due to ECG-triggering problems [26]. Driven by the limitations and motivated by the challenges of conventional ECG together with the advantages of ACT, this study compares phonocardiogram triggered, conventional vector electrocardiogram triggered and traditional pulse oximetry triggered CMR cine imaging at 7.0 T in a pilot study as precursor to a larger clinical study.

To accomplish this goal, the suitability, accuracy and reproducibility of each cardiac triggering approach for the assessment of left ventricular parameter at 7.0 T is explored. For this purpose, breath-held 2D CINE imaging in conjunction with a retrospective triggering regime is conducted paralleled by real time logging of the ECG, POX and ACT signal waveforms to track (mis)synchronization between the cardiac cycle and data acquisition. A qualitative and quantitative analysis of 2D CINE images and signal waveforms is performed. The merits and limitations of the acoustic cardiac gating approach are discussed and its implications for other ultrahigh field MR imaging applications are considered.

Materials and methods

Acoustic Noise Measurements at 7.0 T

During CMR, recordings of a phonocardiogram inside of the magnet bore are paralleled by acoustic noise due to gradient coil switching consisting of several very sharp harmonic components, which are related to the echo time TE and the repetition time TR. For this reason, acoustic measurements were conducted to assess the acoustic signal-to-noise ratio between the sound pressure level induced by the cardiac activity and the sound-pressure level generated by the gradient noise. Acoustic measurements were conducted inside the 7.0 T magnet bore. Two series of acoustic signals were acquired. The first series was designed to record and characterize the noise generated in the MR environment by a 2D CINE FLASH sequence (TE = 2 ms, TR = 4 ms, pixel bandwidth = 445 Hz, FOV = (32 × 32) cm^2 using an optical microphone (MO 2000 set, Sennheiser, Wedemark, Germany). For this purpose, the optical microphone was positioned at the same position with respect to the scanning table and the magnet bore as it was used in the volunteer study. The second series was setup to collect and analyze the phonocardiogram derived from the heart sound of healthy subjects superimposed by the environmental noise generated by the same 2D CINE FLASH technique. For this purpose, an acoustic sensor (diameter = 5 cm) covered by a membrane to generate a pressure wave in a waveguide was attached to the optical microphone. The acoustic signal was recorded by means of an USB-soundcard chip (PCM2903; Texas Instruments, Dallas, TX, USA). The optical microphone was calibrated with a 94 dB test tone provided from a pistonphone (Voltcraft SLC-100, Conrad electronics, Germany). After connecting the membrane to the microphone the set-up was calibrated manually to correct for the minor attenuation induced by the acoustic sensor's membrane. With this set-up absolute sound pressure levels were obtained. Furthermore, this approach offers the benefit that the characteristics of the acoustic signal measurements are given by the environment and not by the signal processing unit. Due to the use of this linear time invariant network approach frequency-shifts between the acoustic signal obtained from the MR environment and the final power spectrum can be avoided. Also, the sound pressure level can be normalized to the auditory threshold.

Pulse Oximetry, ECG and Acoustic Triggering

For pulse oximetry, a commercial sensor (Siemens, Erlangen, Germany) was placed on the tip of the right index finger to track changes in the absorbance due to the pulsing arterial blood. A wireless connection linked the sensors output to the internal physiological signal controller circuitry of the MR scanner.

For ECG recording and triggering, a commercial vector ECG module (Siemens, Erlangen, Germany) was used. The electrodes (ConMed, Corp., Utica, NY, USA) of the vector ECG were carefully placed at the anterior chest wall, with one electrode on the sternum, one on the left thorax, and one below the sternum following the manufacturer's patient preparation instructions. For the vector ECG's training period the patient table was placed in the home position to eliminate major interferences with the fringe field. The waveform was delivered to the internal physiological signal controller circuitry of the clinical MR scanner.

Unlike traditional ECG-triggering the acoustic approach employs the phonocardiogram's first heart

tone for triggering instead of electrophysiological signals [23]. The acoustic gating device comprises four main components: an acoustic sensor made of synthetic material placed on the subject's anterior chest for phonocardiogram detection, an acoustic wave guide for signal transfer and to ensure galvanic decoupling, a signal processing unit and a coupler unit to the MR system. The two former aspects have also safety implications since the ACT approach galvanically isolates the subject and hence eliminates the risk for patient burns. Signal processing and conversion were conducted outside the magnet room using dedicated electronic circuit [23]. Short rectangular shaped trigger pulses were generated to provide an output trigger signal. This waveform was delivered to the internal physiological signal controller circuitry of the clinical MR scanner. This design was chosen to meet the needs of cardiac gated/triggered CMR: (i) maximum latency of 35 ms between the ECG's R-wave and phonocardiogram based trigger output pulse, (ii) free of interference with electromagnetic fields and (iii) immunity to magneto-hydrodynamic effects. The current implementation connects the trigger signal to the MR-scanner's standard external trigger signal input. Hence, no changes to the MR system's hardware or software are required [23]. The acoustic sensor was positioned directly on the subject's chest at the anterior left fifth intercostals space and gently fixed with a strap incorporated in the MR patient table. Note that neither the limited ECG in the MR scanner nor the acoustic waveforms reported here should be treated as reliable indicators of patient emergency conditions.

Three patient table positions were selected to examine the signal waveform as a function of the magnetic field strength: (i) patient table in home position so that the magnetic field strength at the ECG, POX and ACT sensor position was approximately 0.3 T, (ii) ECG, POX and ACT sensor position aligned with the front end of the magnet with a fringe field of approximately 1.0 T and (iii) ECG, POX and ACT sensor in the magnet's isocenter (B_0 = 7.0 T).

Logging and Analysis of Signal Waveforms at 7.0 T

For all subjects vector ECG, POX and ACT were connected at the same time to record traces of waveforms along with the trigger information simultaneously. This information was extracted from the scanners central physiological monitoring unit (CPMU) and simultaneously stored in log files with a sampling rate of 400 Hz (ECG), 50 Hz (POX) and 200 Hz (ACT). Also, the trigger detection tickmarks generated for Vector ECG, POX or ACT triggering by the scanners CPMU were written into log files. This logging procedure was paralleled by storing the respiratory trace simultaneously using a sampling rate of 50 Hz.

The recorded data were processed to analyze the trigger information and to assess triggering efficiency and temporal fidelity of synchronization with the cardiac cycle for each trigger technique. Off-line analysis of the log-files was performed using LabVIEW (National Instruments, Austin, TX, USA). For this purpose a customized post-processing algorithm was developed. The post-processing procedure includes the following features:

- Identification of breath hold periods: Only portions of the trigger signal traces which were acquired during breath-held 2D CINE FLASH imaging were included into the waveform analysis. For this purpose, the respiratory trace was used.
- Segmentation and temporal realignment: The ECG waveform is segmented into individual R-R intervals by using cross correlation between R-R intervals. For this purpose, one R-R interval acquired at the one breath-held CINE series is taken as a reference while all other R-R intervals are shifted along the time axis to achieve maximum correlation with the reference. This R-R wave segmentation mask is applied to the segmentation of the POX and ACT waveforms, which were acquired simultaneously to the ECG waveform. Temporal realignment was used to overcome the potential bias of (erroneous) trigger detection provided by the scanners internal real-time circuitry.
- Reassignment of the trigger detection tickmarks derived from the scanners central physiological monitoring unit to the realigned ECG, POX and ACT traces and assessment of the trigger jitter across the cardiac cycle.
- Calculation of the mean value and the standard deviation of the cardiac cycle for ECG, POX and ACT as an objective measure for trigger reliability.
- Calculation of the offset between the ECG's R-wave and the trigger detection moment derived from the ECG, POX and ACT waveform as an objective measure for trigger reliability.

Cine CMR at 7.0 T

End-expiratory breath-hold short axis views of the heart ranging from the atrioventricular ring to the apex were acquired using retrospectively gated 2D FLASH CINE on a 7.0 T whole body MR systems (Magnetom, Siemens, Erlangen, Germany). A 4 element transmit/receive coil was used for RF excitation and signal reception [27]. The coil was connected to the 7.0 T system via 4 transmit/receive (T/R) switches and a 1 to 4 radio frequency power splitter and combiner with a CP-like phase setting for the four individual channels. The coil setup consists of two identical coil subsets - one placed on the subject's anterior torso and one positioned posterior - each containing two transmit/receive loop coil elements.

For breath-held 2D CINE FLASH imaging field of view (FOV) was set to (340 × 308) mm^2, data

acquisition matrix size was set to 256 × 186 elements (reconstruction matrix size 256 × 232 elements). 30 cardiac phases (temporal resolution = 33 ms for a heart rate of 60 bpm) were acquired using typically 18 slices (slice thickness = 4 mm, slice gap = 2 mm). Slice order was reversed from apex-base to base-apex throughout the set of subjects to eliminate patient discomfort or training effects. Image acquisition was confined to a single slice per breath-hold. The flip angle was set to α = 35 for all subjects, resulting in TR = 5.5 ms and TE = 2.7 ms. Parallel imaging was applied (R = 2) using sensitivity encoding based reconstruction.

Three sets of breath-held 2D CINE FLASH acquisitions were performed. In one set ACT was employed. For comparison, the other set made use of vector ECG based cardiac triggering while another set used POX for cardiac triggering. The use of ACT, ECG and POX was swapped randomly to avoid systematic errors.

Image Analysis

For LV chamber quantification end-diastolic and end-systolic volume (EDV, ESV), and left ventricular mass (LVM) were calculated using commercial evaluation software (CMR42®, Circle Cardiovascular Imaging, Calgary, Canada) from images of all subjects using all three triggering methods. CMR reading was performed by one cardiologist with very profound expertise in clinical CMR (>3000 CMR examinations), who was not involved in the image acquisition at all.

For CINE image quality assessment two independent observers reviewed and scored the images in a randomized, blinded reading session. For this purpose, overall image quality of end-diastolic and end-systolic images was rated using a scale ranging from 0 to 3 for each slice. The following scale was used for the blinded reading:

0 - images with poor and non-diagnostic quality due to cardiac motion induced blurring,
1 - image quality impaired by cardiac motion which may lead to misdiagnosis,
2 - good image quality, cardiac motion artifacts hard to recognize and
3 - excellent image quality, no cardiac motion artifacts observed.

After the independent image quality assessment was completed both readers exchanged their rankings for each case-, slice- and cardiac phase, and agreed on a consensus score.

Endocardial border sharpness (EBS) of the 2D CINE FLASH images derived from ACT, ECG POX triggered acquisitions was determined through an objective measurement of acutance using a dedicated algorithm [21].

Study Population

The study was designed as a comparative volunteer study using healthy adult subjects with no history of cardiovascular disease (n = 9). The mean age was 32 ± 10 years ranging 23-52 years. The average body surface area was (2.0 ± 0.3) m^2 ranging from 1.8 m^2 to 2.7 m^2. The average body mass index was 24.8 ± 4.4 kg/m^2 (range 20.9-35.9 kg/m^2). Volunteers with contraindications to CMR were excluded. The study was carried out according to the principles of the Declaration of Helsinki and was approved by the local institutional ethics committee. Informed written consent was obtained from each volunteer prior to the study, in compliance with the local institutional review board guidelines.

Statistical Analysis

All data are presented as mean ± standard deviation (SD) unless stated otherwise. Statistical significance in the difference of the image scores was analyzed using Wilcoxon matched pairs test for the consensus scores for ACT vs ECG, ACT vs POX and ECG vs POX triggered data. Statistical significance in the difference of the parameter derived from LV function assessment was analyzed using t-test. A probability $p \leq 0.05$ was considered statistically significant. All computations were performed with Microsoft Excel (Microsoft, Redmond, USA) and R (R Foundation for Statistical Computing, Vienna, Austria). Comparison of the different triggering techniques was carried out using the Bland and Altman method [28] (GraphPad Software, Inc., La Jolla, CA, USA). The confidence interval was set to the mean value ± 1.96 of the standard deviation.

Results

Acoustic Signal-to-Noise Measurements at 7.0 T

Recordings of phonocardiograms inside the magnet bore are paralleled by acoustic noise due to gradient coil switching. High sound pressure levels (SPL) of up to 120 dB were induced by magnetic field gradients driven by the switching scheme of a 2D FLASH CINE imaging technique. Figure 1 illustrates the spectrogram which shows the sound pressure level spectrum over time obtained from a subject positioned at the magnet's isocenter during 2D CINE FLASH imaging (TE = 2.0 ms, TR = 4.0 ms) at 7.0 T. In this case of the phonocardiogram being paralleled by the gradient switching noise the sound pressure level (SPL) was tracked over a series of 6 heartbeats. The power spectra show numerous noise peaks including several very sharp harmonic components at 1/TR, 2/TR, 3/TR and 1/TE which are related to the gradient switching scheme of 2D FLASH with maximum SPL close to 120 dB. The spectrogram also revealed that the heart sound encompasses low-frequencies.

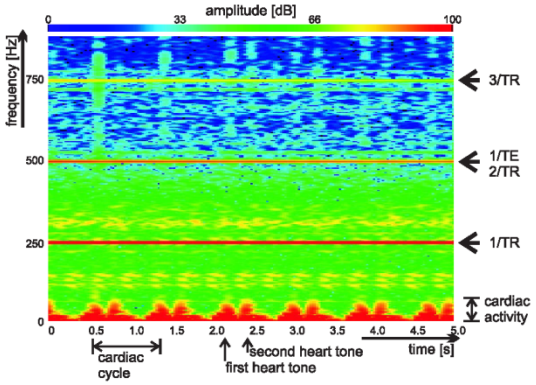

Figure 1 Acoustic Spectrogram obtained at 7.0 T. Spectrogram obtained from a subject positioned at the 7.0 T magnet's isocenter during 2D CINE FLASH acquisitions (TE = 2.0 ms, TR = 4.0 ms). The graphs show signal contributions from gradient switching superimposed on the cardiac signals. The gradient switching manifests itself by several very sharp harmonic components at 1/TR, 2/TR, 3/TR and 1/TE with maximum sound pressure level close to 120 dB. The spectrogram also shows the 1st and the 2nd heart tone which are of low-frequency nature. Acoustic signal-to-noise ratio, which is defined as the ratio between the sound pressure level due to cardiac activity and the gradient switching induced sound pressure level is approximately 30 dB for the frequency range between 10 Hz and 70 Hz.

SNR was defined as the ratio between the sound pressure level due to cardiac activity and the gradient switching induced sound pressure level. For example, for the frequency range between 10 Hz and 50 Hz a minimum signal to noise ratio of SNR = 30 dB was found for 2D CINE FLASH imaging at 7.0 T. To make acoustic triggering immune to interference from acoustic noise generated by gradient switching, separation of the acoustic cardiac activity from the higher frequency gradient noise was carried out by means of a third order inverse Chebychev filter using a UAF42 chip (Burr Brown Products by TI, Dallas, Texas, USA). The cut off frequency was set to f_c = 105 Hz since the energy of the first heart tone is mainly covered by frequencies ranging from 1 to 100 Hz. With this filtering no gradient noise peaks or peaks due to environmental noise were found within the relevant frequency range between 0 Hz to 105 Hz. The filtering yielded an attenuation of the gradient noise peaks found for frequencies above the cut-off frequency f_c = 105 Hz by at least 30 dB.

Assessment of ECG, POX and ACT Waveforms at 7.0 T

Off-line analysis of the log-files revealed that ECG waveforms were susceptible to severe distortions. Adverse signal elevation was found for cardiac phases where normally the T-wave occurs; a magneto-hydrodynamic effect which was pronounced at the isocenter of the magnet as illustrated in Figure 2, which shows ECG, POX and ACT traces derived from an individual subject over 18 cardiac cycles. ECG waveform distortions yielded an amplitude reaching the same order of magnitude or even larger than that of the R-wave. Pulse oximetry waveforms were free of interference from electromagnetic fields and magneto-hydrodynamic effects. A rather flat plateau and a significant scatter in the amplitude and width were observed for the peak in the POX trace. The peak in the POX trace showed a mean latency of approximately 350 ms with respect to the R-wave of the ECG trace. The acoustic approach provided waveforms free of interferences from electromagnetic fields or from magneto-hydrodynamic effects even in the isocenter of the 7.0 T magnet as illustrated in Figure 2. Off-line analysis of ECG and ACT traces yielded an average delay of Δt = 29.65 ms ± 4.43 ms between the R-wave and the first heart tone. This delay is not detrimental for whole R-R coverage 2D CINE FLASH using retrospective triggering.

Cardiac 2D CINE FLASH Imaging at 7.0 T

In the case of correct R-wave detection, ECG-gated 2D CINE FLASH imaging was found to be immune to cardiac motion effects as illustrated in figure 3 for one of the 9 subjects (subject 1). However, frequent R-wave mis-registration occurred in ECG-triggered acquisitions with a failure rate of up to 30% which manifests itself in a severe jitter of the R-wave detection tickmarks. Consequently, ECG triggered 2D CINE FLASH imaging was prone to severe cardiac motion artifacts if R-wave mis-registration occurred. For example, an ECG cardiac triggered whole heart coverage 2D CINE FLASH dataset obtained at diastole is shown in the top row of Figure 4 for one subject of the 9 subjects (subject 2). Images suffering from cardiac motion induced blurring are marked with dotted lines. Unlike ECG, ACT triggering produced images free of cardiac motion artefacts as illustrated in the bottom row of Figure 4 for the same subject. POX triggering 2D CINE FLASH acquisitions obtained from the same subject also produced images free of blood pulsation and cardiac motion artefacts as demonstrated in the middle row of Figure 4.

Assessment of the Trigger Detection Variance

Figure 5 shows mid-ventricular short axis views of the heart together with whole R-R interval time series of one-dimensional projections, trigger detection tickmarks and signal waveforms obtained at 7.0 T using ECG, POX and ACT triggered 2D CINE FLASH acquisitions for a midventricular slice derived from subject 1. In this example of almost correct recognition of the onset of cardiac activity, ECG, POX and ACT triggered 2D CINE FLASH imaging were found to be rather immune to the

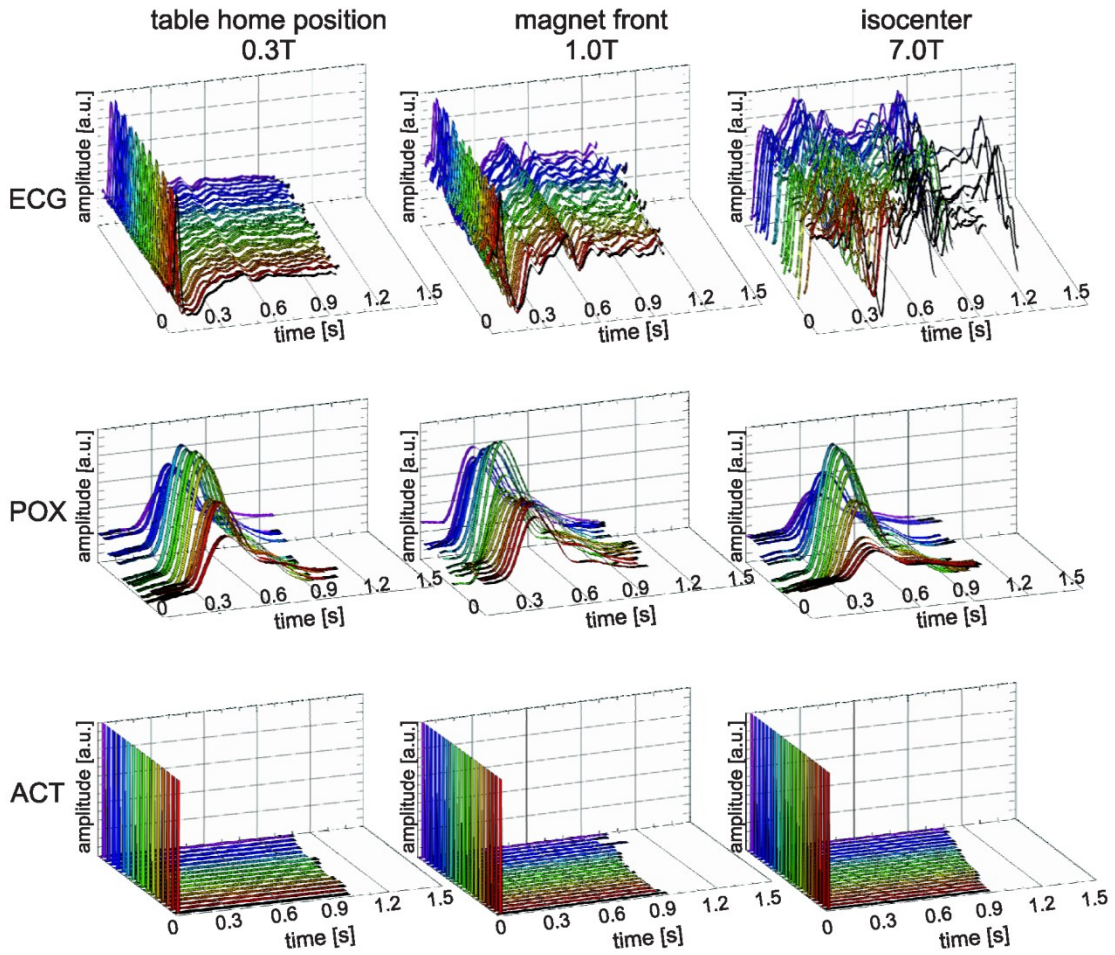

Figure 2 ECG, pulse oximetry and acoustic trigger signal traces acquired at three different field strengths. ECG **(top)**, pulse oximetry **(middle)** and acoustic trigger **(bottom)** signal traces derived from a healthy subject. Signal traces were recorded with the ECG, ACT and POX sensors located at the patient table home position **(left)**, at the front end of the 7.0 T magnet **(center)** and in the isocenter of the 7.0 T magnet **(right)** and post-processed and filtered by the scanners central physiological monitoring unit. Severe signal distortion occurred in the vector ECG signal obtained at the magnet's isocenter. A scatter in the amplitude and width was observed for the peak in the pulse oximetry trace. ACT is free of interferences with electromagnetic fields and magneto-hydrodynamic effects.

effects of cardiac motion. Consequently, the 2D CINE FLASH images derived from ECG, ACT and POX acquisitions together with the M-mode like whole R-R interval time series of one-dimensional projections along the cardiac phases safeguard recognition and delineation of the ventricular blood/myocardium interface. In spite of ECG's severe signal distortion faultless ECG triggering was observed for this example, with the exception of a scatter in the ECG trigger detection of approximately Δt = 60 ms which might compromise the temporal fidelity and hence might constitute a synchronization problem. Please note that a variance was also observed for the peak amplitude and peak width of the POX waveform as pointed out in Figure 5. This variance resulted in a trigger detection jitter of approximately Δt = 65 ms, which is equivalent to two cardiac phases. In comparison, ACT showed a 5 ms jitter which can be attributed to the ACT waveform sampling rate of 200 Hz.

Figure 6 shows an example of erroneous ECG triggering for a midventricular slice derived from subject 2. In this case, ECG triggered 2D CINE FLASH imaging was prone to severe cardiac motion artifacts due to R wave mis-registration. Trigger detection was found to be scattered across several cardiac phases including early

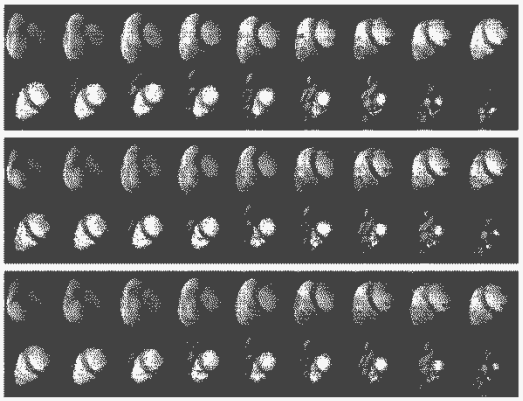

Figure 3 Short axis diastolic views free of cardiac motion effects. Short axis diastolic views obtained from breath-held base-to-apex 2D CINE FLASH acquisitions using **(top)** vector ECG, **(middle)** ACT and POX **(bottom)** gating. In this case of correct R-wave detection (subject 1), ECG-gated 2D CINE FLASH imaging was found to be immune to cardiac motion effects, as were ACT and POX gated acquisitions.

systole and diastole as demonstrated by the tickmarks depicted in Figure 6. R-wave mis-registration induced reduction in myocardium/blood contrast and image sharpness as illustrated by the short axis views together with whole R-R interval time series of one-dimensional projections. In comparison, ACT triggered 2D CINE FLASH imaging provided faultless trigger detection, accurate to the peak induced by the 1st heart tone and hence produced images free of motion artifacts. Please note the scatter in the POX peak amplitude and peak width, causing a jitter (Δt = 72 ms) in the pulse-oximetry trigger detection.

Mean R-R interval lengths deduced from the signal waveforms of ECG, POX and ACT triggered acquisitions are surveyed for each subject in Table 1 together with the standard deviation of the R-R interval length, which is a measure of the trigger detection accuracy. A close match in the mean R-R interval length and in the standard deviation of the R-R interval length derived from the assessment of the ECG, ACT and POX waveforms signifies correct trigger detection. A significant difference in the standard deviation of the R-R interval length deduced from ECG, ACT and POX waveforms indicates trigger (mis)registration at cardiac phases other than that which mark the onset of cardiac activity. Four out of nine healthy subjects showed a standard deviation for the cardiac cycle derived from ECG waveforms which was at least 1.5 times larger ($SD_{ECG} \geq 1.5 * SD_{ACT}$) than that obtained from ACT or POX waveforms.

Table 1 also surveys the standard deviation of the offset between the ECG's R-wave and the trigger detection moment which was derived from the ECG, POX and ACT waveforms and which was applied for synchronization. Four out of nine healthy subjects showed a standard deviation for the cardiac trigger offset derived from ECG waveforms which was at least four times larger ($SD_{ECG} \geq 4 * SD_{ACT}$) than that observed for ACT or POX waveforms.

Left Ventricular Parameter Assessment

Left ventricular volumes, mass and ejection fraction deduced from ECG, POX and ACT triggered acquisitions are surveyed in Figure 7. For each subject, the mean of the two measurements (ACT vs. ECG and ACT vs. POX) and the difference between the LV parameter obtained for ECG, POX and ACT triggered 2D CINE FLASH acquisitions are shown using Bland-Altman plots. The mean LV parameter derived from ECG triggered 2D CINE FLASH acquisitions were ESV = 74 ± 22ml, EDV = 170 ± 43ml, LVM = 130 ± 17) g, EF = 57 ± 8%. The mean LV parameter obtained from POX triggered 2D CINE FLASH acquisitions showed ESV = 67 ± 19 ml, EDV = 168 ± 44 ml, LVM = 130 ± 15g, EF = 60 ± 5%. In comparison, the ACT-triggered acquisitions yielded: ESV = 66 ± 20 ml, EDV = 173 ± 43 ml, LVM = 130 ± 15g, EF = 62 ± 3%. T-test revealed no significant differences for LV parameter derived from ACT, POX and ECG triggered acquisitions (all $p > 0.05$).

Image Quality Assessment

The application of acoustic triggering substantially improved the 2D CINE FLASH image quality as compared to the conventional approach. The blinded reading yielded a mean image quality score of 1.7 ± 0.5 for end-diastolic and 1.3 ± 0.6 for end-systolic cardiac images derived from ECG gated acquisitions. In comparison POX gated acquisitions yielded a mean image quality score of 2.0 ± 0.5 for end-diastolic and of 1.6 ± 0.5 for end-systolic cardiac phases. ACT triggered images showed a mean image quality score of 2.4 ± 0.5 for end-diastolic and of 2.0 ± 0.5 end-systolic cardiac phases as summarized in Table 2. A comparison between the image quality score obtained for ACT, POX and ECG gating using Wilcoxon paired test revealed significant differences between ACT vs. ECG gated acquisitions ($p = 0.10$ for endsystole, $p = 0.04$ for enddiastole) and for ACT vs. POX gated acquisitions ($p = 0.03$ for endsystole, $p = 0.01$ for enddiastole). The image quality comparison between ECG vs. POX gated acquisitions showed no significant differences in image quality ($p = 0.40$ for endsystole, $p = 0.34$ for enddiastole).

In case of faultless gating the EBS analysis revealed similar results for all synchronisation techniques. ECG

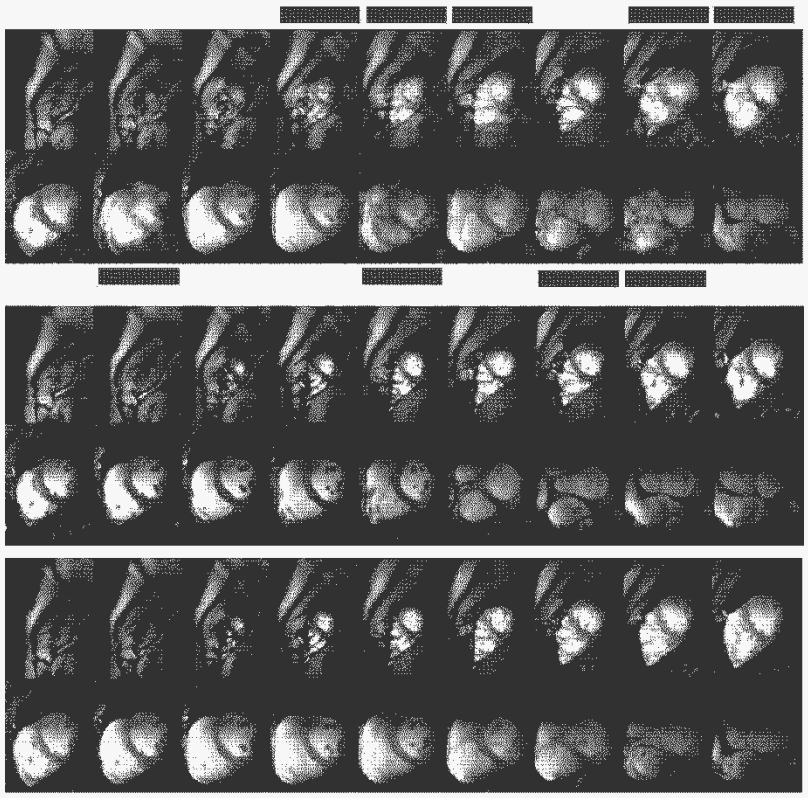

Figure 4 Short axis diastolic views showing cardiac motion artifacts when using ECG gating. Short axis diastolic views obtained from breath-held apex-to-base 2D CINE FLASH acquisitions using **(top)** vector ECG, **(middle)** ACT and POX **(bottom)** gating. In this subject (subject 2) vector ECG triggered 2D CINE FLASH imaging was prone to severe cardiac motion artifacts if R-wave mis-registration occurred. Images suffering from cardiac motion induced blurring are marked with grey bars. Acoustic triggering and POX provided image quality free of interferences from cardiac motion effects.

gated acquisitions showed an average EBS of (2.2 ± 0.3) pixels. ACT gated acquisitions yielded an average EBS of (2. 1 ± 0.2) pixels, and POX gated acquisitions showed an average EBS of (2.1 ± 0.2) pixels. In case of erroneously ECG gated acquisitions EBS analysis was challenging due to heavily reduced contrast to noise ratio (CNR) between blood and myocardium. The CNR degradation was caused by severe signal blurring across the endocardial border, as demonstrated in Figure 4.

Discussion

CMR at 7.0 T is still in its infancy and needs to continue to be very carefully validated against CMR applications very well established at 1.5 T and 3.0 T [29]. In current basic and clinical research practice some of the traits of ultrahigh field CMR are offset by challenges intrinsic to the use of ultrahigh magnetic field strength such as the synchronization of data acquisition with cardiac motion using traditional electrocardiographic (ECG) techniques. To address this issue, this study examines the applicability of acoustic cardiac triggering for CMR at 7.0 T in healthy volunteers, as a precursor to a larger clinical study. The acoustic approach was found to be immune to interference from environmental and gradient switching induced acoustic fields plus to be free of interference from electromagnetic fields and magneto-hydrodynamic effects. The efficacy and reliability of acoustic triggering is demonstrated by eliminating the frequently-encountered difficulty of mis-triggering due to ECG-waveform distortions or temporal jittering in the pulse-oximetry synchronization. R-wave mis-registration occurred in ECG-triggered acquisitions with a failure rate of up to 30% which manifest itself in severe cardiac motion induced image blurring.

It should be noted, that ECG trigger mis-registration was not equally distributed across the entire cardiac cycle but occurred at cardiac phases with large amplitude or up-slope in the ECG waveform including (i) an

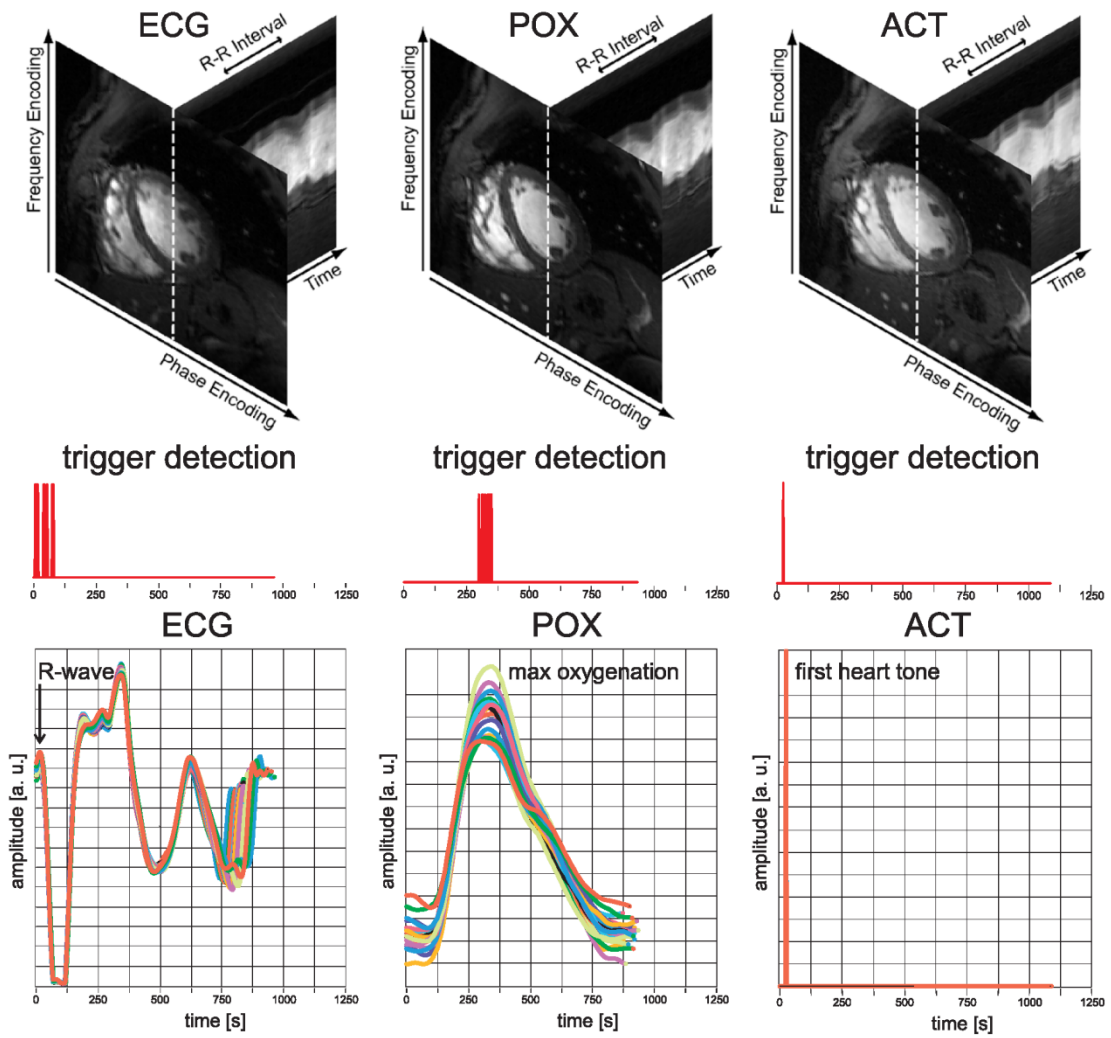

Figure 5 Example of correct ECG trigger detection. Cardiac images, trigger detection tickmarks and signal waveforms obtained at 7.0 T using vector ECG (left), pulse oximetry (center) and acoustically triggered (right) 2D CINE FLASH acquisitions. All signal waveforms show the output of the scanners central physiological monitoring unit (including processing of the ECG, POX and ACT signal) as displayed at the scanners user interface. Top: Mid-ventricular, short axis views of the heart together with whole R-R interval time series of one-dimensional projections along the profile (dotted line) marked in the short axis view. Middle: Trigger detection tickmarks obtained from a single subject over 18 cardiac cycles after temporal realignment using cross correlation and reassignment. Bottom: Signal waveforms obtained from a single subject (subject 1) over 18 cardiac cycles. In spite of vector ECG's severe signal distortion faultless vector ECG triggering was observed for this example. Hence, in this example of correct recognition of the onset of cardiac activity, vector ECG, POX and ACT triggered 2D CINE FLASH imaging were found to be immune to the effects of cardiac motion. Please note the jitter in the vector ECG (Δt = 60 ms) and in the pulse oximetry trigger (Δt = 65 ms) detection.

initial peak which covers the R-wave and (ii) major waveform distortions at systole and end-diastole. This mis-triggering behavior forces the k-space segmentation and retrospective reconstruction strategy to combine and assign k-space data which were acquired at different phases of myocardial contraction and relaxation to the same cardiac phase used to form a final image. This out-of-sync assignment causes severe degradation in image quality and image sharpness. Please note that this study did not yield missed ECG triggers. Missed triggers

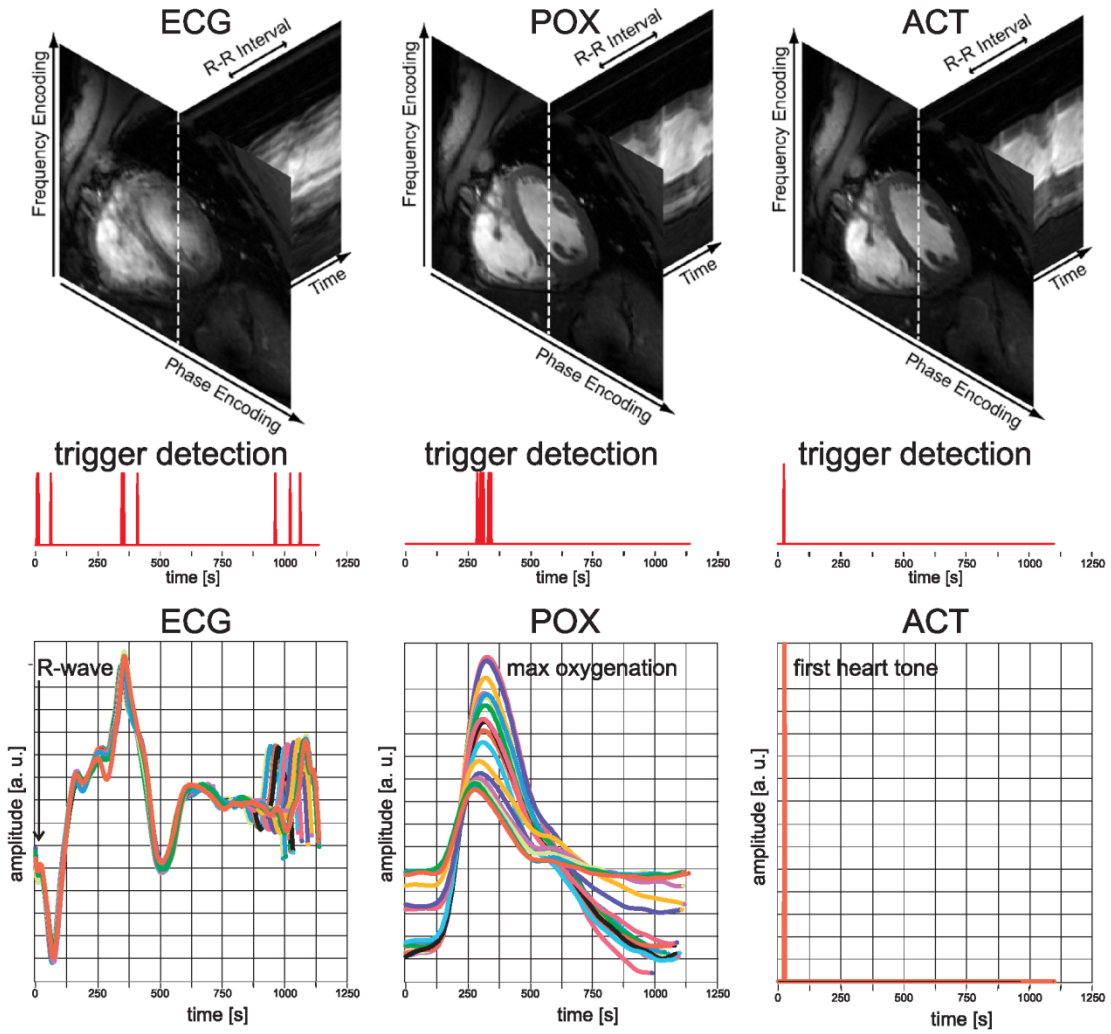

Figure 6 Example of erroneous ECG trigger detection. Cardiac images, trigger detection tickmarks and signal waveforms obtained at 7.0 T using vector ECG **(left)**, pulse oximetry **(center)** and acoustically triggered **(right)** 2D CINE FLASH acquisitions. All signal waveforms show the output of the scanners central physiological monitoring unit (including processing of the ECG, POX and ACT signal) as displayed at the scanners user interface. **Top**: Mid-ventricular, short axis views of the heart together with whole R-R interval time series of one-dimensional projections along the profile (dotted line) marked in the short axis view. **Middle**: Trigger detection tickmarks obtained from a single subject over 18 cardiac cycles after temporal realignment using cross correlation and reassignment. **Bottom**: Signal waveforms obtained from a single subject (subject 2) over 18 cardiac cycles. In this example vector ECG triggered CINE imaging was prone to severe cardiac motion artifacts due to R wave mis-registration which induced reduction in myocardium/blood contrast and image sharpness. ACT triggered 2D CINE FLASH imaging provided faultless trigger detection and hence produced images free of motion artifacts. Please note the scatter in the POX peak amplitude and peak width, causing a jitter (Δt = 72 ms) in the pulse oximetry trigger detection which constituted a synchronization problem.

would not compromise image quality but lengthen the acquisition time. Acoustically triggered 2D CINE FLASH imaging at 7.0 T produced images free of motion artifacts, as did pulse oximetry triggered 2D CINE FLASH imaging. The latter showed a scatter in the POX peak amplitude and peak width, causing a jitter of approximately Δt = 72 ms in the pulse-oximetry based trigger detection. This might be tolerable for a temporal resolution of 30 ms to 50 ms commonly used in conventional CINE imaging since data acquisition is distributed over several cardiac cycles which might result in averaging of motion effects. However, it stands

Table 1 Synopsis of the trigger detection variance assessment

Subject	Mean cardiac interval length (ms)			Standard deviation of the mean cardiac interval length (ms)			Standard deviation of the cardiac trigger offset (ms)		
	ACT	ECG	POX	ACT	ECG	POX	ACT	ECG	POX
1	869	865	840	89	54	45	78	10	11
2	870	795	1103	83	126	87	76	477	101
3	875	845	834	48	28	34	13	3	19
4	1064	999	1079	76	143	52	44	456	456
5	926	990	923	49	54	31	14	56	23
6	841	939	898	95	69	35	149	52	15
7	848	839	876	79	62	48	75	257	67
8	1110	886	1091	37	174	33	1	1047	14
9	762	576	660	81	168	144	112	488	331

Synopsis of the mean R-R interval lengths, standard deviation of the mean R-R interval lengths and standard deviation of the cardiac trigger detection offset deduced from the signal waveforms of ECG, POX and ACT triggered acquisitions. A significant difference in the standard deviation of the R-R interval length deduced from ECG, ACT and POX waveforms indicates trigger misregistration. A large standard deviation of the offset between the ECG's R-wave and the trigger detection which was derived from the ECG, POX and ACT waveforms indicates trigger misregistration.

to reason that the enhanced temporal resolution of CINE imaging facilitated by the signal-to-noise benefit at high and ultra-high fields [30] combined with the speed gain of parallel cardiac imaging [31] can be used to generate highly accurate time-series curves for wall motion tracking (i) to determine the exact time point of maximal systolic contraction and diastolic filling including assessment of mechanical dyssynchrony and (ii) to visualize small rapidly moving structures. Taking the underlying physiological temporal resolution into account it is fair to assume that a jitter in the POX trigger detection larger than 2-3 cardiac phases might diminish the temporal fidelity needed to characterize those physiologic phenomena within the cardiac cycle. Hence, the trigger detection jitter observed for pulse oximetry can constitute a challenge for reliable synchronization of data acquisition with the cardiac cycle. Another drawback of pulse oximetry is the latency between cardiac activity and trigger registration caused by the travel time of blood between the heart and the sensor position which can be in the order of several hundreds of milliseconds but which can also depend on (patho)physiology.

Acoustic triggering presents no risk of high voltage induction and patient burns, patient comfort and ease of clinical use, which all have, patient comfort, safety and practical implications. With reliable ACT triggering available, a positively-inclined practitioner might envisage using the merits of ACT to further simplify clinical CMR. For example, LV assessment is routinely conducted using 2D CINE imaging encompassing a stack of end-expiratory breath-held short axis views of the heart ranging from the atrioventricular ring to the apex. In current clinical practice, it is common to plan and scan each slice in an independent series instead of scanning all slices in a single series because of the frequently encountered risk of mis-triggering. This practical work around bears the advantage that only the most recently acquired slice needs to be re-scanned in case of non-diagnostic image quality due to mis-synchronization. Overcoming the hassle of ECG triggering, reliable triggering using ACT holds the promise to obviate the need for creating an independent series for each slice. Hence ACT, may help to streamline CINE imaging by using a single series for the entire stack of slices which has practical, data storage, data handling and data mining implications.

Admittedly, acoustic cardiac gating shares an apparent drawback of conventional ECG and pulse oximetry based cardiac triggering/gating that extra hardware is required for signal detection and processing, although the current ACT setup does not disturb the scanners certification. To overcome the constraint of using ancillary hardware various self-gating methods have been proposed and it's feasibility has been demonstrated for CMR [7,8,10,32]. However, self-gated CMR of small displacements such as vessel wall motion or MR angiography (MRA) remains a challenge due to the small changes in blood volume, low changes in vessel size and small vessel displacements throughout the cardiac cycle. The acoustic cardiac gating approach reported here is conceptually appealing for the pursuit of vascular CMR since the acoustic sensor can be used to directly detect vessel pulsation from larger vessels included in the target vessel territory.

It should be noted that the work reported here is limited to using vector ECG recordings and retrospective reconstruction techniques implemented on a clinical platform. Further fine-tuning of the post-processing and image reconstruction procedures used in current clinical

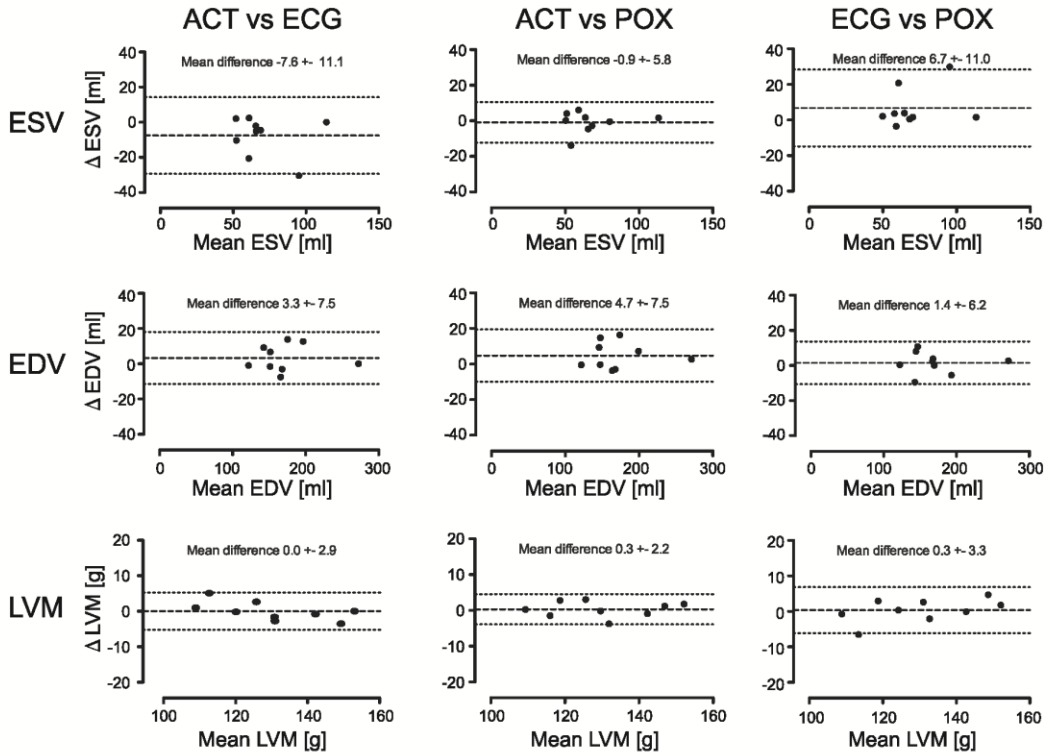

Figure 7 Comparison of cardiac chamber quantification parameters obtained for three triggering methods. Bland-Altman plots showing for each subject the mean of two measurements (ACT vs ECG, ACT vs POX and ECG vs POX) and the difference in the left ventricular parameter derived from vector ECG, ACT and POX gated 2D CINE FLASH acquisitions at 7.0 T. Dashed black lines in the Bland-Altman plots represent the mean difference while the dotted lines embody the confidence interval which was set to the mean value ± 1.96 of the standard.

Table 2 Synopsis of the image quality assessment

	End-diastolic Phase			End-systolic Phase		
Subject	**ACT**	**ECG**	**POX**	**ACT**	**ECG**	**POX**
1	2,4	2,2	1,8	1,5	1,6	1,7
2	2,6	0,9	1,9	2,1	0,5	1,6
3	2,9	2,7	2,5	2,6	2,4	2,1
4	2,9	1,7	2,8	2,6	1,2	2,4
5	2,5	1,9	1,9	2,1	1,7	1,7
6	1,6	2,1	1,8	1,5	1,5	1,4
7	1,5	1,6	1,1	1,1	1,6	1,0
8	2,8	1,1	2,4	2,4	0,8	1,5
9	2,1	0,7	1,3	1,9	0,5	0,9
Mean	**2,4**	**1,7**	**2,0**	**2,0**	**1,3**	**1,6**
SD (+/-)	**0,5**	**0,7**	**0,5**	**0,5**	**0,6**	**0,5**

Mean values of image quality scores for each subject and trigger approach. Overall image quality of end-diastolic and end-systolic images was rated using a scale ranging from 0 to 3 for each slice (0 - images with poor and non-diagnostic quality due to cardiac motion induced blurring, 1 - image quality impaired by cardiac motion which may lead to misdiagnosis, 2 - good image quality, cardiac motion artifacts hard to recognize and 3 - excellent image quality, no cardiac motion artifacts observed). Please note that the poor scores obtained for subject 7 are due to respiration induced motion artifacts.

practice including cross-correlation of ECG signals obtained for different R-R intervals together with retrospective image reconstruction is conceptually appealing to enhance ECG's trigger detection accuracy, albeit this change in the manufacturers ECG processing/reconstruction methodology is beyond the scope of the work reported here.

Conclusion

The applicability of acoustic triggering for cardiac CINE imaging at 7.0 T was shown. The intrinsic insensitivity of the MR-stethoscope to interference from electromagnetic fields renders it suitable for left ventricular parameter assessment at 7.0 T due to its excellent trigger reliability, which is superior to that of traditional ECG, VCG and conventional pulse oximetry. Acoustic cardiac triggering promises to be beneficial for ultra-high field strengths including 7.0 T and beyond, which is an important but challenging development looming on the pre-clinical research horizon. Although the full

range of ultrahigh field CMR is untapped yet, it is expected to drive future technological developments. With appropriate ancillary triggering hardware, RF-coil design and imaging techniques/protocols customized for 7.0 T applications, LV assessment and other CMR applications are feasible. While this is, for the moment, merely a start, it continues to motivate new basic and clinical research on ultrahigh field CMR, including extra efforts towards the development of a wireless signal transmission version of the acoustic triggering approach.

Author details
[1]Berlin Ultrahigh Field Facility (B.U.F.F.), Max-Delbrueck Center for Molecular Medicine, Berlin, Germany. [2]Siemens Healthcare, Erlangen, Germany. [3]Working Group on Cardiovascular Magnetic Resonance, Medical University Berlin, Charité Campus Buch, HELIOS-Klinikum Berlin-Buch, Dept. of Cardiology and Nephrology, Berlin, Germany. [4]Experimental and Clinical Research Center, Charité - Campus Buch, Humboldt-University, Berlin, Germany.

Authors' contributions
TF build the acoustic cardiac triggering device, performed the experiments, collected the data and was significantly involved in writing the manuscript. FH performed data evaluation and statistical analysis and was involved in editing the manuscript.TGO conducted analysis of the waveforms obtained for ACT, ECG and POX and was involved in editing the manuscript. MD has setup the CMR protocols for this study. FvK was responsible for the volunteer care, data documentation, left ventricular function analysis and image quality assessment. He was involved in editing the manuscript. MP performed image quality assessment. He was involved in editing the manuscript. JSM was significantly involved in the study and imaging protocol design. She was involved in editing the manuscript. TN was responsible for the overall concept, was significantly involved in the study and protocol design. He was also significantly involved in writing the manuscript.

Competing interests
Wolfgang Renz is a full-time employee of Siemens (Erlangen, Germany).

Received: 25 June 2010 Accepted: 16 November 2010
Published: 16 November 2010

References

1. Lanzer P, Botvinick EH, Schiller NB, Crooks LE, Arakawa M, Kaufman L, Davis PL, Herfkens R, Lipton MJ, Higgins CB: **Cardiac imaging using gated magnetic resonance.** *Radiology* 1984, **150**:121-127.
2. Brau AC, Wheeler CT, Hedlund LW, Johnson GA: **Fiber-optic stethoscope: a cardiac monitoring and gating system for magnetic resonance microscopy.** *Magn Reson Med* 2002, **47**:314-321.
3. Pattynama PM, van der Velde ET, Steendijk P, Lamb HJ, Baan J, de Roos A: **Cardiovascular MR imaging: pressure-gating using the arterial pressure signal from a conventional ferromagnetic micromanometer-tip catheter.** *Magn Reson Imaging* 1994, **12**:531-534.
4. Rubin JM, Fowlkes JB, Prince MR, Rhee RT, Chenevert TL: **Doppler US gating of cardiac MR imaging.** *Acad Radiol* 2000, **7**:1116-1122.
5. Buikman D, Helzel T, Roschmann P: **The rf coil as a sensitive motion detector for magnetic resonance imaging.** *Magn Reson Imaging* 1988, **6**:281-289.
6. Buehrer M, Curcic J, Boesiger P, Kozerke S: **Prospective self-gating for simultaneous compensation of cardiac and respiratory motion.** *Magn Reson Med* 2008, **60**:683-690.
7. Larson AC, White RD, Laub G, McVeigh ER, Li D, Simonetti OP: **Self-gated cardiac cine MRI.** *Magn Reson Med* 2004, **51**:93-102.
8. Larson AC, Kellman P, Arai A, Hirsch GA, McVeigh E, Li D, Simonetti OP: **Preliminary investigation of respiratory self-gating for free-breathing segmented cine MRI.** *Magn Reson Med* 2005, **53**:159-168.
9. Nijm GM, Sahakian AV, Swiryn S, Carr JC, Sheehan JJ, Larson AC: **Comparison of self-gated cine MRI retrospective cardiac synchronization algorithms.** *J Magn Reson Imaging* 2008, **28**:767-772.
10. Crowe ME, Larson AC, Zhang Q, Carr J, White RD, Li D, Simonetti OP: **Automated rectilinear self-gated cardiac cine imaging.** *Magn Reson Med* 2004, **52**:782-788.
11. Rengle A, Baboi L, Saint-Jalmes H, Sablong R, Beuf O: **Optical cardiac and respiratory device for synchronized MRI on small animal.** *Conf Proc IEEE Eng Med Biol Soc* 2007, 2046-2049.
12. Lanzer P, Barta C, Botvinick EH, Wiesendanger HU, Modin G, Higgins CB: **ECG-synchronized cardiac MR imaging: method and evaluation.** *Radiology* 1985, **155**:681-686.
13. Fischer SE, Wickline SA, Lorenz CH: **Novel real-time R-wave detection algorithm based on the vectorcardiogram for accurate gated magnetic resonance acquisitions.** *Magn Reson Med* 1999, **42**:361-370.
14. Chia JM, Fischer SE, Wickline SA, Lorenz CH: **Performance of QRS detection for cardiac magnetic resonance imaging with a novel vectorcardiographic triggering method.** *J Magn Reson Imaging* 2000, **12**:678-688.
15. Stuber M, Botnar RM, Fischer SE, Lamerichs R, Smink J, Harvey P, Manning WJ: **Preliminary report on in vivo coronary MRA at 3 Tesla in humans.** *Magn Reson Med* 2002, **48**:425-429.
16. Kugel H, Bremer C, Puschel M, Fischbach R, Lenzen H, Tombach B, Van Aken H, Heindel W: **Hazardous situation in the MR bore: induction in ECG leads causes fire.** *Eur Radiol* 2003, **13**:690-694.
17. Shellock FG, Kanal E: **Burns associated with the use of monitoring equipment during MR procedures.** *J Magn Reson Imaging* 1996, **6**:271-272.
18. Shellock FG, Crues JV: **MR procedures: biologic effects, safety, and patient care.** *Radiology* 2004, **232**:635-652.
19. Lange S, Nguyen QN: **Cables and electrodes can burn patients during MRI.** *Nursing* 2006, **36**:18.
20. Frauenrath T, Hezel F, Heinrichs U, Kozerke S, Utting JF, Kob M, Butenweg C, Boesiger P, Niendorf T: **Feasibility of cardiac gating free of interference with electro-magnetic fields at 1.5 Tesla, 3.0 Tesla and 7.0 Tesla using an MR-stethoscope.** *Invest Radiol* 2009, **44**:539-547.
21. Becker M, Frauenrath T, Hezel F, Krombach GA, Kremer U, Koppers B, Butenweg C, Goemmel A, Utting JF, Schulz-Menger J, Niendorf T: **Comparison of left ventricular function assessment using phonocardiogram- and electrocardiogram-triggered 2D SSFP CINE MR imaging at 1.5 T and 3.0 T.** *Eur Radiol* 2009.
22. Snyder CJ, DelaBarre L, Metzger GJ, van de Moortele PF, Akgun C, Ugurbil K, Vaughan JT: **Initial results of cardiac imaging at 7 Tesla.** *Magn Reson Med* 2009, **61**:517-524.
23. Frauenrath T, Niendorf T, Kob M: **Acoustic Method for Synchronization of Magnetic Resonance Imaging (MRI).** *Acta Acustica united with Acustica* 2008, **94**:148-155.
24. Brants A, Versluis M, de Roos A, Westenberg J, Webb A: **Quantitative comparison of left ventricular cardiac volume, mass and function obtained at 7 Tesla with "gold standard" values at 1.5 Tesla.** *Proc Intl Soc Mag Reson Med; Stockholm, SE* 2010, 1299.
25. Brandts A, Westenberg JJ, Versluis MJ, Kroft LJ, Smith NB, Webb AG, de Roos A: **Quantitative assessment of left ventricular function in humans at 7 T.** *Magn Reson Med* 2010.
26. Maderwald S, Nassenstein K, Orzada S, Schäfer LC, Oehmigen M, Bitz AK, Kraff O, Brote I, Ladd SC, Ladd ME, Quick HH: **MR imaging of cardiac wall-motion at 1.5T and 7T: SNR and CNR comparison.** *Proc Intl Soc Mag Reson Med; Stockholm, SE* 2010, 1299.
27. Renz W, Lindel T, Seifert F, Hoffmann W, Schulz-Menger J, Ittermann B: **A 4 channel TX/RX decoupled loop array for cardiac/body imaging at 7T.** *26th Annual Scientific Meeting of the European Society for Magnetic Resonance in Medicine and Biology; Antalya, TR* 2009, 476.
28. Bland JMAD: **Statistical method for assessing agreement between two methods of clinical measurement.** *Lancet* 1986, 307-310.
29. von Knobelsdorff-Brenkenhoff F, Frauenrath T, Prothmann M, Dieringer MA, Hezel F, Renz W, Kretschel K, Niendorf T, Schulz-Menger J: **Cardiac chamber quantification using magnetic resonance imaging at 7 Tesla-a pilot study.** *Eur Radiol* 2010, **20(12)**:2844-52.
30. Gutberlet M, Noeske R, Schwinge K, Freyhardt P, Felix R, Niendorf T: **Comprehensive Cardiac Magnetic Resonance Imaging at 3.0 Tesla: Feasibility and Implications for Clinical Applications.** *Invest Radiol* 2006, **41**:154-167.

Comparison of three multichannel transmit/receive radiofrequency coil configurations for anatomic and functional cardiac MRI at 7.0T: implications for clinical imaging

Winter L, Kellman P, Renz W, Gräßl A, Hezel F, Thalhammer C, von Knobelsdorff-Brenkenhoff F, Tkachenko V, Schulz-Menger J, Niendorf T.

Eur Radiol. 2012 Oct;22(10):2211-20

http://dx.doi.org/10.1007/s00330-012-2487-1

Two-dimensional sixteen channel transmit/receive coil array for cardiac MRI at 7.0 T: design, evaluation, and application.

Thalhammer C, Renz W, Winter L, Hezel F, Rieger J, Pfeiffer H, Graessl A, Seifert F, Hoffmann W, von Knobelsdorff-Brenkenhoff F, Tkachenko V, Schulz-Menger J, Kellman P, Niendorf T.

J Magn Reson Imaging. 2012 Oct;36(4):847-57

http://dx.doi.org/10.1002/jmri.23724

Progress and promises of human cardiac magnetic resonance at ultrahigh fields: A physics perspective

Niendorf T, Graessl A, Thalhammer C, Dieringer MA, Kraus O, Santoro D, Fuchs K, Hezel F, Waiczies S, Ittermann B, Winter L.
J Magn Reson. 2013 Apr;229:208-22

http://dx.doi.org/10.1016/j.jmr.2012.11.015

Isometric handgrip exercise during cardiovascular magnetic resonance imaging: Set-up and cardiovascular effects

von Knobelsdorff-Brenkenhoff F, Dieringer MA, Fuchs K, Hezel F, Niendorf T, Schulz-Menger J.
J Magn Reson Imaging 2013 Jun;37(6):1342-50

http://dx.doi.org/10.1002/jmri.23924

Journal of Cardiovascular Magnetic Resonance

RESEARCH Open Access

Assessment of the right ventricle with cardiovascular magnetic resonance at 7 Tesla

Florian von Knobelsdorff-Brenkenhoff[1,2†], Valeriy Tkachenko[1,2], Lukas Winter[1], Jan Rieger[1], Christof Thalhammer[1], Fabian Hezel[1], Andreas Graessl[1], Matthias A Dieringer[1,2], Thoralf Niendorf[1,3] and Jeanette Schulz-Menger[1,2*]

Abstract

Background: Functional and morphologic assessment of the right ventricle (RV) is of clinical importance. Cardiovascular magnetic resonance (CMR) at 1.5T has become gold standard for RV chamber quantification and assessment of even small wall motion abnormalities, but tissue analysis is still hampered by limited spatial resolution. CMR at 7T promises increased resolution, but is technically challenging. We examined the feasibility of cine imaging at 7T to assess the RV.

Methods: Nine healthy volunteers underwent CMR at 7T using a 16-element TX/RX coil and acoustic cardiac gating. 1.5T served as gold standard. At 1.5T, steady-state free-precession (SSFP) cine imaging with voxel size (1.2x1.2x6) mm^3 was used; at 7T, fast gradient echo (FGRE) with voxel size (1.2x1.2x6) mm^3 and (1.3x1.3x4) mm^3 were applied. RV dimensions (RVEDV, RVESV), RV mass (RVM) and RV function (RVEF) were quantified in transverse slices. Overall image quality, image contrast and image homogeneity were assessed in transverse and sagittal views.

Results: All scans provided diagnostic image quality. Overall image quality and image contrast of transverse RV views were rated equally for SSFP at 1.5T and FGRE at 7T with voxel size (1.3x1.3x4)mm^3. FGRE at 7T provided significantly lower image homogeneity compared to SSFP at 1.5T. RVEDV, RVESV, RVEF and RVM did not differ significantly and agreed close between SSFP at 1.5T and FGRE at 7T (p=0.5850; p=0.5462; p=0.2789; p=0.0743). FGRE at 7T with voxel size (1.3x1.3x4) mm^3 tended to overestimate RV volumes compared to SSFP at 1.5T (mean difference of RVEDV 8.2±9.3ml) and to FGRE at 7T with voxel size (1.2x1.2x6) mm^3 (mean difference of RVEDV 9.3±8.6ml).

Conclusions: FGRE cine imaging of the RV at 7T was feasible and provided good image quality. RV dimensions and function were comparable to SSFP at 1.5T as gold standard.

Keywords: Magnetic resonance imaging, Right ventricle, Ultrahigh field, Cardiac

Background

Function, size and morphology of the right cardiac ventricle (RV) are known to be strong influencing factors on morbidity and mortality in various cardiac diseases, for instance congenital heart disease, pulmonary hypertension, myocardial infarction or arrythmogenic right ventricular cardiomyopathy (ARVC) [1-4]. However, their evaluation by using non-invasive imaging techniques is often a challenge, mainly attributable to the asymmetric and highly variable shape of the RV, the predominantly longitudinal systolic shortening, the small myocardial wall thickness and the location behind the sternum. Cardiovascular magnetic resonance (CMR), mainly using steady-state free-precession (SSFP) cine imaging at a field strength of 1.5Tesla (T), has evolved as the gold standard for the assessment of RV dimensions and function due to its ability to image in any plane, its excellent blood-tissue contrast, its capability to depict even small wall motion abnormalities and its proven reproducibility [4-7]. Nevertheless, expectations to characterize the myocardial tissue of the RV comparable to the LV including the differentiation of fibrosis, fat or edema, remained widely unaccomplished yet. As an example, the current task force criteria to assess ARVC include CMR to assess RV

* Correspondence: jeanette.schulz-menger@charite.de
†Equal contributors
[1]Berlin Ultrahigh Field Facility (B.U.F.F.), Max-Delbrueck Center for Molecular Medicine, Berlin, Germany
[2]Working Group on Cardiovascular Magnetic Resonance, Experimental and Clinical Research Center, a joint cooperation between the Charité Medical Faculty and the Max-Delbrueck Center for Molecular Medicine, HELIOS Klinikum Berlin Buch, Department of Cardiology and Nephrology, Berlin, Germany
Full list of author information is available at the end of the article

size and function, but emphasize that the evidence of fibro-fatty replacement within the RV wall is only obtained by endomyocardial biopsy [4]. Even the accuracy of CMR to quantify RV mass, which is known to be an important predictor of cardiovascular events, is uncertain due to the challenge of resolving the thin (2-5mm) RV free wall properly using protocols (typical voxel size of cine imaging 1.8x1.8x6mm^3) common in today's clinical [8-10]. To extend the information that is extractable from CMR, technological improvements that increase the spatial and temporal resolution as well as signal-to-noise ratio (SNR) are therefore desired. As field strength positively correlates with SNR, CMR at ultrahigh fields (7T) offers the potential to depict even microscopic structures and to facilitate targeted tissue characterization [11,12]. However, imaging at 7T comes with technical challenges, like increased B_0 heterogeneities, non-uniform B_1 distribution and increased radio frequency (RF) power deposition. Recently, the technical feasibility of cardiac cine imaging at 7T using fast gradient echo (FGRE) techniques has been demonstrated, and data demonstrating the ability for accurate LV chamber quantification at 7T were reported [13-16]. Moreover, dedicated transmit and receive coils as well as cardiac trigger techniques have been developed to meet the demands of CMR at 7T [17-21].

Aim of the present study was to extend the application of cine imaging at 7T to the assessment of RV size and function and to compare the results with the gold standard at 1.5T. This work is regarded as the first step toward a comprehensive assessment of RV function, size and morphology using CMR at 7T.

Methods

Subjects

Nine healthy volunteers (6 males; mean age 29±5 years, range 24–38 years; mean body mass index 22±2 kg/m^2, range 18-24kg/m^2) underwent CMR at 1.5T and at 7T. The status "healthy" was based on: i) uneventful medical history, ii) absence of any symptoms indicating cardiovascular dysfunction, iii) normal ECG, iv) normal cardiac dimensions and function on the CMR cine images of this study. The local ethics committee approved the study, and all subjects gave written informed consent to participate in the study.

MR and RF coil technology at 7T

A 7T whole body MR system (Siemens Healthcare, Erlangen, Germany) equipped with an Avanto (Siemens Healthcare, Erlangen, Germany) gradient system (slew rate: 200 T/m/s, max. gradient strength: 40mT/m) and an 8kW RF amplifier (Stolberg HF-Technik AG, Stolberg-Vicht, Germany) was used. A 16 channel transceiver coil array tailored for cardiac MR at 7.0 T [19,20] that uses loop elements and consists of two sections was applied: A planar posterior section located below the patient's chest and a modestly curved anterior section positioned on top of the patient's chest. Each section contains an identical arrangement of 8 TX/RX elements, connected to the MR system via a coil interface comprising 16 TX/RX switches and low-noise preamplifiers (Stark Contrasts, Erlangen, Germany). To drive each channel of the coil the output of the RF amplifier was split into 16 equal-intensity signals using a home-built 16x16 Butler matrix. The transmit phases of the individual coil elements were adjusted by using the 1st order circular polarized (cp) mode of the Butler matrix with an increment of 22.5 degrees between subsequent output channels in conjunction with −78° phase shifting coaxial cables for all posterior coil elements [20].

MR and RF coil technology at 1.5T

At 1.5T a Magnetom Avanto (Siemens Healthcare, Erlangen, Germany) system equipped with the same gradient coil used at 7.0 T was used. A TX body coil was used for transmission and a 12-channel RX body array coil was used for reception.

Cardiac gating

Since electrocardiography is corrupted by interference with electromagnetic fields and by magneto-hydrodynamic effects at 7T, acoustic cardiac triggering (ACT) was applied (EasyACT, MRI.TOOLS GmbH, Berlin, Germany). ACT registers the first heart tone of the phonocardiogram to synchronize data acquisition with cardiac motion [21]. ACT was used for retrospective gating at 7T and at 1.5T to ensure consistency throughout the study.

Slice positioning

One technician with profound experience performed all scans at 1.5T and 7.0T to ensure reproducibility and consistency. After acquisition of scout images, standard four- and two-chamber views as well as a long axis view of the RV were acquired. Next, a stack of transverse slices covering the entire RV was obtained twice using two voxel dimensions. These images served for RV volumetry and evaluation of image quality. Furthermore, a stack of sagittal slices covering the entire RV was acquired. These images only served for evaluation of image quality.

Imaging parameters

At 7T, cine images were acquired using 2D FGRE. Each slice was acquired in an end-expiratory breath-hold. Imaging parameters were: echo time TE=2.7ms, repetition time TR=5.6ms, nominal flip angle FA=32°, transmit reference voltage U_{ref} 400 V, peak voltage of sinc-pulse

(t=800 μs) U_{peak} 190V, voxel size (1.2x1.2x6)mm^3, no interslice gap, bandwidth 444Hz/pixel, 30 phases per heart cycle, parallel imaging (R=2, 32 calibration lines) in conjunction with GRAPPA reconstruction. For the transverse stack a second scan was performed using the same imaging parameters with the exception of the spatial resolution, which was adjusted to a voxel size of (1.3x1.3x4)mm^3. Prior to RV function assessment volume selective second order B_0-shimming was performed.

At 1.5T, a clinically established SSFP cine protocol was used. Imaging parameters were: TE=1.3ms, TR=3.0ms, FA=70°, voxel size (1.2x1.2x6)mm^3, no interslice gap, bandwidth 790Hz/pixel, 30 phases per heart cycle, parallel imaging (R=2, 32 calibration lines) in conjunction with GRAPPA reconstruction.

Image interpretation

The CMR images were read in consensus by two physicians (FvKB, VT) with very profound experience in CMR both at 7T and 1.5T [14,19,7]. The software CMR42® (Circle Cardiovascular Imaging, Calgary, Canada) was used. *Quantitatively*, RV end-diastolic volume (RVEDV), RV end-systolic volume (RVESV), RV ejection fraction (RVEF) and RV mass (RVM) were obtained by manually contouring endocardial borders in end-diastole and end-systole as well as epicardial borders in end-diastole. *Qualitatively*, each cine slice was scored in diastole and systole regarding overall image quality, homogeneity and contrast. The decision was based on anatomic border sharpness, visualization of subtle anatomic features and presence of artifacts. i) Overall image quality: 0=poor, non-diagnostic; 1=impaired image quality that may lead to misdiagnosis; 2=good; and 3=excellent. ii) Homogeneity: 0=inhomogeneous image or artifacts that may impair diagnostic quality; 1=homogeneous image, no artifact present. iii) Image contrast: 0=low or poor contrast between anatomical structures and blood pool; 1=sufficient contrast between anatomical structures and blood pool.

Statistical analysis

Continuous values (RVEDV, RVESV, RVEF, RVM) are displayed as median and range. Kruskal-Wallis tests were performed to evaluate differences between CMR settings (1.5T vs. 7T with voxel size (1.2x1.2x6)mm^3 vs. 7T with voxel size (1.3x1.3x4)mm^3). Bland-Altman analyses were performed to assess the pairwise agreement. For categorical data (image quality, contrast, homogeneity), relative frequencies are shown. Multinomial or logistic regression was used to evaluate differences between the different CMR settings. The regression analyses were based on generalized estimation equations with independence as working correlation matrix to account for multiple measurements per patient. A p-value of less than 0.05 was regarded as statistically significant. Calculations were done with SAS 9.2 (SAS Institute Inc., Cary, NC, USA).

Results

Evaluation of overall image quality, image contrast and homogeneity

Image quality was diagnostic in all CMR examinations at 1.5T and 7T, with no examination scored as "poor / non-diagnostic" (score 0). Figure 1 exemplarily depicts a four-chamber view, a RV long axis view and a mid-ventricular transverse slice of the RV obtained with FGRE at 7T together with SSFP images derived from 1.5T. Figure 2 provides an overview of the four-chamber views of all subjects derived from 7T. Additional movie files show cines of the RV long axis and the transverse slice acquired at 7T in one subject, and a composition of the four-chamber views of all study participants obtained at 7T (see Additional files 1, 2 and 3).

The results of the evaluation of overall image quality, image contrast and homogeneity are summarized in Figure 3:

Regarding *overall image quality*, SSFP at 1.5T and FGRE at 7T with voxel size (1.3x1.3x4)mm^3 provided a significantly higher proportion of "excellent image quality" (66.4% and 43.8%) compared to FGRE at 7T with voxel size (1.2x1.2x6)mm^3 (22.7%) in the transverse slice orientation in diastole ($p<0.0001$ and $p=0.0478$). For the sagittal slice orientation, SSFP cine images at 1.5T provided a significantly higher proportion of "excellent image quality" (75% in diastole and 87% in systole) compared to FGRE at 7T with voxel size (1.3x1.3x4)mm^3 (37% in diastole and 22% in systole) (each $p<0.0001$).

Regarding *image homogeneity*, SSFP at 1.5T provided significantly higher proportions of "homogeneous images" compared to the 7T acquisitions, both in transverse orientation in diastole ($p=0.0329$) and in systole ($p=0.0197$), and in sagittal orientation in diastole ($p=0.0002$) and systole ($p<0.0001$). The 7T groups did not differ significantly from each other.

Regarding *image contrast*, the various modalities were not found to differ significantly in transverse image orientation (diastole: $p=0.7290$; systole: $p=0.3170$), as well as in sagittal image orientation in diastole ($p=0.1182$). Only for systole in sagittal orientation, SSFP at 1.5T provided a higher proportion of images rated as "sufficient contrast" compared to FGRE at 7T with voxel size (1.3x1.3x4)mm^3 ($p=0.0463$).

RV chamber quantification

Median quantitative RV results are depicted in Table 1. No significant difference was found regarding RVEDV ($p=0.5850$), RVESV ($p=0.5462$), RVEF ($p=0.2789$) and

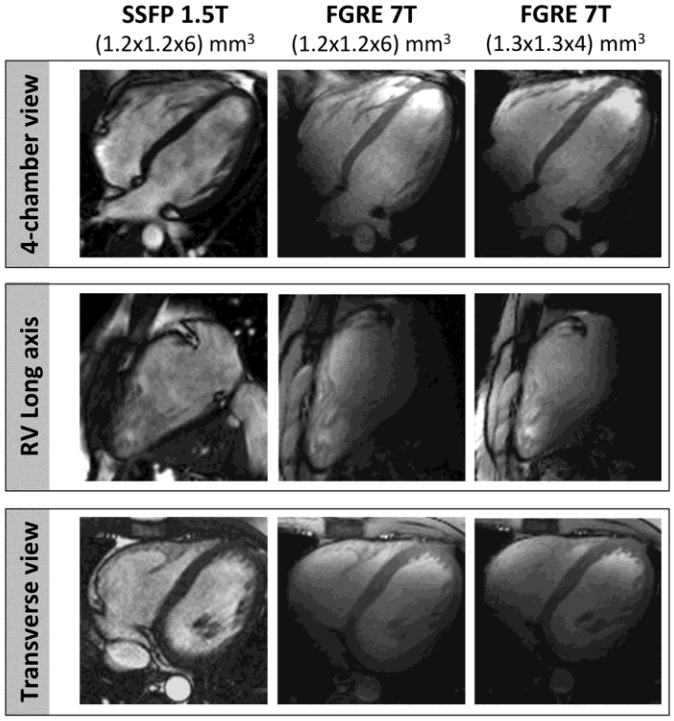

Figure 1 Cine imaging of the RV. Four-chamber view, RV long axis view and mid-ventricular transverse view obtained by SSFP at 1.5T with voxel size (1.2x1.2x6)mm^3*(left)*, by FGRE at 7T with voxel size (1.2x1.2x6)mm^3*(middle)* and by FGRE at 7T with voxel size (1.3x1.3x4)mm^3*(right)*.

RVM (p=0.0743) between SSFP at 1.5T and FGRE at 7T. Bland-Altman plots illustrating the agreement between the various approaches regarding REDV, RVESV, RVEF and RVM are shown in Figure 4. There was a tendency towards larger volumes with FGRE at 7T with voxel size (1.3x1.3x4)mm^3 both compared to SSFP at 1.5T (mean difference: RVEDV −8.2±9.3ml, RVESV −4.3±5.1ml) and FGRE at 7T with voxel size (1.2x1.2x6)mm^3 (mean difference: RVEDV −9.3±8.6ml, RVESV −6.0±4.5ml).

Discussion

The present results demonstrated that FGRE cine imaging of the RV at 7T using a dedicated 16-channel transceiver RF coil and acoustic cardiac gating provided good quality cine images of the RV to assess its size and function. The findings confirm preliminary experiences with the LV at 7T [14] and underline that cine imaging at 7T is feasible.

We know from studies of the LV with FGRE cine imaging at 1.5T and 7T that the step from 1.5T towards 7T improved the image quality of FGRE cine images, in particular in long axis acquisitions parallel to the blood flow [14]. The blood/myocardium contrast is known to be reduced with low blood flow, attributable to the inflow-dependent blood pool signal intensity in FGRE sequences [22]. The ultrahigh field strength has the potential to minimize this source of error due to different field strength dependent T_1 prolongation of blood and myocardium. Translated to the RV, this observation gains importance due to sometimes low blood flow between the RV trabeculae. In the present study of the RV, images in transverse orientation acquired with SSFP at 1.5T received the highest mean image score compared to the acquisitions at 7T. Notwithstanding, it is notable that our statistical analysis revealed that both field strengths did not differ significantly in overall image quality in systole in general, as well as in diastole if the enhanced spatial resolution (voxel size (1.3x1.3x4)mm^3) is regarded. This observation underlines the feasibility to obtain high-quality cine images of standard planes at 7T and forms the basement for accurate RV chamber quantification, which is predominantly done in transverse slices [6]. In contrast, the sagittal orientated slices exhibited significant differences in image quality between SSFP at 1.5T and FGRE at 7T, with SSFP at 1.5T being more often "excellent". The observation that the image quality at 7T varied dependent on slice orientation can be attributed to the complex B_1 field pattern

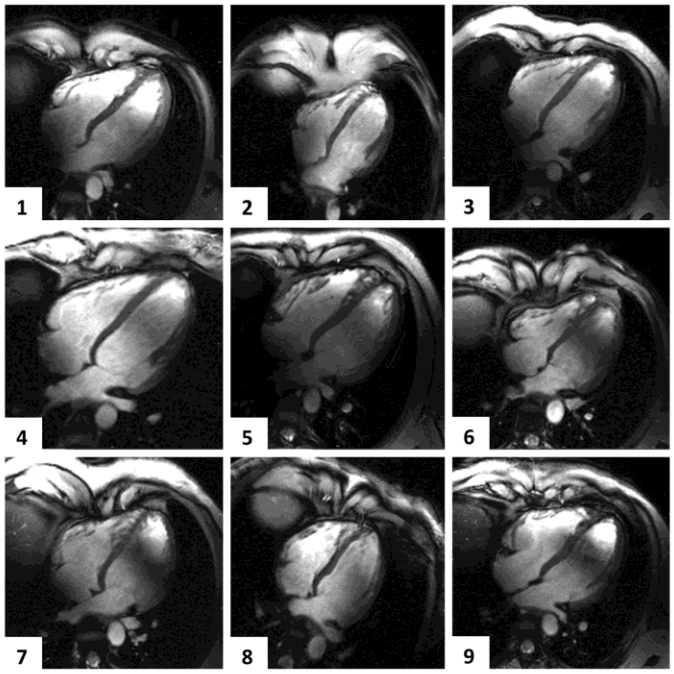

Figure 2 Cine imaging of the RV. Four-chamber views of all subjects obtained with 2D cine FGRE at 7T using a voxel size of (1.3x1.3x4) mm^3.

with various constructive and destructive interferences throughout the FOV. Depending on the volunteer and slice orientation, a specific field pattern is revealed. From a clinical perspective, sagittal views are currently mainly used to assess RV wall motion and morphology complementary to transverse slices. This comprehensive assessment is important for example in the diagnosis of ARVC, where regional akinesia, dyskinesia or asynchrony are relevant indicators [4]. Therefore, further technical improvements are necessary to enable patient and slice dependent transmit field shaping to provide stable image quality throughout a CMR examination at 7T.

It is a recognized limitation of this study that no SNR and blood/myocardium contrast-to-noise ratio (CNR) values are reported. A previous pilot study on cardiac chamber quantification at 1.5 T and 7.0 T showed that 2D cine FGRE imaging at 7.0 T provided SNR and blood/myocardium CNR that are superior to FGRE acquisitions at 1.5T using the same slice thickness [14]. Careful SNR and CNR validation demonstrated that SNR and CNR derived from 2D cine FGRE at 7T was found to be competitive with that derived from SSFP acquisitions at 1.5 T using standard clinical routine imaging parameter [14].

Regarding image contrast as assessed by visual evaluation, the present results underline that the combination of FGRE with ultrahigh field reaches a grade of contrast that is comparable to SSFP at 1.5T, similar to the results reported for the LV [14]. For the RV, this was true both for transverse and sagittal slice orientation and independent from the voxel size. Opposed to that, the acquisition of homogeneous images is still a challenge in ultrahigh field CMR. Both in sagittal and transverse direction, the results at 7T were inferior compared to 1.5T and a high proportion of 7T images were evident with poor homogeneity for both voxel sizes. Further improvements in subject specific and slice specific B_0- and B_1-shimming are therefore essential to fully exploit the potential of 7T [23,24].

Regarding the quantification of cardiac size and function, it has been shown for 1.5T and 3T that RV volumes are overestimated and mass underestimated when using SSFP instead of FGRE [22,10] - even though the absolute difference is relatively small with a mean RVEDV difference of about 4ml [22]. This difference is explained by the stronger contrast between myocardium and blood on the one side, and between myocardium and epicardial fat on the other side obtained with SSFP. This leads to an outward shift of the endocardial contour and an inward shift of the epicardial contour compared to FGRE. Furthermore, areas with slow flow, as within the apex, are often mistaken for myocardium when using FGRE. It is notable from the present results that the difference in RV quantification between SSFP and FGRE no longer

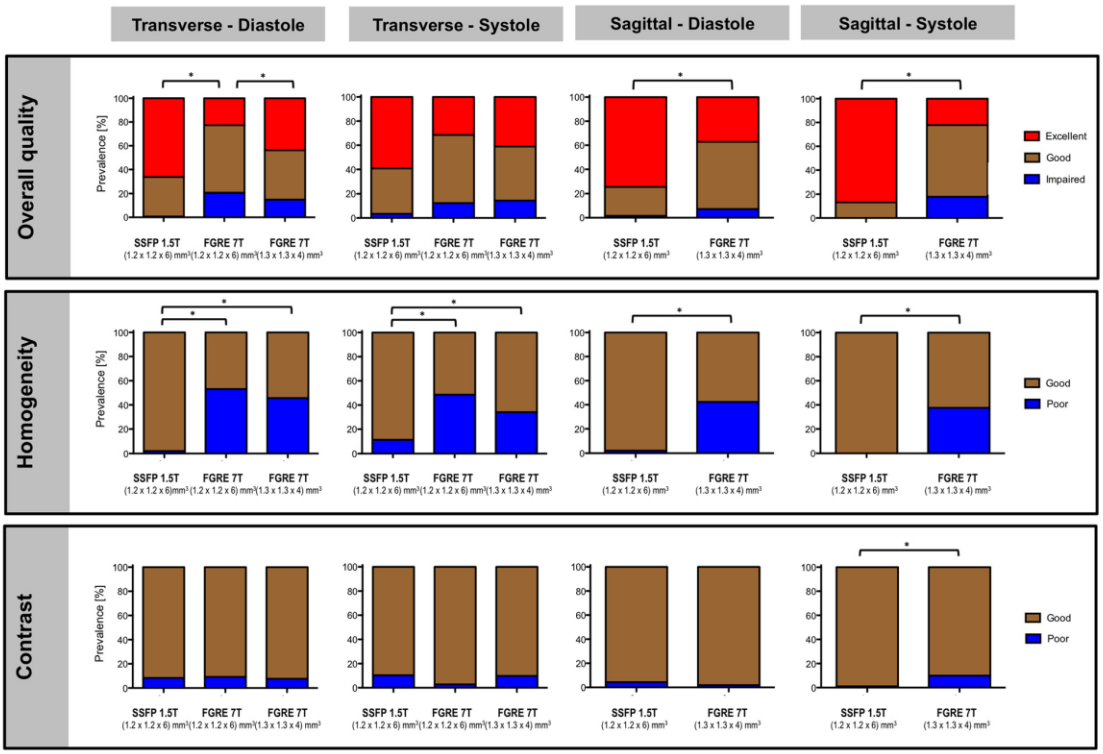

Figure 3 Image quality, contrast and homogeneity. Scoring results are grouped by slice orientation (transverse and sagittal) and by cardiac phase (diastole and systole). Significant inter-group differences are highlighted by "*". The corresponding p-values are given in the text.

Table 1 RV chamber quantification

	1.5T SSFP 1.2x1.2x6mm^3	7T FGRE 1.2x1.2x6mm^3	7T FGRE 1.3x1.3x4mm^3	p-value
RVEDV [ml]				0.5850
Median	146.2	138.6	152.1	
Min. - Max.	127.4 - 202.3	124-0 - 207.7	121.4 - 222.8	
RVESV [ml]				0.5462
Median	65.2	62.4	69.3	
Min. - Max.	57.4 - 91.1	53.7 - 93.5	54.6 - 103.6	
RVEF [%]				0.2789
Median	55.0	56.7	55	
Min. - Max.	54 - 57	54 - 58	54 - 58	
RVM [g]				0.0743
Median	35	36	33	
Min. - Max.	26 - 49	24 - 53	26 - 51	

Legend: RV end-diastolic volume (RVEDV), RV end-systolic volume (RVESV), RV ejection fraction (RVEF) and RV mass (RVM) are presented as median, min and max for each modality (1.5T SSFP, 7T FGRE with two voxel sizes). The p-values refer to the Kruskal-Wallis test including all three modalities. There was no significant difference regarding RVEDV, RVESV, RVEF and RVM.

existed when moving from 1.5T to 7T. This tendency matches the experiences we made for the LV at 7T [14]. The bias between the results obtained for FGRE imaging at 7T with voxel size (1.2x1.2x6)mm^{3}and SSFP at 1.5T (RVEDV 1.2±5.9ml, RVESV 1.7±2.5ml) was within the range of the inter-observer variability reported for SSFP examinations of the RV [22]. Hence, close agreement can be postulated. This finding underlines the accurate endocardial border delineation achievable by FGRE at 7T. Another interesting aspect of the present results was that FGRE at 7T by tendency provided larger volumes than SSFP 1.5T when we decreased the voxel size from (1.2x1.2x6)mm^3 to (1.3x1.3x4)mm^3. We explain this trend mainly by the observation that the higher spatial resolution led to a more detailed differentiation of the RV free wall that caused an outward shift of the manually contoured endocardial borders (Figure 5). This finding on the one hand has to be kept in mind when trying to translate normal values from 1.5T to 7T. On the other hand, it underscores the potential of CMR at 7T

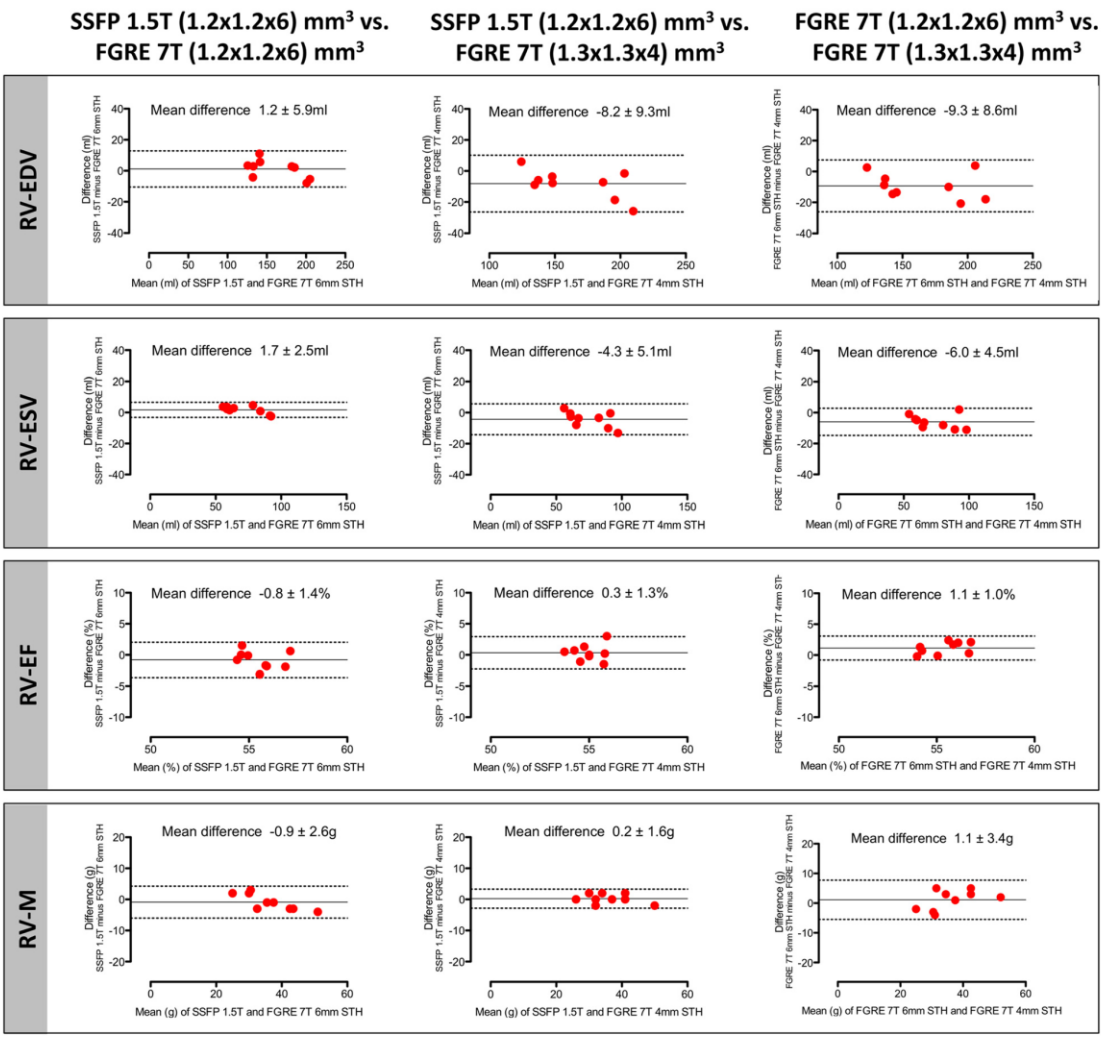

Figure 4 RV chamber quantification. Bland-Altman plots illustrating the agreement between RV volumes, ejection fraction and mass obtained by SSFP at 1.5T as the current gold standard and those derived from FGRE cine acquisitions with different spatial resolutions. [RV-EDV = right ventricular end-diastolic volume; RVESV = right ventricular end-systolic volume; RVEF = right ventricular ejection fraction; RVM = right ventricular mass].

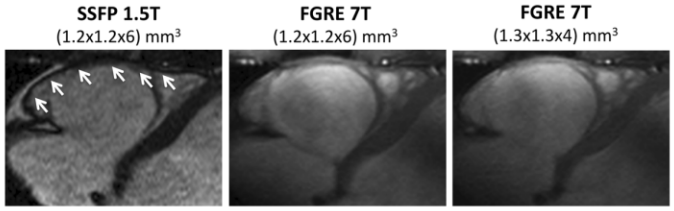

Figure 5 Blood-myocardium contrast of the RV free wall. Focused view on the RV free wall demonstrating that the border between blood and myocardium appears less dark and less sharp at 7T compared to 1.5T, which is further enhanced with decreasing voxel size. This potentially explains the tendency towards larger volume measurements at 7T with voxel size (1.3x1.3x4)mm^3 compared to 1.5T.

to have a more detailed look at the RV free wall. As it can be anticipated from Figure 3, some inter-subject variability of trabecular structure and compact layer thickness may exist. For instance, the measurement of the compact layer of the free RV wall as well of the remaining trabecular layer may provide new insights into the microstructure of the RV myocardium. Furthermore, the accurate quantification of RV mass based on properly spatially resolved cine images would strengthen its role as a cardiovascular risk marker. After this first evidence of the feasibility of RV cine imaging at 7T, such interesting aspects need further investigation in future studies with sample sizes large enough to provide adequate power.

Conclusions

In conclusion, the present study demonstrated that cine imaging of the RV is feasible at 7T using FGRE techniques. The achieved image quality was comparable to SSFP at 1.5T and allowed accurate myocardial border delineation for RV chamber quantification, which provided RV volumes, mass and function with close agreement to SSFP at 1.5T. This work is regarded as fundament and stimulator for further efforts to explore whether enhanced spatial resolution together with ultrahigh field strength can provide more detailed insights into the structure of the RV.

Additional files

Additional file 1: Long axis view of the right ventricle obtained by FGRE cine imaging at 7T with voxel size (1.3x1.3x4)mm^3 underlining the excellent blood/myocardium contrast even in the right ventricular apex.

Additional file 2: Transverse view of the right ventricle obtained by FGRE cine 7T with voxel size (1.3x1.3x4)mm^3 underlining the excellent resolution of the RV trabeculae.

Additional file 3: Cinematic four-chamber views of all subjects obtained with 2D cine FGRE at 7T using a voxel size of (1.3x1.3x4) mm^3.

Competing interests

The authors declare that they have no competing interests with the exception of Thoralf Niendorf and Jan Rieger, who are founder of MRI.TOOLS GmbH (Berlin, Germany).

Authors' contributions

FvKB and VT contributed to the study design, image acquisition, image interpretation, data storage, statistical data analysis and data interpretation and drafted the first version of the manuscript; LW and CT contributed to the image acquisition (in particular regarding coils) and data interpretation; JR contributed to the image acquisition (in particular regarding cardiac gating) and data interpretation; MD contributed to the image acquisition, image interpretation and data interpretation; TN and JSM contributed to the study design, image acquisition, image interpretation, data storage, statistical data analysis and data interpretation. All authors helped to draft the manuscript, and read and approved the final manuscript.

Acknowledgements

We thank the study nurses Antje Els and Elke Nickel-Szczech for coordinating and documenting the examinations, and Denise Kleindienst for assisting during CMR image acquisition. We thank Dr. Carsten Schwenke (scossis, Berlin, Germany) for supporting the statistical calculations.
FvKB and MD are supported by a research grant of the Else-Kröner Fresenius Stiftung (Bad Homburg, Germany). The study was supported by institutional grants of the Charité Medical Faculty Berlin and the Max-Delbrueck-Center for Molecular Medicine.

Author details

[1]Berlin Ultrahigh Field Facility (B.U.F.F.), Max-Delbrueck Center for Molecular Medicine, Berlin, Germany. [2]Working Group on Cardiovascular Magnetic Resonance, Experimental and Clinical Research Center, a joint cooperation between the Charité Medical Faculty and the Max-Delbrueck Center for Molecular Medicine, HELIOS Klinikum Berlin Buch, Department of Cardiology and Nephrology, Berlin, Germany. [3]Experimental and Clinical Research Center, a joint cooperation between the Charité Medical Faculty and the Max-Delbrueck Center for Molecular Medicine, Berlin, Germany.

Received: 17 October 2012 Accepted: 6 March 2013
Published: 14 March 2013

References

1. Hopkins WE. **Right ventricular performance in congenital heart disease: a physiologic and pathophysiologic perspective.** *Cardiol Clin.* 2012; **30**:205–18.
2. Galie N, Hoeper MM, Humbert M, Torbicki A, Vachiery JL, Barbera JA, Beghetti M, Corris P, Gaine S, Gibbs JS, Gomez-Sanchez MA, Jondeau G, Klepetko W, Opitz C, Peacock A, Rubin L, Zellweger M, Simonneau G. **Guidelines for the diagnosis and treatment of pulmonary hypertension: the Task Force for the Diagnosis and Treatment of Pulmonary Hypertension of the European Society of Cardiology (ESC) and the European Respiratory Society (ERS), endorsed by the International Society of Heart and Lung Transplantation (ISHLT).** *Eur Heart J.* 2009; **30**:2493–537.
3. Kumar A, Abdel-Aty H, Kriedemann I, Schulz-Menger J, Gross CM, Dietz R, Friedrich MG. **Contrast-enhanced cardiovascular magnetic resonance imaging of right ventricular infarction.** *J Am Coll Cardiol.* 2006; **48**:1969–76.
4. Marcus FI, McKenna WJ, Sherrill D, Basso C, Bauce B, Bluemke DA, Calkins H, Corrado D, Cox MG, Daubert JP, Fontaine G, Gear K, Hauer R, Nava A, Picard MH, Protonotarios N, Saffitz JE, Sanborn DM, Steinberg JS, Tandri H, Thiene G, Towbin JA, Tsatsopoulou A, Wichter T, Zareba W. **Diagnosis of arrhythmogenic right ventricular cardiomyopathy/dysplasia: proposed modification of the task force criteria.** *Circulation.* 2010; **121**:1533–41.
5. Kilner PJ, Geva T, Kaemmerer H, Trindade PT, Schwitter J, Webb GD. **Recommendations for cardiovascular magnetic resonance in adults with congenital heart disease from the respective working groups of the European Society of Cardiology.** *Eur Heart J.* 2010; **31**:794–805.
6. Alfakih K, Plein S, Bloomer T, Jones T, Ridgway J, Sivananthan M. **Comparison of right ventricular volume measurements between axial and short axis orientation using steady-state free precession magnetic resonance imaging.** *J Magn Rson Imaging.* 2003; **18**:25–32.
7. von Knobelsdorff-Brenkenhoff F, Bublak A, El-Mahmoud S, Wassmuth R, Opitz C, Schulz-Menger J. **Single-centre survey of the application of cardiovascular magnetic resonance in clinical routine.** *Eur Heart J Cardiovasc Imaging.* 2013; **14**:62–8.
8. Kawut SM, Barr RG, Lima JA, Praestgaard A, Johnson WC, Chahal H, Ogunyankin KO, Bristow MR, Kizer JR, Tandri H, Bluemke DA. **Right Ventricular Structure Is Associated With the Risk of Heart Failure and Cardiovascular Death: The Multi-Ethnic Study of Atherosclerosis (MESA)-Right Ventricle Study.** *Circulation.* 2012; **126**:1681–88.
9. Haddad F, Hunt SA, Rosenthal DN, Murphy DJ. **Right ventricular function in cardiovascular disease, part I: Anatomy, physiology, aging, and functional assessment of the right ventricle.** *Circulation.* 2008; **117**:1436–48.
10. Alfakih K, Plein S, Thiele H, Jones T, Ridgway JP, Sivananthan MU. **Normal human left and right ventricular dimensions for MRI as assessed by turbo gradient echo and steady-state free precession imaging sequences.** *J Magn Reson Imaging.* 2003; **17**:323–29.
11. Niendorf T, Sodickson DK, Krombach GA, Schulz-Menger J. **Toward cardiovascular MRI at 7 T: clinical needs, technical solutions and research promises.** *Eur Radiol.* 2010; **20**:2806–16.

12. Niendorf T, Graessl A, Thalhammer C, Dieringer MA, Kraus O, Santoro D, Fuchs K, Hezel F, Waiczies S, Ittermann B, Winter L. **Progress and promises of human cardiac magnetic resonance at ultrahigh fields: A physics perspective.** *J Magn Reson.* 2012. epub ahead of print.
13. Snyder CJ, DelaBarre L, Metzger GJ, van de Moortele PF, Akgun C, Ugurbil K, Vaughan JT. **Initial results of cardiac imaging at 7 Tesla.** *Magn Reson Med.* 2009; **61:**517–24.
14. von Knobelsdorff-Brenkenhoff F, Frauenrath T, Prothmann M, Dieringer MA, Hezel F, Renz W, Kretschel K, Niendorf T, Schulz-Menger J. **Cardiac chamber quantification using magnetic resonance imaging at 7 Tesla–a pilot study.** *Eur Radiol.* 2010; **20:**2844–52.
15. Brandts A, Westenberg JJ, Versluis MJ, Kroft LJ, Smith NB, Webb AG, de Roos A. **Quantitative assessment of left ventricular function in humans at 7 T.** *Magn Reson Med.* 2010; **64:**1471–77.
16. Suttie JJ, Delabarre L, Pitcher A, van de Moortele PF, Dass S, Snyder CJ, Francis JM, Metzger GJ, Weale P, Ugurbil K, Neubauer S, Robson M, Vaughan T. **7 Tesla (T) human cardiovascular magnetic resonance imaging using FLASH and SSFP to assess cardiac function: validation against 1.5 T and 3 T.** *NMR Biomed.* 2012; **25:**27–34.
17. Dieringer MA, Renz W, Lindel T, Seifert F, Frauenrath T, von Knobelsdorff-Brenkenhoff F, Waiczies H, Hoffmann W, Rieger J, Pfeiffer H, Ittermann B, Schulz-Menger J, Niendorf T. **Design and application of a four-channel transmit/receive surface coil for functional cardiac imaging at 7T.** *J Magn Reson Imaging.* 2011; **33:**736–41.
18. Grassl A, Winter L, Thalhammer C, Renz W, Kellman P, Martin C, von Knobelsdorff-Brenkenhoff F, Tkachenko V, Schulz-Menger J, Niendorf T. **Design, evaluation and application of an eight channel transmit/receive coil array for cardiac MRI at 7.0T.** *Eur J Radiol.* 2011. epub ahead of print.
19. Winter L, Kellman P, Renz W, Grassl A, Hezel F, Thalhammer C, von Knobelsdorff-Brenkenhoff F, Tkachenko V, Schulz-Menger J, Niendorf T. **Comparison of three multichannel transmit/receive radiofrequency coil configurations for anatomic and functional cardiac MRI at 7.0T: implications for clinical imaging.** *Eur Radiol.* 2012; **22:**2211–20.
20. Thalhammer C, Renz W, Winter L, Hezel F, Rieger J, Pfeiffer H, Graessl A, Seifert F, Hoffmann W, von Knobelsdorff-Brenkenhoff F, Tkachenko V, Schulz-Menger J, Kellman P, Niendorf T. **Two-Dimensional sixteen channel transmit/receive coil array for cardiac MRI at 7.0 T: Design, evaluation, and application.** *J Magn Reson Imaging.* 2012; **36:**847–57.
21. Frauenrath T, Hezel F, Renz W, D'Orth Tde G, Dieringer M, Von Knobelsdorff-Brenkenhoff F, Prothmann M, Menger JS, Niendorf T. **Acoustic cardiac triggering: a practical solution for synchronization and gating of cardiovascular magnetic resonance at 7 Tesla.** *J Cardiovasc Magn Reson.* 2010; **12:**67.
22. Grothues F, Boenigk H, Graessner J, Kanowski M, Klein HU. **Balanced steady-state free precession vs. segmented fast low-angle shot for the evaluation of ventricular volumes, mass, and function at 3 Tesla.** *J Magn Reson Imaging.* 2007; **26:**392–400.
23. Sengupta S, Welch EB, Zhao Y, Foxall D, Starewicz P, Anderson AW, Gore JC, Avison MJ. **Dynamic B0 shimming at 7 T.** *Magn Reson Imaging.* 2011; **29:**483–96.
24. Schar M, Vonken EJ, Stuber M. **Simultaneous B (0)- and B(1)+–map acquisition for fast localized shim, frequency, and RF power determination in the heart at 3 T.** *Magn Reson Med.* 2010; **63:**419–26.

doi:10.1186/1532-429X-15-23
Cite this article as: von Knobelsdorff-Brenkenhoff *et al.*: Assessment of the right ventricle with cardiovascular magnetic resonance at 7 Tesla. *Journal of Cardiovascular Magnetic Resonance* 2013 **15**:23.

Detailing Magnetic Field Strength Dependence and Segmental Artifact Distribution of Myocardial Effective Transverse Relaxation Rate at 1.5, 3.0, and 7.0 T

Meloni A, Hezel F, Positano V, Keilberg P, Pepe A, Lombardi M, Niendorf T.
Magn Reson Med. 2014 Jun;71(6):2224-30.

http://dx.doi.org/10.1002/mrm.24856

Modular 32-channel transceiver coil array for cardiac MRI at 7.0T

Graessl A, Renz W, **Hezel F**, Dieringer MA, Winter L, Oezerdem C, Rieger J, Kellman P, Santoro D, Lindel TD, Frauenrath T, Pfeiffer H, Niendorf T.
Magn Reson Med. 2013 Jul 31, [Epub ahead of print]

http://dx.doi.org/10.1002/mrm.24903

Lebenslauf

Mein Lebenslauf wird aus datenschutzrechtlichen Gründen in der elektronischen Version meiner Arbeit nicht veröffentlicht.

Mein Lebenslauf wird aus datenschutzrechtlichen Gründen in der elektronischen Version meiner Arbeit nicht veröffentlicht.

Mein Lebenslauf wird aus datenschutzrechtlichen Gründen in der elektronischen Version meiner Arbeit nicht veröffentlicht.

Publikationsliste

Publikationen in Fachzeitschriften

1. **Modular 32-channel transceiver coil array for cardiac MRI at 7.0T**

   Graessl A, Renz W, **Hezel F**, Dieringer MA, Winter L, Oezerdem C, Rieger J, Kellman P, Santoro D, Lindel TD, Frauenrath T, Pfeiffer H, Niendorf T.
   Magn Reson Med. 2013 Jul 31, [Epub ahead of print]

   Impact Factor: 2,96

2. **Detailing Magnetic Field Strength Dependence and Segmental Artifact Distribution of Myocardial Effective Transverse Relaxation Rate at 1.5, 3.0, and 7.0 T**

   Meloni A, **Hezel F**, Positano V, Keilberg P, Pepe A, Lombardi M, Niendorf T.
   Magn Reson Med. 2014 Jun;71(6):2224-30

   Impact Factor: 2,96

3. **Assessment of the right ventricle with cardiovascular magnetic resonance at 7 Tesla**

   von Knobelsdorff-Brenkenhoff F, Tkachenko V, Winter L, Rieger J, Thalhammer C,Hezel F, Graessl A, Dieringer MA, Niendorf T, Schulz-Menger J.
   J Cardiovasc Magn Reson. 2013, 15:23

   Impact Factor: 3,72

4. **Isometric handgrip exercise during cardiovascular magnetic resonance imaging: Set-up and cardiovascular effects**

   von Knobelsdorff-Brenkenhoff F, Dieringer MA, Fuchs K, **Hezel F**, Niendorf T, Schulz-Menger J.
   J Magn Reson Imaging 2013 Jun;37(6):1342-50

   Impact Factor: 2,7

5. **Progress and promises of human cardiac magnetic resonance at ultrahigh fields: A physics perspective**

   Niendorf T, Graessl A, Thalhammer C, Dieringer MA, Kraus O, Santoro D, Fuchs K, **Hezel F**, Waiczies S, Ittermann B, Winter L.
   J Magn Reson. 2013 Apr;229:208-22

   Impact Factor: 2,14

6. **High spatial resolution and temporally resolved T_2^* mapping of normal human myocardium at 7.0 Tesla: an ultrahigh field magnetic resonance feasibility study**

   Hezel F, Thalhammer C, Waiczies S, Schulz-Menger J, Niendorf T.

   PLoS One.2012;7(12):e52324

   Impact Factor: 4,09

7. **Two-dimensional sixteen channel transmit/receive coil array for cardiac MRI at 7.0 T: design, evaluation, and application.**

   Thalhammer C, Renz W, Winter L, **Hezel F**, Rieger J, Pfeiffer H, Graessl A, Seifert F, Hoffmann W, von Knobelsdorff-Brenkenhoff F, Tkachenko V, Schulz-Menger J, Kellman P, Niendorf T.

   J Magn Reson Imaging. 2012 Oct;36(4):847-57

   Impact Factor: 2,7

8. **Comparison of three multichannel transmit/receive radiofrequency coil configurations for anatomic and functional cardiac MRI at 7.0T: implications for clinical imaging**

   Winter L, Kellman P, Renz W, Gräßl A, **Hezel F**, Thalhammer C, von Knobelsdorff-Brenkenhoff F, Tkachenko V, Schulz-Menger J, Niendorf T.

   Eur Radiol. 2012 Oct;22(10):2211-20

   Impact Factor: 3,22

9. **Acoustic cardiac triggering: a practical solution for synchronization and gating of cardiovascular magnetic resonance at 7 Tesla**

   Frauenrath T, **Hezel F**, Renz W, d'Orth Tde G, Dieringer M, von Knobelsdorff-Brenkenhoff F, Prothmann M, Schulz Menger J, Niendorf T.

   J Cardiovasc Magn Reson. 2010 Nov 16;12:67

   Impact Factor: 3,72

10. **Cardiac chamber quantification using magnetic resonance imaging at 7 Tesla--a pilot study**

    von Knobelsdorff-Brenkenhoff F, Frauenrath T, Prothmann M, Dieringer MA, **Hezel F**, Renz W, Kretschel K, Niendorf T, Schulz-Menger J.

    Eur Radiol. 2010 Dec;20(12):2844-52

    Impact Factor: 3,22

11. **Comparison of left ventricular function assessment using phonocardiogram- and electrocardiogram-triggered 2D SSFP CINE MR imaging at 1.5 T and 3.0 T**

    Becker M, Frauenrath T, **Hezel F**, Krombach GA, Kremer U, Koppers B, Butenweg C, Goemmel A, Utting JF, Schulz-Menger J, Niendorf T.

    Eur Radiol. 2010 Jun;20(6):1344-55

    Impact Factor: 3,22

12. **Feasibility of cardiac gating free of interference with electro-magnetic fields at 1.5 Tesla, 3.0 Tesla and 7.0 Tesla using an MR-stethoscope**

    Frauenrath T, **Hezel F**, Heinrichs U, Kozerke S, Utting JF, Kob M, Butenweg C, Boesiger P, Niendorf T.

    Invest Radiol. 2009 Sep;44(9):539-47

    Impact Factor: 4,59

13. **Myocardial T2* mapping free of distortion using susceptibility-weighted fast spin-echo imaging: a feasibility study at 1.5 T and 3.0 T**

    Heinrichs U, Utting JF, Frauenrath T, **Hezel F**, Krombach GA, Hodenius MA, Kozerke S, Niendorf T.

    Magn Reson Med. 2009 Sep;62(3):822-8

    Impact Factor: 2,96

Patentanmeldungen:

- **Method for Automatic Motion Analysis and Quality Assurance in Cardiovascular Magnetic Resonance Imaging**

  Fabian Hezel, Thoralf Niendorf

  DE102009011382 A1 / WO2010099973 A1 / US20120045104

- **MRI operation procedure – accelerated distortion free susceptibility weighted imaging**

  Fabian Hezel, Thoralf Niendorf

  EP2317333 A1 / US 20110105890

Internationale Konferenzbeiträge:

ISMRM 2013 Salt Lake City, USA:

- Towards Myocardial T_2^* Mapping at 7.0 T: Assessment and Implications of Static Magnetic Fields Variations
  Hezel F, Kellman P, Winter L, Kraus O, Fuchs K, Niendorf T
- Coronary MR Angiography at 7.0 Tesla Using 3D Fat-Water Separated Imaging and a 8 Channel Array of Bowtie Dipole Transceivers: A Feasibility Study
  Hezel F, Kellman P, Winter L, Kraus O, Fuchs K, Niendorf T
- A two-dimensional 16 Channel Dipole Transceiver Array for Cardiac MR at 7.0 T: Design, Evaluation of RF Shimming Behavior and Application in CINE Imaging
  Graessl A, Winter L, Oezerdem C, Hezel F, Fuchs K, Pfeiffer H, Hoffmann W, Niendorf T
- Feasibility of Cardiac Fast Spin Echo Imaging at 7.0 T Using a Two-Dimensional 16 Channel Array of Bowtie Transceivers
  Fuchs K, Hezel F, Winter L, Oezerdem C, Graessl A, Dieringer MA, Kraus O, Niendorf T
- 2D CINE SSFP Imaging At 7.0T Using 8-Channel Bowtie Antenna Transceiver Arrays: A Cardiac MR Feasibility Study
  Kraus O, Dieringer MA, Hezel F, Winter L, Graessl A, Oezerdem C, Niendorf T
- 2-in-1: Simultaneously T_2/T_2^* Weighted Double Echo Fast Spin Echo Imaging
  Fuchs K, Hezel F, Klix S, Niendorf T
- Assessment of multiple sclerosis at 7.0 T using high spatial resolution, fluid attenuated inversion recovery prepared susceptibility weighted fast spin echo imaging
  Tovar Martinez E, Fuchs K, Hezel F, Dieringer MA, Wuerfel J, Niendorf T

ISMRM 2012 Melbourne, Australien:

- Feasibility of Abdominal MRI at 7.0 T Using a Novel 32 Channel Transceiver Coil Array
  Hezel F, Graessl A, Kellman P, Niendorf T
- Toward Assessment of Iron Overload Diseases at 7.0 T: Myocardial T_2^* Mapping to Derive Global and Segmental T_2^* Norm Values for Healthy Subjects at 7.0 T
  Hezel F, Meloni A, Schulz-Menger J, Keilberg P, Kellman P, Lombardi M, Niendorf T
- Accelerated Black Blood Imaging Using Self-Calibrated Split-Echo FSE (SCSE-FSE) Imaging
  Klix S, Hezel F, Ruff J, Niendorf T
- Cardiac Triggered B_1^+ Mapping Using Bloch Siegert in the Heart at 3T
  Santoro D, Samson-Himmelstjerna F, Carinci F, Hezel F, Dieringer MA, Niendorf T
- Design, Evaluation and Application of a Modular 32 Channel Transmit/Receive Surface Coil Array for Cardiac MRI at 7T
  Graessl A, Renz W, Hezel F, Frauenrath T, Pfeiffer H, Hoffmann W, Kellman P, Martin C, Niendorf T
- High Spatial Resolution Susceptibility Weighted Fast Spin Echo Brain Imaging at 3.0T and 7.0T
  Tovar Martinez E, Hezel F, Fuchs K, Wuerfel J, Paul F, Sobesky J, Niendorf T

- Improved Cardiac Triggering by Combining Multiple Physiological Signals: A Cardiac MR Feasibility Study at 7.0 T
  Frauenrath T, Fuchs K, Hezel F, Dieringer MA, Rieger J, Niendorf T
- Lessons Learned from Cardiac MRI at 7.0 T: LV Function Assessment at 3.0 T Using Local Multi-Channel Transceiver Coil Arrays
  Frauenrath T, Pfeiffer H, Hezel F, Dieringer MA, Winter L; Graessl A, Santoro D, Oezerdem C, Renz W, Greiser A, Niendorf T
- Magnetic Field Dependence of Myocardial R_2^* Values and Segmental Myocardial Field Inhomogeneity Assessed at 1.5 T, 3.0 T and 7.0 T.
  Meloni A, Hezel F, Positano V, Keilberg P, Pepe A, Niendorf T, Lombardi M

ISMRM 2011, Montreal, Kanada

- Rapid CINE Myocardial T_2^* Mapping at 7T
  Hezel F, Kellman P, Thalhammer C, Renz W, Niendorf T
- Initial Results of Abdominal MRI at 7T Using a 16 channel Transmit/Receive Coil
  Hezel F, Kellman P, Thalhammer C, Oezerdem C, Renz W, Niendorf T
- Fat-water separated imaging at 7T: initial results for cardiac applications
  Kellman P, Hezel F, Shah S, Renz W, Thalhammer C, Schulz-Menger J, Niendorf T
- Anatomic and Functional Cardiac MR at 7T: A comparison of 4, 8 and 16 Element Transceive RF Coil Designs
  Winter L, Thalhammer C, Dieringer MA, Oezerdem C, Rieger J, Hezel F, Renz W, Niendorf T
- Design, Evaluation and Application of a Sixteen Channel Transmit/Receive Surface Coil Array for Cardiac MRI at 7T
  Thalhammer T, Renz W, Pfeiffer H, Rieger J, Winter L, Hezel F, Seifert F, Hoffmann W, Seemann R, Niendorf T

ISMRN 2010, Stockholm, Schweden

- Highly Accelerated Single Breath-Hold Myocardial T_2^* Mapping Using Susceptibility Weighted Fast Spin-Echo Imaging
  Hezel F, Krombach G, Kozerke S, Niendorf T
- Feasibility of CINE Myocardial T_2^* Mapping Using Susceptibility Weighted Gradient-Echo Imaging at 7.0 T
  Hezel F, Frauenrath T, Renz W, Schulz-Menger J, Niendorf T
- Accurate Left Ventricular Chamber Quantification Is Feasible Using Cardiovascular Magnetic Resonance at 7T
  Von Knobelsdorff-Brenkenhoff F, Frauenrath T, Prothmann M, Dieringer MA, Hezel F, Renz W, Kretschel K, Niendorf T, Schulz-Menger J
- Banding Artifact Reduction in 2D CINE Balanced SSFP at 3.0 T Using Phase-Cycling and k-T BLAST
  Kremer U, Hezel F, Krombach G, Niendorf T
- Cardiac Imaging at 7.0T: Comparison of Pulse Oximetry, Electrocardiogram and Phonocardiogram Triggered 2D CINE for Left Ventricular Function Assessment
  Frauenrath T, Hezel F, Renz W, Von Knobelsdorff-Brenkenhoff F, De Geyer D'Orth T, Prothmann M, Dieringer MA, Kretschel K, Schulz-Menger J, Niendorf T

- Comparison of Left Function Assessment Using Phonocardiogram and Electrocardiogram Triggered 2D SSFP CINE MR Imaging at 1.5 T and 3.0 T
  Frauenrath T, Becker M, Hezel F, Krombach G, Kremer U, Schulz-Menger J, Niendorf T
- Single Breath-Hold High Spatial Resolution Abdominal Imaging and T_2^* Mapping at 7.0 T
  Dieringer M, Hezel F, Renz W, Boyé P, Ittermann B, Seifert F, Lindel T, Niendorf T

ISMRM 2009, Honolulu , USA

- Analysis of Endocardial Border Sharpness of Accelerated 2D CINE SSFP: Implications for Left Ventricular Function Assessment
  Hezel F, Katoh M, Kühl H, Grawe H, Utting JF, Niendorf T
- Feasibility of Acoustically Triggered CINE Imaging for Global Cardiac Function Assessment Using an MR-Stethoscope
  Frauenrath T, Hezel F, Utting JF, Krombach G, Niendorf T
- Myocardial T_2^* Mapping Free of Distortion Using Susceptibility Weighted Spin-Echo Based Imaging: A Feasibility Study at 1.5 T and 3.0T
  Heinrichs U, Utting JF, Frauenrath T, Hezel F, Krombach G, Hodenius M, Kozerke S,Niendorf T

Danksagung

Ich möchte meinen Betreuer Herr Prof. Dr. Thoralf Niendorf für seine hervorragende und inspirierende Unterstützung und Motivation bei dieser Dissertation danken.

Desweitern danke ich dem gesamten Team der Berlin Ultrahigh Field Facility für ihre technische, organisatorische inhaltliche und auch oft moralische Unterstützung. Ein besonderer herzlicher Dank gebührt dabei Katharina, Julia, Lukas, Till, Christof, Davide, Celal und Andeas für deren Hilfe bei Pulsprogrammierung, bei der Spin-Gymnastik und die Entwicklung hervorragender RF-Spulen.

Ich danke Peter Kellman vom NIH für seine hilfreichen Hinweise und die fruchtbaren Diskussionen über unsere Entwicklungen und Forschungsergbnisse. Ebenfalls danke ich Frau Prof. Dr. Jeanette Schulz-Menger und Dr. Florian von Knobelsdorff-Brenkenhoff aus der Arbeitsgruppe Kardiale MRT am Charité Campus Buch, welche mir für jegliche medizinische Fragestellungen stets geduldig zur Verfügung standen.